Wireless communication in vehicles

Steven John Herbert

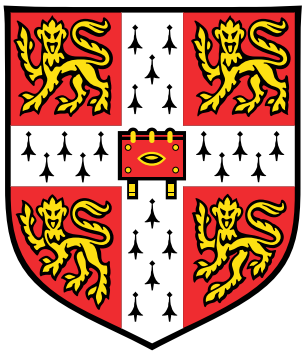

University of Cambridge
Computer Laboratory
Darwin College

December 2014

This dissertation is approved for
the degree of *Doctor of Philosophy*

Acknowledgements

Clichéd though it is to say so, this dissertation would not have been possible without many people. A special mention goes to the following:

To my supervisors: to Dr. Ian Wassell, for his gentle guidance, remarkable breadth of knowledge and unfailing willingness to discuss football; and to Dr. Tian-Hong Loh, for his help with my measurements whilst based at the National Physical Laboratory (NPL), and for our numerous all afternoon-long meetings pouring over the minutiae of my work.

To my other colleagues: to Ruoshui with whom I conducted my first ever measurement campaign; to Bogdan for his continued interest in my work, and for challenging me always to think more deeply about the matters in hand; to Rob and Alastair for conducting my internal progress reviews and showing me the importance of focussing on the ultimate goals of my work; and to David Humphreys, David Knight and Jonathan Rigelsford for helping me with my measurements and subsequent analysis. To my PhD examiners and those who kindly reviewed my dissertation as well as those who have previously reviewed my papers; and to the Engineering and Physical Sciences Research Council, who, along with NPL provided a CASE award which funded this research.

To all my friends: to my friends at Darwin College, in parallel with whom I have walked the PhD journey; to my friends at the Computer Laboratory, especially Niall, Alan and our *lunch club*, for all those engaging discussions and table-football matches; to my friends at NPL, with whom I shared that glorious summer of 2012 and to Clare for being a good friend in the harder months which followed. To my former housemate, Andrew and his (now) wife, Ruth, for always being there; to my friend and confidant, Shuchen, whose life strangely seems to mirror my own, thus enabling us a special insight into each other's lives; and to my beloved friend Janet, who has shared each up and down of this PhD with me, and cares passionately about my success.

To my family: to my grandparents, sadly not all of whom are around to witness me complete my PhD, but without whose encouragement of my creativity and tenacity in my formative years, I would never have been able to do so; to Elizabeth, Peter and Caroline, all inspirational scholars in their own right, and to me, not just siblings, but trusted friends; and finally to my parents, for their eternal love and unswerving support.

Declaration

This dissertation is the result of my own work and includes nothing which is the outcome of work done in collaboration, except where specifically indicated in the text.

This dissertation does not exceed the regulation length of 60000 words.

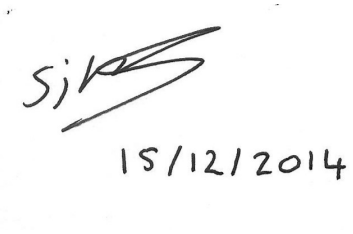

Steven Herbert
Cambridge
December 2014

Abstract

There is an increasing interest in the deployment of wireless communication systems in vehicles. The motivation for this work is to provide a fundamental characterisation of the in-vehicle Electromagnetic (EM) wave propagation environment, and to demonstrate how this can be used to aid the deployment of wireless communication systems in vehicles.

The fundamental characterisation of the in-vehicle EM wave propagation environment presented in this dissertation yields a number of useful outcomes. The instantaneous impulse response of the in-vehicle channel is characterised, which is presented in the form of a statistical model for arriving rays. Noticing that it is impractical to undertake a full statistical characterisation of the time-varying impulse response, the time variation of the in-vehicle channel is instead characterised as a Doppler spread. This approach provides parameters which are sufficient to perform an information theoretic analysis to lower bound the capacity of the in-vehicle channel. For typical operating conditions, it is found that the channel capacity is approximately equal to that of the same channel with perfect channel state information available at the receiver.

Having established the fundamental EM wave propagation characteristics for a single in-vehicle wireless channel, the EM properties of the cavity itself are characterised. This is achieved through a thorough investigation into the analogy between vehicle cavities and reverberation chambers, specifically considering the quality factor (and hence time constant), EM isolation, and electric field uniformity of typical vehicle cavities. This approach yields the important insight that the root mean square delay spread is approximately the same for all wireless links in a typical vehicle cavity. Also, that the angular spread of energy received at any given location (away from the cavity boundaries) is approximately uniform, and that over short distances the coherence distance is well defined, and hence Multiple Input Multiple Output antenna arrays should work well in vehicles.

To what extent a typical wireless system can exploit this characterisation depends on how well the parameters can be estimated by a typical wireless communication system. This is also addressed, specifically investigating the estimation of the cavity time constant, and channel time variation. It is found that both of these can be estimated well using a typical wireless sensor network system.

Publications

S. Herbert, T.-H. Loh, I. Wassell and J. Rigelsford, "On the analogy between vehicle and vehicle-like cavities with reverberation chambers," in *IEEE Transactions on Antennas and Propagations*, 2014.

S. Herbert, I. Wassell, T.-H. Loh and J. Rigelsford, "Characterising the spectral properties and time variation of the in-vehicle wireless communication channel," in *IEEE Transactions on Communications*, 2014.

S. Herbert, T.-H. Loh and I. Wassell, "An impulse response model and Q-factor estimation for vehicle cavities," in *IEEE Transactions on Vehicular Technology*, 2013.

R. Liu, **S. Herbert**, T.-H. Loh and I. Wassell, "A study on frequency diversity for intra-vehicular wireless sensor networks (WSNs)," in *IEEE Vehicular Technology Conference (VTC Fall)*, 2011.

Contents

List of Figures

List of Tables

Glossary

Roman symbols

A	Area
c	The speed of light in a vacuum (3.00×10^8 m/s)
C	Capacity
$\mathcal{CN}$	Complex Gaussian distribution
d	Distance
E	Electric field
E	Energy
$\mathbb{E}$	Expectation
f	Frequency
$h_{\mathbb{H}}$	Channel time varying impulse response
$\mathbb{H}$	Linear integral operator describing the action of a wireless channel
$\mathcal{H}$	Entropy
$\mathcal{I}$	Mutual information
j	Square root of minus one
$\mathcal{N}$	Gaussian distribution
P	Probability
P	Power
P_H	Power spectral density
$\mathrm{P}_{\mathbb{H}}$	Power delay profile
Q	Quality factor
R	Autocorrelation function
R	Achievable rate
$\mathcal{R}$	Rayleigh distribution
S	Matrix of Scattering parameters
t	Absolute time
$T_{\mathbb{H}}$	Channel time varying frequency response

v	Signal
V	Volume
w	Wall loss per unit area
W	Bandwidth
z	Channel response

Greek symbols

Γ	Covariance matrix (complex)
δ	*Dirac* delta function
ζ	Time shift
η	Antenna efficiency
λ	Wavelength
μ	Mean
ν	Frequency shift
σ	Standard deviation
σ^2	Variance
Σ	Covariance matrix (real)
τ	Time elapsed since impulse
τ_c	Cavity time constant
τ_{rms}	Root mean square delay spread
ω	Angular frequency

Acronyms

ACC	Autocorrelation Co-efficient
ACF	Autocorrelation Function
AWGN	Additive White Gaussian Noise
CLT	Central Limit Theorem
CSI	Channel State Information
EF	Electric Field
EM	Electromagnetic
EUT	Environment Under Test
IDFT	Inverse Discrete Fourier Transform
IID	Independent Identically Distributed
ISM	Industrial Scientific and Medical
LOS	Line-of-Sight

LUF	Lowest Usable Frequency
MIMO	Multiple Input Multiple Output
MMSE	Minimum Mean Squared Error
NPL	National Physical Laboratory
OFDM	Orthogonal Frequency Division Multiplexing
PDF	Probability Density Function
PDP	Power Delay Profile
PDS	Positive Definite Symmetric
PER	Packet Error Rate
PMF	Probability Mass Function
PSD	Power Spectral Density
QF	Quality Factor
RAM	Radiation Absorbent Material
RHS	Right Hand Side
RMS	Root Mean Square
RSSI	Received Signal Strength Indicator
SP	Scattering Parameter
SPM	Scattering Parameter Matrix
SA	Spectrum Analyser
SB9112	Schwarzbeck 9112 Biconical Antenna
SB9113	Schwarzbeck 9113 Biconical Antenna
SG	Signal Generator
SNR	Signal to Noise Ratio
US	Uncorrelated Scattering
VNA	Vector Network Analyser
WSN	Wireless Sensor Network
WSS	Wide Sense Stationary
WSSUS	Wide-Sense Stationary Uncorrelated Scattering
ZMCS	Zero Mean Circularly Symmetric

Chapter 1

Introduction

This dissertation details the Electromagnetic (EM) wave propagation modelling and information capacity evaluation of a wireless communication channel existing within an EM cavity. Details of how this analysis can improve the effectiveness of in-vehicle wireless communication systems are also given.

For the purposes of this dissertation an EM cavity is defined as:

A region of arbitrary, and not necessarily uniform medium, partially or fully enclosed by one or more highly reflective surfaces.

This definition is deliberately general, to maximise the applicability, and hence impact, of the research. The reason that the dissertation is titled *wireless communication in vehicles*, rather than *wireless communication in electromagnetic cavities* is that whilst the theory can be applied to EM cavities with arbitrary characteristics, the measurements are performed on cavities with characteristics typical of vehicles, specifically road vehicles, and the example application is for a wireless system deployed in a road vehicle.

In this introduction:

- The motivation for undertaking this project is given,
- An outline of the thesis is presented,
- The main contributions are identified,
- The notation used throughout is defined.

1.1 Motivation

The motivation to undertake this project is threefold: the proposed research is relevant, novel and achievable.

Relevance: The research is relevant to current in-vehicle wireless communication system applications. In modern vehicles *infotainment* systems must coexist alongside vehicle radio, *Wi-Fi*, mobile telephones, *Bluetooth* headsets and Wireless Sensor Networks (WSNs). Specific examples of in-vehicle wireless communication systems are discussed in Chapter 2.

Novelty: Previous research typically focuses on deploying existing wireless systems in vehicles, and optimising their performance according to some measurement campaign and optimisation criteria. This contrasts with the approach taken here, where the underlying physical process is modelled, leading to a profound understanding of how to deploy optimal, or at least improved, wireless communication systems.

Achievability: The fundamental science of electromagnetics shows that it is possible to mathematically model a wireless propagation channel, and there is a strong precedent that mathematical optimisation of this abstracted model leads to tangible improvements in performance of actual deployed systems (i.e., for typical performance metrics such as latency, data-throughput and required transmission power). Furthermore existing work in the fields of EM propagation modelling, information theory and wireless communications indicates that it should be possible to express the abstracted model as a series of tractable expressions, that are expected, with a high degree of confidence, to lead to a useful outcome being achieved.

As previously mentioned, the theory has been derived to be valid for EM cavities in general, and thus this dissertation supports the measurement of and deployment of wireless communications systems in all EM cavities (i.e., not limited to vehicle cavities) should such an eventuality arise. Also, the EM propagation modelling contained in this dissertation could be used to successfully implement alternative wireless device system deployments, such as time-of-arrival positioning systems, should somebody so desire as to deploy one in an EM cavity.

1.2 Thesis outline

Following this introduction, an overview of the existing work in the area is given in Chapter 2, and details of the experimental methods are presented in Chapter 3. The core of the thesis is developed in Chapters 4 – 7, followed by conclusions in Chapter 8. Below, it is explained how these four core chapters (i.e., 4 – 7) combine to form the thesis.

EM wave propagation can be completely characterised by its time varying impulse response, $h_{\mathbb{H}}(t, \tau)$. If, for every object affecting the EM propagation (including the antennas), the geometry, position and material properties are known at every time instant then $h_{\mathbb{H}}(t, \tau)$ is a deterministic function. This assumption of determinism is, however, unrealistic for any real system. Therefore it is more reasonable to take a statistical approach, with the justification being that any real system will have incomplete information about $h_{\mathbb{H}}(t, \tau)$. Discussion as to whether $h_{\mathbb{H}}(t, \tau)$ is truly a random phenomenon, whilst academically interesting, is not the subject-matter of this dissertation, and a statistical framework is a valid way to model the partial information which the deployed system has regarding the channel state.

The theoretical derivation of the channel as a statistical process is undertaken under the following assumptions:

I. That which is known, is assumed to be known exactly.

II. That which is unknown, exactly corresponds to a random variable, characterised by a probability distribution whose parameters are known exactly.

III. The phenomena upon which the theoretical model is formulated is conditioned from a complete description of the actual physical reality.

In reality none of these three assumptions are necessarily correct, therefore an iterative approach is taken to ensure that the final propagation model is appropriate, this is summarised in Fig. 1.1. Chapter 4 details the channel propagation model characterisation, and in effect includes the final loop of the flowchart shown in Fig. 1.1.

The characterisation of the in-vehicle channel in Chapter 4 shows that it is reasonable to model the channel as underspread (i.e., the channel remains coherent for a time duration which is longer than its delay spread). In the infinite bandwidth limit, the capacity of an underspread channel approaches that of a channel with perfect receiver Channel State Information (CSI). In Chapter 5, a simple lower bound on the capacity is derived, to verify that for typical operating

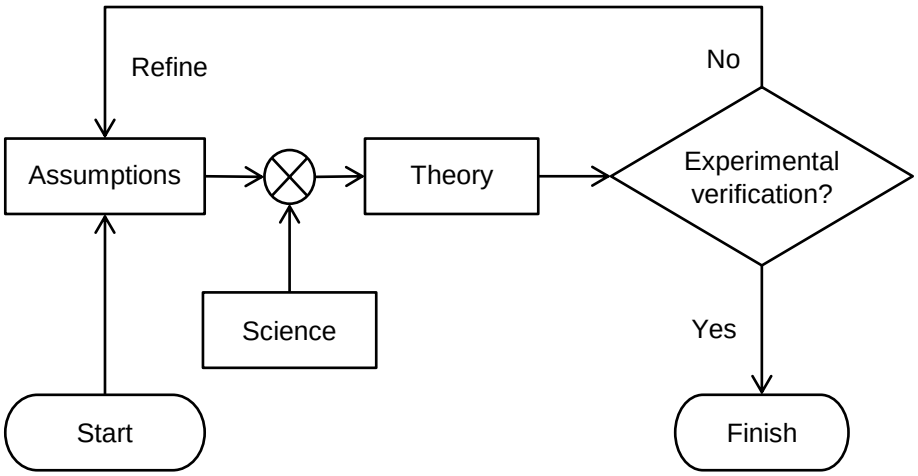

Figure 1.1: Flowchart of the propagation model

situations (i.e., coherence time, delay spread, bandwidth and Signal to Noise Ratio), the capacity of the in-vehicle channel is indeed approximately that of a channel with perfect receiver CSI.

Chapter 6 is essentially parallel to Chapter 5, and is concerned with the extent to which EM wave propagation in vehicle cavities is analogous to that in reverberation chambers. The motivation for this arises from noting that, ostensibly at least, the two environments share many similarities. The analogy between reverberation chambers and vehicle cavities yields a useful insight into the possible values of crucial communication parameters such as the delay spread, coherence distance and angular spread for wireless systems deployed in vehicles. Using the reverberation chamber type analysis to estimate these parameters, with only information that would typically be available to deployed wireless communication systems is the subject matter of Chapter 7. This validates the thesis, by demonstrating that the theoretical and experimental results concerning the fundamental nature of the EM propagation in vehicles can lead to tangible improvements in the performance of deployed wireless communication systems. Also presented in Chapter 7 is a heuristic method for channel prediction (i.e., as the in-vehicle channel varies with time).

Fig. 1.2 illustrates how these four technical chapters fit together to form the thesis. In general Chapter 7 could represent a more sophisticated wireless communication system than that presented in this dissertation, and in such an instance it may approach more closely the channel capacity evaluated in Chapter 5.

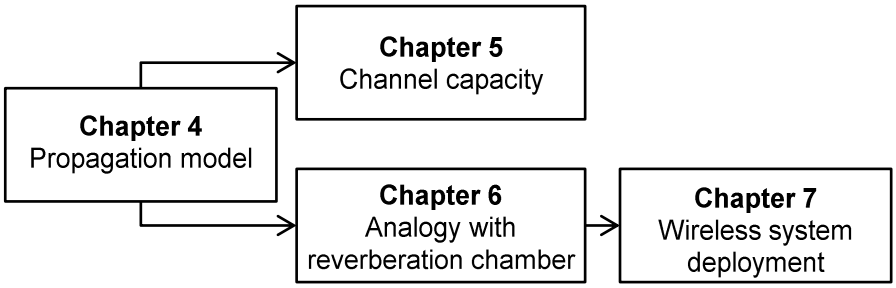

Figure 1.2: Thesis organisation

1.3 Main contributions

In the dissertation, the following contributions are made:

I. A statistical model for the instantaneous impulse response of an in-vehicle channel.

II. Rapid time variation of the in-vehicle channel characterised as a Doppler spread.

III. A simple method to calculate a lower bound on the information capacity of a highly underspread fading channel.

IV. A method for classifying EM cavities into three types, according to their propagation characteristics.

V. Time constant estimation for vehicle cavities, using data typically available to wireless communication systems.

VI. Slow time variation of the in-vehicle channel is characterised as a random process in the time domain.

1.4 Notation

As far as possible, this dissertation uses standard notation. Detailed below is the definition of some of the terms used, as well as an explanation of how complex numbers are handled. This section complements the Glossary, and the definitions within the body of the dissertation.

Convolution is denoted $*$, complex conjugation is denoted $(.)^*$, the transpose of a vector or matrix is denoted $(.)^T$, and the *Hadamard* (element-wise) product is denoted $\odot$. The magnitude of a complex number is denoted $|.|$, as is the determinant of a matrix, however it is always clear in context which is meant. $\langle . \rangle$ is used to denote the mean of some measured data.

Italicised and non-italicised symbols are used for frequency and time domain variables respectively (mainly in Chapter 5, which is has a large number of equations). Scalars are non-bold lower case, as in general are functions (i.e., x for the time domain, x for the frequency domain), vectors are bold lower-case (i.e., $\mathbf{x}$ for the time domain, $\boldsymbol{x}$ for the frequency domain), a single element from a vector or matrix is non-bold lower-case with subscript to denote its index (i.e., $\mathrm{x_i}$ for a vector and $\mathrm{x_{i,j}}$ for a matrix in the time domain; and x_i for a vector and $x_{i,j}$ for a matrix in the frequency domain), truncated vectors are bold lower-case with subscript to denote first element and superscript to denote final element (i.e., $\mathbf{x_i^j}$ for the time domain, $\boldsymbol{x}_{\boldsymbol{i}}^{\boldsymbol{j}}$ for the frequency domain) and matrices are upper-case (i.e., X for the time domain, X for the frequency domain).

Finally, it is convenient to represent complex numbers as vectors, and when multiplied together as a matrix acting on a vector. Letting x be a number, which in general may be complex:

$$\underline{x} = \begin{bmatrix} \mathrm{Re}(x) \\ \mathrm{Im}(x) \end{bmatrix},$$
$$\underline{X} = \begin{bmatrix} \mathrm{Re}(x) & -\mathrm{Im}(x) \\ \mathrm{Im}(x) & \mathrm{Re}(x) \end{bmatrix},$$

for example (letting z also be a number which in general may be complex):

$$z \times x = \underline{Z}\underline{x}.$$

This notation also generalises to complex vectors. Letting $\boldsymbol{x}$ be a vector of size n with each element in general a complex number:

$$\underline{\boldsymbol{x}} = \begin{bmatrix} \underline{x}_1 \\ \underline{x}_2 \\ \vdots \\ \underline{x}_n \end{bmatrix},$$
$$\underline{\boldsymbol{X}} = \begin{bmatrix} \underline{X}_1 & \underline{0} & \underline{0} & \cdots \\ \underline{0} & \underline{X}_2 & \underline{0} & \cdots \\ \underline{0} & \underline{0} & \ddots & \\ \vdots & \vdots & & \underline{X}_n \end{bmatrix}.$$

Coherence

The notion of *coherence* is used throughout this dissertation, specifically it has two distinct interpretations. In terms of power sources, two (or more sources) are coherent if their phase difference does not change with time. Whilst the term coherent is most easily understood in

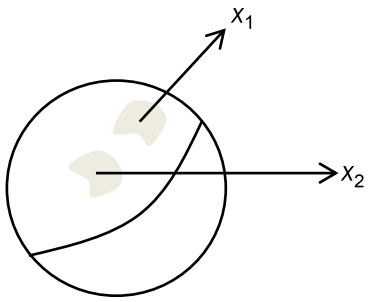

Figure 1.3: Radiation pattern of the coherent/ incoherent source model

terms of two or more sources, a single source can also be coherent. Consider dividing up the radiation pattern of a single source into an arbitrary number of elements. The source is said to be coherent if any two elements are coherent with zero phase difference. To illustrate this, Fig. 1.3 shows a source with two elements of the transmitted signal, x_1 and x_2. For a coherent source x_1 and x_2 are coherent, and the elements of the radiation pattern from which they originate can be at any location and can also be arbitrarily small. The term *incoherent* is used to denote one or more sources which are not coherent.

A perfectly incoherent isotropic point source is an important model which is used in this dissertation. This is used to denote the situation where any two infinitesimally small elements of the radiation pattern will be incoherent (i.e., Fig. 1.3 with x_1 and x_2 being incoherent and originating from arbitrarily small elements). Or, more simply, that it is simply a power source, and cannot be thought of meaningfully in terms of coherent transmission of a signal.

Coherence is also used in information theoretical analysis, where the coherent capacity is that where CSI is available at the receiver. The term *noncoherent* capacity is used to denote the situation where CSI is not available at the receiver.

Probability density functions

Throughout the dissertation, a number of Probability Density Functions (PDFs) are used without specific definition. For reference, these are detailed below.

- The PDF of a random variable, $\boldsymbol{x}$, of size k. Which has a multivariate Gaussian distribution, with mean, $\boldsymbol{\mu}$, and covariance matrix, Σ:

$$\mathcal{N}(\boldsymbol{x}; \boldsymbol{\mu}, \Sigma) = (2\pi)^{-\frac{k}{2}} |\Sigma|^{-\frac{1}{2}} e^{-\frac{1}{2}(x-\mu)^T \Sigma^{-1}(x-\mu)}.$$

- The PDF of a random variable, $\boldsymbol{x}$, of size k. Which has a multivariate complex Gaussian distribution, with mean, $\boldsymbol{\mu}$, covariance matrix, Γ, and relation matrix, $\mathrm{C} = \mathbb{E}((\boldsymbol{x}-\boldsymbol{\mu})(\boldsymbol{x}-\boldsymbol{\mu})^T)$:

$$\mathcal{CN}\left(\boldsymbol{x}; \boldsymbol{\mu}, \Gamma, \mathrm{C}\right) = \pi^{-k}\left(|\Gamma||\Gamma^* - \mathrm{C}^{*T}\Gamma^{-1}\mathrm{C}|\right)^{-\frac{1}{2}}\ e^{-\frac{1}{2}a},$$

  where:

$$a = \begin{bmatrix}(\boldsymbol{z}-\boldsymbol{\mu})^* \\ \boldsymbol{z}-\boldsymbol{\mu}\end{bmatrix}^T \begin{bmatrix}\Gamma & \mathrm{C} \\ \mathrm{C}^{*T} & \Gamma^*\end{bmatrix} \begin{bmatrix}\boldsymbol{z}-\boldsymbol{\mu} \\ (\boldsymbol{z}-\boldsymbol{\mu})^*\end{bmatrix}.$$

- The PDF of a random variable, $\boldsymbol{x}$, which has a Rayleigh distribution with parameter σ:

$$\mathcal{R}(x;\sigma) = \frac{x}{\sigma^2}e^{-\frac{x^2}{2\sigma^2}}.$$

Chapter 2

Existing research in the field

Wireless systems are increasingly deployed in vehicles: black-box event data recorders; *Wi-Fi*; various *Bluetooth* devices; mobile phones; vehicle radio; and Wireless Sensors Networks (WSNs) are all already commonplace, or expected to be in the near future [1–15].

The desire of manufacturers and users to deploy wireless devices in vehicles provides ample motivation for investigating and characterising the Electromagnetic (EM) environment in vehicles. Moreover, once this has been achieved an important performance metric is the channel information capacity. An alternative approach is to deploy existing wireless systems in vehicles under a range of operating scenarios, and to measure their performance.

This chapter presents the existing literature on these topics, and important insufficiencies have been identified.

2.1 Electromagnetic field distribution and propagation modelling in cavities

The action of a wireless communication channel can be described as a linear integral operator $\mathbb{H}$, which can be expressed in terms of its time varying impulse response $h_{\mathbb{H}}(t, \tau)$ [16]. Should this be known (either as a deterministic or a random function) then the characterisation of the EM wave propagation is complete, however this is not currently the case. There is existing work concerning the steady-state behaviour of EM cavities (i.e., if $h_{\mathbb{H}}(t, \tau)$ is time-invariant) particularly the steady-state Electric Field (EF) distribution for a constant wave input, and this in turn sheds some light on the steady-state EM wave propagation. There is also some existing work concerning the time-variation of EM propagation in EM cavities under certain specified assumptions, and by introducing time variation it is possible to gain a further insight into how the actual in-vehicle channel may behave.

2.1.1 Steady-state in-vehicle electric field distribution

In much of the literature there is an implicit assumption that the EF distribution in a vehicle cavity will be analogous to that in an EM reverberation chamber [17], albeit with a much lower Quality Factor (QF). Indeed, it could almost be argued that if this were not the case, then there would be little point in modelling the EF distribution at all, the more conventional approach (within the field of wireless communication) of modelling the time-varying impulse response would suffice. Nonetheless, the evidence for modelling the vehicle cavity as an EM cavity with a QF is compelling, and this provides a logical starting point for reviewing the existing literature.

For any given reverberation chamber, a Lowest Usable Frequency (LUF) and a working volume will be defined (i.e., the volume of the chamber a certain distance away from the walls). For operation at a frequency above the LUF, and within the working volume there are five important properties:

I. The energy, E, retained at a time delay, τ, after a unit impulse input of energy at $\tau = 0$ can be expressed as:

$$\mathrm{E} = ke^{-\frac{\tau}{\tau_c}}, \tag{2.1}$$

where k is a constant, and τ_c is the cavity time constant.

II. The reverberation chamber is an isolated EM environment.

III. The EF distribution is isotropic, i.e., it has six components (a real and imaginary part for each of three Cartesian dimensions) which are Independent Identically Distributed (IID) Gaussian random variables.

Figure 2.1: Stirrer in the National Physical Laboratory reverberation chamber

IV. The EF distribution is homogeneous, i.e., the same isotropic distribution is found at all locations within the working volume.

V. The EF distribution is ergodic, i.e., the same isotropic distribution is found if the EF is sampled by varying frequency, or time. This applies when a time variation of the EF is introduced by deploying a stirrer in the cavity, which is a large irregular reflective rotating object. An example of which is shown in Fig. 2.1. An EF which has properties III – V is known a *uniform* EF [18].

These properties lead to a number of methods to evaluate the QF (Q) of a reverberation chamber, there are also existing examples of the QF being evaluated in vehicles. Typical equations that might be used to evaluate the QF include the following four examples (see Table 2.1 for the relevant references):

I. By finding the average power (for a reverberation chamber with arbitrary geometry):

$$Q = \frac{16\pi^2 V}{\eta_{\mathrm{Tx}}\eta_{\mathrm{Rx}}\lambda^3}\left\langle\frac{\mathrm{P_{Rx}}}{\mathrm{P_{Tx}}}\right\rangle, \tag{2.2}$$

where V is the cavity volume; η_{Tx} is the transmit antenna efficiency; η_{Rx} is the receive antenna efficiency; λ is the wavelength; $\mathrm{P_{Rx}}$ is the received power; and $\mathrm{P_{Tx}}$ is the transmitted power. The average $\langle \mathrm{P_{Rx}}/\mathrm{P_{Tx}}\rangle$ takes place over a sufficient number (usually 200 or more) of independent field realisations, which is typically achieved in a reverberation chamber by using a stirrer. The transmit and receive antennas are located within the working volume such that the stirrer obscures the Line-of-Sight between the two.

II. Using the cavity time constant:

$$Q = 2\pi f \tau_c, \tag{2.3}$$

where f is frequency. This method requires τ_c to have first been estimated (note that (2.3) is an important equality which is why it has been included here in spite of it not used in the literature summarised in Table 2.1).

III. Evaluating the QF for each mode:

$$Q = \frac{f_r}{f_u - f_l}, \tag{2.4}$$

where f_r is the resonant frequency, f_u is the upper -3 dB cut-off frequency, and f_l is the lower -3 dB cut-off frequency.

IV. By evaluating the losses:

$$Q = \frac{8\pi V f}{c \sum_i A_i w_i}, \tag{2.5}$$

where c is the speed of light. The variable i is introduced to distinguish parts of cavity wall through which energy is lost with different values of wall loss (which in general could include apertures), each of these parts has area A; and wall loss w.

The reverberation chamber has been developed primarily as a controlled environment for Electromagnetic Compatibility testing [17], however the theory also has implications for communication systems deployed in EM cavities, most obviously owing to the fact that the QF is related to the channel delay spread (i.e., through (2.1)) and thus the channel coherence bandwidth. The cavity QF is also relevant because the channel information capacity will depend on its time varying impulse response (which is again related to the QF through (2.1)). Consequently there is a clear motivation for wireless communication engineers to measure typical in-vehicle QFs, and a summary of their results is shown in Table 2.1 (the value of the QF for a reverberation chamber would typically be 10 – 1000 times greater than those in Table 2.1 [[18] Fig. 7.13]). It should be noted that for reverberation chambers, the LUF can be determined from the cavity geometry, however there are no existing evaluations of typical values of the LUF for vehicle cavities.

In-vehicle EF distributions have also been investigated for the purpose of assessing the specific absorption rate and field exposure threat in the *SEFERE* project [22], and there is some overlap with this programme of work. This is because it is relevant to assess in-vehicle EF distributions for the purpose of deploying effective communication systems.

Table 2.1: Quality factor estimation.

Reference	**Frequency / GHz**	**Quality factor**	**Equation**
Heddebaut *et al.* [10]	0.7 – 6	8 – 1100	(2.2)
Delangre *et al.* [19]	4.9 –5.1	77.5 – 255	(2.2)
Weng *et al.* [20]	0.072 – 0.303	4 – 40	(2.4)
Ruddle [21]	0 – 6	10 – 1000	(2.5)

2.1.2 Steady-state in-vehicle electromagnetic wave propagation

As for the EF distribution, the analogy with reverberation chambers dominates much of the published work concerning the steady-state propagation of EM waves in vehicle cavities [9, 19, 23–25]. In these works it is reasoned that the exponential decay is a good fit for the arriving power, and no attempt has been made to resolve arriving rays, either experimentally or theoretically.

Another approach [26–34] is to adapt the Saleh-Valenzuela indoor propagation model [35] to fit the in-vehicle environment. This is justified by reasoning that the in-vehicle environment shares many propagation characteristics with the indoor environment. This approach yields some success, however it is somewhat tenuous to suggest that in general the in-vehicle environment provides the clustered structure upon which the Saleh-Valenzuela model relies. Also, it should be noted that these works deal with the *intra-vehicular* propagation environment which is usually defined for any pair of transmit-receive antennas operating on a single vehicle. In such situations one or both of the antennas could potentially be located on the outside of the vehicle, and thus the EM waves do not necessarily propagate through the cavity for all the scenarios considered by these authors. Crucially the Saleh-Valenzuela model is not, in general, consistent with the exponentially decaying model for energy retained in the cavity, and thus there is no existing model for in-vehicle EM wave propagation expressed in terms of ray arrivals which is consistent with the accepted EM cavity model for energy retained.

Another important aspect of the steady-state EM wave propagation is the angular spread of the arriving energy. Generally, a reasonable approach is to assume that if there exists a line-of-sight between the transmitter and receiver, then EM waves propagating along this direction will dominate, and if not then the direction of maximum arriving energy is random and uniformly distributed. The measurements presented by Sawada *et al.* [34] demonstrate that this would appear to be a reasonable assumption for propagation in vehicle cavities, although there is some directional non-uniformity arising from reflective paths.

2.1.3 Time variation of the in-vehicle electromagnetic environment

As identified in Section 2.1.2 there is a paucity of literature concerning the steady state impulse response of EM cavities, it is therefore unsurprising that there is no work on the time varying impulse response, $h_{\mathbb{H}}(t, \tau)$. Instead the literature on the time variation of the EM environment in EM cavities focuses on characterising the time variation either in terms of the stability of communication channels in cavities; or evaluating the Doppler shifts associated with stirrer and antenna motion in the reverberation chamber.

It is not necessarily important to unify these two approaches in order to find a general expression for $h_{\mathbb{H}}(t, \tau)$, as the extent of the possible channel variation for all time is vast and thus a statistical characterisation would have to be so general it would be practically useless. Moreover the purpose of understanding the time variation is itself two-fold: the slow channel variation, characterised as channel stability in the time domain is required to tackle wireless communication system deployment challenges; whereas the rapid channel variation, characterised as a Doppler spread is required to evaluate the channel capacity.

The channel stability has been characterised in terms of the coherence time of in-vehicle channels [36, 37], with values typically in the range 1 – 10 s for vehicles whilst being driven, and greater than 100 s for stationary vehicles. An alternative approach, taken by Heddebaut *et al.* [10], is to evaluate the ratio of link energy which varies compared to that which does not, yielding experimental values in the range 12 – 20 dB.

There is extensive literature available on characterising the Doppler spread in reverberation chambers [38–43], and the relevant findings can be summarised thus:

I. The power spectral density has a maximum at 0 Hz Doppler shift and decreases with the magnitude of the Doppler shift frequency. This is the case for both the stirrer moving [38–43], and also for the case when one of the antennas is moving [39].

II. The maximum Doppler shift is proportional to the transmission (carrier) frequency [39–41].

III. The maximum Doppler shift decreases with cavity loading (i.e., the volume of absorptive material within the cavity) [40].

IV. The stirring can be modelled as an Uncorrelated Scattering (US) process [38].

2.2 Information theoretic analysis on the channel capacity

In his seminal 1948 paper [44], Shannon builds on previous work, including important contributions by Nyquist [45, 46] and Hartley [47], to derive the information capacity of a continuous waveform channel with constant channel frequency response, and perfect receiver Channel State Information (CSI):

$$C = W \log_2 (1 + \text{SNR}) \ \text{bit}\,\text{s}^{-1}, \tag{2.6}$$

where C is the capacity, W is the bandwidth and SNR is the Signal to Noise Ratio.

Gallager also presents a rigorous and intuitive derivation of this result [48]. The capacity in (2.6) can be generalised for a time-invariant frequency selective fading channel, with perfect receiver CSI [48, 49]:

$$C = W\mathbb{E}_f \left(\log_2 \left(1 + |T_{\mathbb{H}}(f,t)|^2 \text{SNR}\right)\right) \ \text{bit}\,\text{s}^{-1}, \tag{2.7}$$

where $T_{\mathbb{H}}(f,t)$ is in general the time-varying frequency response (which in this case is time-invariant).

For noncoherent (i.e., without assuming *a priori* receiver CSI) Wide-Sense Stationary Uncorrelated Scattering (WSSUS) channels, it is accepted that for a large bandwidth, the capacity stated in (2.7) can be approached, if the channel varies slowly relative to its delay spread, which is known as the *underspread* condition [49]. The measurements presented in this dissertation, as well as the previous material discussed in Section 2.1 indicate that under normal operating circumstances the in-vehicle channel can be approximated as a WSSUS underspread channel.

2.2.1 Capacity of the underspread channel

Durisi *et al.* [50–52] have led the way in deriving upper and lower bounds on the capacity for WSSUS underspread channels. By transmitting and receiving the symbols on a Weyl-Heisenberg set, which is well-localised in time and frequency, the authors obtain the lower and upper bounds on the channel capacity. The lower bounds are more relevant, as (2.7) is itself an upper bound on the capacity.

The lower bound $\mathrm{L}_1(W)$ defined in [[50] Equation (39)] is a tight lower bound, but the authors acknowledge that it may be computationally difficult to evaluate when parameter values from actual channels are substituted in. They therefore propose a second lower bound $\mathrm{L}_2(W)$ [[50] Equation (48)] where they have sacrificed some tightness to make it less complicated computationally. The authors have included a peak power constraint, which complicates the

expressions for $\mathrm{L}_1(W)$ and $\mathrm{L}_2(W)$ and is not required for a simple channel capacity evaluation. Also, the derivation starts from a general case of the underspread channel, whereas they note that in reality actual channels tend to be highly underspread. It is therefore possible that, by taking these two factors into account, a less computationally demanding lower bound could possibly be found. Durisi *et al.* also propose two other approximate lower bounds, L_a and L_{aa} [50], however these are not strict lower bounds, and thus are not discussed here.

2.2.2 Capacity of the overspread channel

It is the case that for a channel with an infinite impulse response, such as the in-vehicle channel, the underspread condition is only an approximation, which is implicitly SNR dependent (i.e., because after a certain delay, the impulse response will be negligible compared to the noise floor, and thus can be truncated without significantly changing the final result). In general, for arbitrary SNR, the in-vehicle channel is overspread (i.e., as the impulse response is modelled as infinite it is necessarily greater than the channel coherence time). Characterising the capacity of the overspread channel remains an interesting open problem.

Koch and Lapidoth [53] have made progress with a related problem, where a discrete representation of the channel is characterised. Whilst the notion of channel spread cannot be directly applied to discrete channels, the channel in [53] has a time varying infinite impulse response, and therefore shares some similarities with the overspread channel, and the results of the characterisation of this channel may shed some light on what to expect from the continuous overspread channel. Specifically, the authors derive that for a channel whose impulse response decays exponentially or slower the capacity is bounded in the SNR.

Salim and Slock [54,55] take a similar approach, noting that from previous work on the discrete channel [56–58] that they expect the capacity of the overspread channel to grow as $\log(\log(\mathrm{SNR}))$ at high SNR. However they then go on to show that under certain operating circumstances, specifically for critically spread and slightly overspread channels, the capacity may grow proportionally with $\log(\mathrm{SNR})$ at high SNR.

The conclusion then, is that whilst for current applications the underspread capacity is a very good approximation, if in the future applications operate at much higher values of SNR, or in much more rapidly varying environments, then it will be necessary to ascertain the capacity of the overspread channel.

2.3 Deployment of wireless systems in vehicles

A different approach (i.e., as opposed to characterising the in-vehicle EM wave propagation environment and channel information capacity) is to deploy existing wireless communication systems in vehicles, and to evaluate their performance under a range of operating conditions [9, 36,59–61]. These studies show that existing wireless communication systems work in vehicular environments, and there have been a number of specific insights:

I. For a *Zigbee* [62] system the Packet Error Rate (PER) increases with the QF [9].

II. For a Binary Phase Shift Keying system operating at 915 MHz a PER of 1 – 14 $\%$ can be achieved, with a maximum packet delay smaller than 500 ms [36].

III. For a Zigbee system a PER of 1 – 10 $\%$ can be achieved with a peak packet delay of 60 – 200 ms and an average packet delay smaller than 3 ms [59].

IV. The node locations and engine noise have a significant effect on link quality for a Zigbee system [60].

V. A Software Defined Radio can be used to simulate an in-vehicle WSN [61].

2.4 Chapter summary

The literature concerning the in-vehicle EM wave propagation environment, the in-vehicle wireless channel information capacity, and wireless communication systems deployed in vehicles has been reviewed. Regarding the in-vehicle EM wave propagation environment, the most common and successful method proposed in the literature is to assume that it is analogous to that in a reverberation chamber, and thus perform the analysis accordingly. Regarding the in-vehicle wireless channel information capacity, good results have been achieved by treating the channel as underspread, and using this property to derive lower and upper bounds (i.e., on the capacity). Regarding the deployment of wireless communication systems in vehicles, several case-studies have been undertaken, showing that existing wireless communication systems work in vehicular environments, as well as yielding more specific insights.

The literature appears to have the following important deficiencies: An EM wave propagation model which can be used to characterise the ray arrival process and the time-variation of the in-vehicle channel, and an investigation into to what extent the in-vehicle EM wave propagation environment is analogous to that in a reverberation chamber. Also, the underspread channel model is very general, and it may be possible to evaluate the capacity more easily using the

specific statistical propagation properties of the in-vehicle channel. It would be of interest to investigate whether the fundamental characterisation of the in-vehicle EM wave propagation environment and channel capacity could lead to improved performance of an actual wireless system.

Chapter 3

Experimental methods and simulations

As explained in Chapter 1, the time-varying impulse response can be considered to be a random process. Chapter 4 presents a theoretical derivation of an appropriate parameterisation of this random process, and the primary purpose of the experiments is to support the theory as demonstrated in Fig. 1.1. This is achieved by undertaking measurements in a range of environments which were judged to be representative of typical vehicle cavities. The work presented in Chapter 6 builds on this parameterisation to investigate the possible analogy between vehicle cavities and reverberation chambers.

A secondary purpose of the experiments is to investigate whether this channel model can lead to an improved performance of an actual wireless system deployed in a vehicle. This is achieved by estimating the random process parameters solely from channel measurements which would typically be available to an actual wireless systems.

3.1 Environments

Two environment types were investigated to characterise the Electromagnetic (EM) wave propagation in vehicle cavities and assess the performance of in-vehicle wireless communication systems. Firstly, a vehicle-like cavity developed and used by the *SEFERE* project [22, 63] which provided a simulation of the in-vehicle environment. The vehicle-like cavity was located in a fully anechoic chamber, enabling the measurements to be undertaken in a temperature controlled environment which has an isolation of at least 100 dB from the external environment. Secondly, two actual vehicles (a panel van and an estate car) in which some precision was lost (as the vehicles were outside and thus exposed to interference and noise) but which provided the ground truth.

3.1.1 Vehicle-like cavity

The vehicle-like cavity was located in the National Physical Laboratory Small Antenna Radiated Testing range, which is a fully anechoic chamber [64, 65]. This controlled environment allowed the experiments to be undertaken using precision measurement equipment, and with a very low noise floor (i.e., close to the thermal noise floor). Throughout the dissertation, the vehicle-like cavity is sometimes referred to by the abbreviation *Cavity* or *Cav*.

Fig. 3.1 shows a photograph and plan-view of the vehicle-like cavity, with the origin and axes defined, also shown are locations $P_{Cav\,1}$, $P_{Cav\,2}$, $P_{Cav\,3}$ and $P_{Cav\,4}$, denoted 1, 2, 3 and 4 respectively. The cavity has dimensions 1260 mm $\times$ 1050 mm $\times$ 1220 mm ($x \times y \times z$). It has four rectangular apertures with corners located at:

- (0, 230, 700) mm, (0, 230, 1000) mm, (0, 820, 700) mm, (0, 820, 1000) mm,
- (1260, 230, 700) mm, (1260, 230, 1000) mm, (1260, 820, 700) mm, (1260, 820, 1000) mm,
- (230, 0, 700) mm, (230, 0, 1000) mm, (1030, 0, 700) mm, (1030, 0, 1000) mm,
- (230, 1050, 700) mm, (230, 1050, 1000) mm, (1030, 1050, 700) mm, (1030, 1050, 1000) mm.

Within the vehicle-like cavity, additional items were introduced to vary the internal EM wave propagation environment: units of Radiation Absorbent Material (RAM); a small stirrer; and a head and torso solid anthropomorphic phantom placed on a car seat. These are shown in

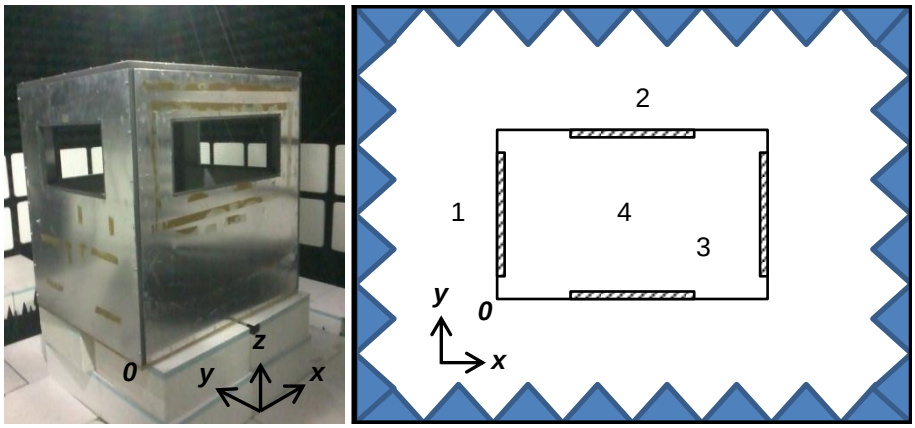

Figure 3.1: Vehicle-like cavity

(a) (b) (c)

Figure 3.2: Items located in the vehicle-like cavity: (a) a single unit of RAM; (b) stirrer; (c) phantom

Fig. 3.2 (a), (b) and (c) respectively.

A single unit of RAM consists of a square based pyramid with base of side 150 mm and vertical height of 390 mm, on top of a cuboid of height 50 mm. The stirrer was designed to mimic the reverberation chamber stirrer shown in Fig. 2.1, and was capable of constant rotation at a range of speeds (up to 0.19 revolutions per second for the measurements conducted). The stirrer has a height of 410 mm and a radius of 180 mm, and when placed in the cavity stands 325 mm off the cavity floor. The human phantom has the same dielectric properties as human muscle tissue [66], and the car seat is from an actual vehicle.

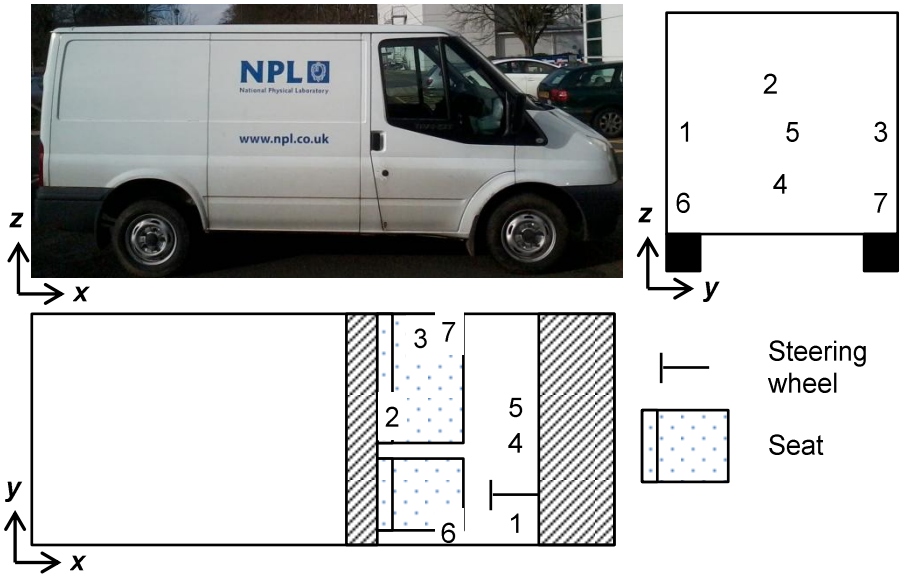

Figure 3.3: Panel van

3.1.2 Actual vehicles

The panel van is shown in Fig. 3.3, which throughout the dissertation is sometimes referred to by the abbreviation *Van*. Also shown in Fig. 3.3 are axis definitions and antenna locations where the numbers 1 to 7 represent locations $P_{Van\,1}$, to $P_{Van\,7}$ respectively. The antenna locations have been chosen to be well spread throughout the cabin, and with some close to the cavity walls. The internal volume of the van cabin is estimated to be 3.57 m^3, and the internal volume of the rear of the van is estimated to be 6.38 m^3. It should be noted that part way through the programme of experiments the van was replaced by a slightly different model, however this appeared to have minimal effects on the measured data.

The estate car is shown in Fig. 3.4, which throughout the dissertation is sometimes referred to by the abbreviation *Car*. Also shown are axis definitions and antenna locations where the numbers 1 to 6 represent locations $P_{Car\,1}$ to $P_{Car\,6}$ respectively. Again, the antenna locations have been chosen to be well spread throughout the car, and with some close to the cavity walls. The internal volume of the car is estimated to be 3.11 m^3.

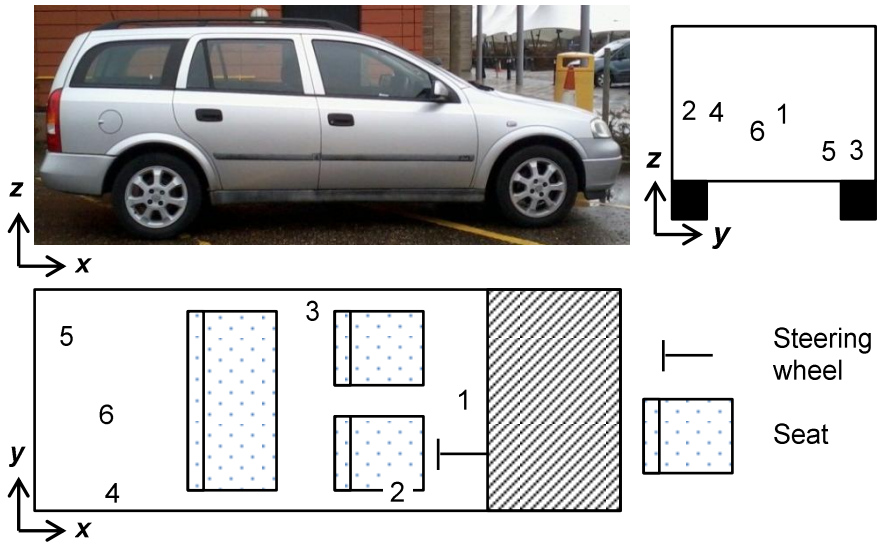

Figure 3.4: Estate car

3.2 Measurement campaigns

The majority of the experiments undertaken to achieve the first objective, that is to perform measurements to support the theoretical channel model, were performed using precision measurement equipment. This included the measurement of scattering parameters (SPs) using a Vector Network Analyser (VNA), and the measurement of Doppler spread using a Spectrum Analyser (SA). For the second objective, estimating the channel parameters using measurements typically available to wireless communication system, both precision measurement equipment and a wireless network development kit were used.

3.2.1 Scattering parameter measurements

Scattering parameters for the Environment Under Test (EUT) were measured using various VNAs. In each case, the ports were referred to the ends of the co-axial cables used to connect the antennas, and a full calibration was performed (which was assumed to be perfect). The measurement set-up is shown in Fig. 3.5.

The SP Matrix (SPM, S) is defined as:

$$S = \begin{bmatrix} S_{11} & S_{12} \\ S_{21} & S_{22} \end{bmatrix}, \tag{3.1}$$

where, in general for a VNA that has more than two ports, it should be noted that the SPM can be between any pair of ports, not just Ports 1 and 2.

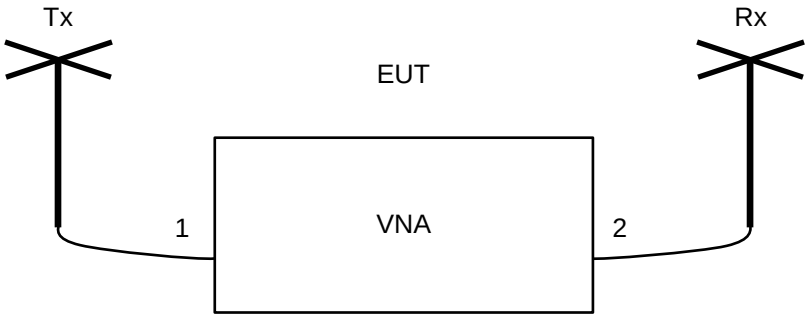

Figure 3.5: Scattering parameter measurement set-up

Sometimes it is sufficient to find only S_{21} of the EUT ($S_{21\,\mathrm{EUT}}$), in which case a good approximation (i.e., for antennas with low return loss) can be found using:

$$S_{21\,\mathrm{EUT}} \approx \frac{S_{21\,\mathrm{meas}}}{\sqrt{\eta_{\mathrm{Tx}}\eta_{\mathrm{Rx}}}}, \tag{3.2}$$

where $S_{21\,\mathrm{meas}}$ is the value of S_{21} measured by the VNA, η_{Tx} is the transmit antenna efficiency and η_{Rx} is the receive antenna efficiency.

To precisely calculate the whole SPM, it is necessary to treat each component in Fig. 3.5 as a two-port scattering network, including the antennas. $S_{11\,\mathrm{ant}}$ of an antenna can be measured using a single port of a VNA, and the efficiency of an antenna, η_{ant}, can also be measured using a standard technique in a reverberation chamber or anechoic chamber. Using a method adapted from that of Prakoso *et al.* [67] it is possible to use $S_{11\,\mathrm{ant}}$ and η_{ant} to express the full two-port SPs of the transmit and receive antennas (note in general $S_{11\,\mathrm{ant}}$ and η_{ant} need not be the same for the transmit and receive antennas):

Transmitter:

$$S_{11} = S_{11\,\mathrm{ant}}, \tag{3.3}$$

$$S_{12} = S_{21} = \sqrt{\eta_{\mathrm{ant}}}\frac{1 - S_{11\,\mathrm{ant}}}{|1 - S_{11\,\mathrm{ant}}|}, \tag{3.4}$$

$$S_{22} = 0. \tag{3.5}$$

Receiver:

$$S_{11} = 0, \tag{3.6}$$

$$S_{12} = S_{21} = \sqrt{\eta_{\mathrm{ant}}}\frac{1 - S_{11\,\mathrm{ant}}}{|1 - S_{11\,\mathrm{ant}}|}, \tag{3.7}$$

$$S_{22} = S_{11\,\mathrm{ant}}. \tag{3.8}$$

Using an alternative matrix S' to represent the SPs:

$$S' = \begin{bmatrix} S_{12} - \frac{S_{11}S_{22}}{S_{21}} & \frac{S_{22}}{S_{21}} \\ -\frac{S_{11}}{S_{21}} & \frac{1}{S_{21}} \end{bmatrix}, \tag{3.9}$$

it is possible to find the SPs of the EUT:

$$S'_{\text{meas}} = S'_{\text{Tx}} S'_{\text{EUT}} S'_{\text{Rx}}, \tag{3.10}$$

$$\implies S'_{\text{EUT}} = (S'_{\text{Tx}})^{-1} S'_{\text{meas}} (S'_{\text{Rx}})^{-1}. \tag{3.11}$$

Three models of antenna were used: Schwarzbeck 9112 biconical antennas (SB9112) [68], Schwarzbeck 9113 biconical antennas (SB9113) [69], and low-profile printed patch-type antennas based on those proposed by Delaveaud *et al.* [70], Conway *et al.* [71, 72] and Chandran *et al.* [73] (this antenna is shown in Fig. 3.7 (a), and is referred to as *patch*). All three models of antenna have an omnidirectional radiation pattern, and their orientation (i.e., relative to the Cartesian axes defined for each environment in Section 3.1) is referred to as *x*-polarised, *y*-polarised or *z*-polarised for direction of maximum Electric Field (EF) parallel to the x, y and z axes, respectively. The parameters η_{ant} and $S_{11\,\text{ant}}$ were measured for each antenna model, and total and reflection efficiencies are detailed in Appendix A.

Full details of the SP measurements undertaken are given in Table 3.1. For the column headed 'location', the co-ordinates in brackets (where applicable) are in millimetres, relative to the origin (see Figs. 3.1, 3.3 and 3.4), and the letter x, y or z refers to the polarisation of the antenna. Various VNAs were used for the measurement campaigns: an Agilent N5242A 2-port VNA; a Rohde & Schwarz ZVB8 4-port VNA; a Rohde & Schwarz ZVB8 2-port VNA; and a Rohde & Schwarz ZVRE 2-port VNA. The letter 'P' refers to the VNA port. SP measurements were undertaken for a number of different purposes:

I. To infer a detailed impulse response (Measurement Campaign 1.1): two orthogonal orientations of the antenna connected to Port 2 were measured, and the stirrer was also rotated to a different position for the second measurement (however whilst each measurement was taking place, the stirrer was switched off). The stirrer obscured the Line-of-Sight (LOS) between the two ports. Only for inferring a detailed impulse response was it necessary to use (3.11) rather than the simpler expression (3.2).

II. To infer a coarse impulse response (Measurement Campaigns 1.2, 1.3, 1.4 and 1.5): for Measurement Campaign 1.2, the vehicle-like cavity was used with the stirrer obscuring the LOS and switched off; for Measurement Campaigns 1.3 and 1.5 the antenna attached to Port 1 was positioned at a known location, and the antenna attached to Port 2 was then positioned at six different (unrecorded) arbitrary locations, with arbitrary orientation. For Measurement Campaign 1.4 both Port 1 and Port 2 antennas were placed at arbitrary locations and orientations.

III. To investigate the EF distribution (Measurement Campaign 1.2): the stirrer was set to constantly rotate at 0.0044 revolutions per second, yielding approximately 100 recorded SP measurements per revolution. The stirrer was located such that it obscured the LOS between Port 1 (which acted as the transmitter) and each of the other three ports (which acted as receivers).

IV. To investigate whether the vehicle cavity can be treated as an isolated environment (Measurement Campaign 1.6): frequency sweeps were taken for a number of scenarios with an object outside the cavity (as well as a measurement with no external objects for reference). In Table 3.1, 'Man' refers to a person standing at the referenced location, approximately 100 mm from the cavity aperture and 'Metal' refers to a person standing at the referenced location holding a large metal panel parallel to the cavity approximately 100 mm from the cavity aperture.

V. To mimic a *Zigbee* [62] based Wireless Sensor Network (WSN) (Measurement Campaigns 1.7 and 1.8): SPs were measured for the *802.15.4* [74] channel frequencies. In the car measurements were taken for antenna locations covering every pair-wise combination of $P_{\text{Car}\,1}$ to $P_{\text{Car}\,5}$, and in the van for every pair-wise combination of $P_{\text{Van}\,1}$ to $P_{\text{Van}\,4}$.

For the measurements undertaken using the Rohde and Schwarz ZVB8 (4-port) VNA, there was apparently a phase offset in the measured data. This manifested itself as a time shift in plots in the time domain (i.e., when an inverse discrete Fourier transform was performed on the data). It is, however, the shape of the plot in the time domain, not the absolute time at which it occurs, which is relevant for the analysis detailed in this dissertation. Comparing the measurements undertaken by the Rohde and Schwarz ZVB8 (4-port) VNA with those undertaken by other VNAs in the same environments showed that the shape of the plot is the same for each. It can therefore be concluded that there is no adverse effects of this apparent issue with the Rohde and Schwarz ZVB8 (4-port) VNA, and for the remainder of this dissertation, the results are presented with the time shift removed.

Table 3.1: Scattering parameter measurements.

Campaign	**Environment**	**Frequency**	**Antenna**	**Location**	**Loading**	**SP Equation**	**VNA**
1.1	Cavity	4 – 17 GHz, 1 MHz step	SB9112	P1: (860,920,650) x P2: (170,120,650) x, z	Phantom: $P_{Cav\,3}$ Stirrer (off): $P_{Cav\,4}$	(3.11)	N5242A (2-port)
1.2	Cavity	0.5 – 3 GHz, 5 MHz step	SB9113	P1: (1020,880,510) x, z P2: (300,490,440) z P3: (256,210,810) x P4: (300,470,440) y	(0, 4, 8, 12 units of RAM) & Stirrer: $P_{Cav\,4}$	(3.2)	ZVB8 (4-port)
1.3	Van (front)	1 – 3 GHz, 5 MHz step	SB9113	P1: $P_{Van\,7}$ P2: 6 locations	0 – 3 occupants	(3.2)	ZVB8 (2-port)
1.4	Van (rear)	1 – 3 GHz, 5 MHz step	SB9113	P1, P2: 6 pairs of locations	n/a	(3.2)	ZVB8 (2-port)
1.5	Car	1 – 3 GHz, 5 MHz step	SB9113	P1: $P_{Car\,6}$ P2: 6 locations	0 – 5 occupants	(3.2)	ZVRE (2-port)
1.6	Cavity	1 – 3 GHz, 5 MHz step	SB9113	P1: (930,750,585) x P2: (330,210,500) x	n/a; Man: $P_{Cav\,1}$; Metal: $P_{Cav\,1}$; Metal: $P_{Cav\,2}$	(3.2)	N5242A (2-port)
1.7	Van (front)	2.405–2.48GHz 5 MHz step	patch	$P_{Van\,1} - P_{Van\,4}$	n/a	(3.2)	ZVB8 (2-port)
1.8	Car	2.405–2.48GHz 5 MHz step	patch	$P_{Car\,1} - P_{Car\,5}$	n/a	(3.2)	ZVRE (2-port)

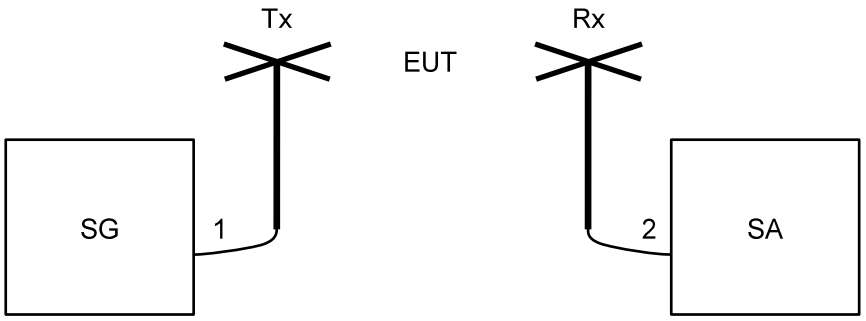

Figure 3.6: Spectrum measurement set-up

3.2.2 Spectrum measurements

Spectrum measurements were undertaken to investigate the Doppler spread resulting from four types of channel variation:

I. A moving absorptive object, i.e., a person, in the cavity (referred to as 'absorptive').

II. A moving reflective object, i.e., the stirrer shown in Fig. 3.2 (b), operating at 0.19 revolutions per second located at $P_{Cav\,4}$ (referred to as 'reflective').

III. One of the antennas moving (referred to as '1 antenna').

IV. Both antennas moving (referred to as '2 antennas').

The experimental set-up consisted of a transmit antenna, connected via co-axial cable to a Signal Generator (SG) providing a Constant Wave, and a receive antenna connected via co-axial cable to an *Agilent E4440A* Spectrum Analyser (SA), as shown in Fig. 3.6. For each campaign, the SA was set to record either a single sweep, or the average over a number of sweeps (either 25 or 50, though the actual number made little difference to the observed results).

The spectrum measurements undertaken are detailed in Table 3.2. For the measurements where one or both antennas are moved, the antenna location and orientation given is approximate (and where applicable is in millimetres). The stirrer remained in the cavity for all campaigns (switched off for all but the reflective stirring measurement), and its position was such that it obscured the direct LOS between the transmit and receive antennas.

Table 3.2: Spectrum measurements.

Campaign	Environment	Frequency / GHz	Antenna	Location	Loading	Variation	Sweep
2.1	Van	2.45	SB9113	Tx: $P_{\text{Van }5}$ Rx: $P_{\text{Van }6}$	1 person	Absorptive	Average
2.2	Cavity	2.45	SB9113	Tx: (850,760,660) x Rx: (180,760,660) x	n/a	Absorptive Reflective 1 antenna 2 antennas	Average
2.3	Cavity	3, 6, 9, 12, 15	SB9112	Tx: (180,160,830) x Rx: (980,910,510) x	0, 4, 8, 12 units of RAM	Reflective	Single

3.2.3 Wireless network measurements

The wireless network experiments were undertaken using the *MICAz* [75] WSN development package which uses the 802.15.4 physical layer communications protocol, operating on the defined channels in the 2.4 GHz Industrial Scientific and Medical (ISM) band. The channel was measured using the Received Signal Strength Indicator (RSSI), and the MICAz motes were integrated into a WSN unit. This unit was developed specifically for the measurements presented in this dissertation. To ensure that units interfered with the normal use of the vehicle as little as possible, it was specified that they should be small, unobtrusive, robust and have a low-profile, moreover these properties are expected to be broadly representative of actual in-vehicle WSN nodes to be deployed in future systems. To achieve useful propagation measurements, it was also required that the units be fitted with high (known) efficiency omnidirectional antennas, and that the RSSI values should be calibrated such that the actual channel response could be estimated.

Three units were built, of which one is shown in Fig. 3.7. It consists of a plastic box housing a MICAz mote, linked via a half-wavelength coaxial cable to a low-profile patch-type antenna with an omnidirectional radiation pattern (previously introduced in Section 3.2.1), and has dimensions 120 mm $\times$ 64 mm $\times$ 40 mm (excluding the antenna). The antennas operate in the 2.4 GHz ISM bandwidth and the efficiency of each antenna was measured, as detailed in Appendix A.

Each unit could act as either a transmitter or a receiver, and calibration was undertaken for each pair of units, and for each of the 16 possible frequency channels. The two units were connected via a known attenuation (comprising of a co-axial cable, and a variable attenuator) which was varied with step size of 1 dB. For each attenuation setting, the RSSI value was recorded. On occasion two or more attenuation values resulted in the same RSSI value being measured, and in such instances the attenuation was averaged to ensure that the registered RSSI could be converted to the corresponding channel response with a one-to-one function. Details of the calibration are given in Appendix B.

In the measurement campaign, one of the units (unit 2) was set to constantly transmit at 8 packets per second on the 2.45 GHz channel whilst the other two (units 1 and 3) acted as receivers. In all cases the measurements were undertaken with the car being driven. The measurement campaign is summarised in Table 3.3

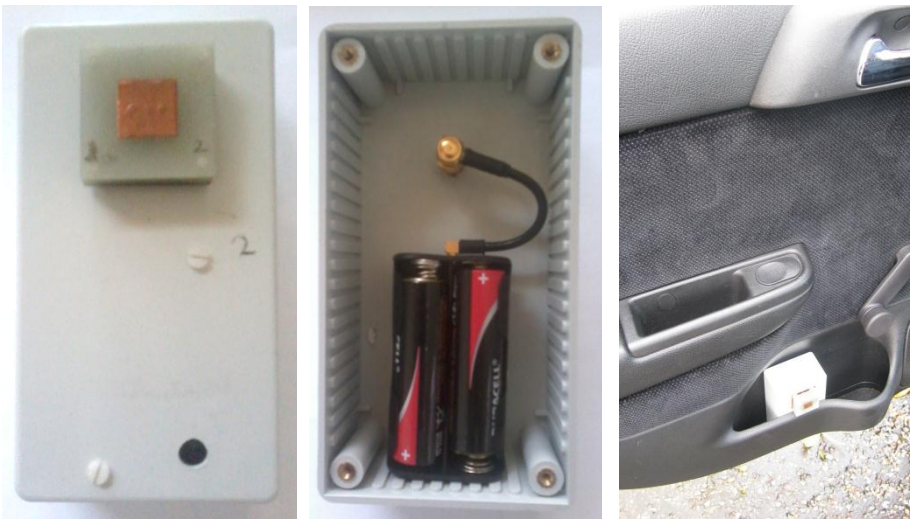

(a) (b) (c)

Figure 3.7: WSN unit: (a) top view; (b) inside view; (c) deployed at $P_{Car\,3}$

Table 3.3: Wireless network measurements.

Campaign	**Environment**	**Loading**	**Unit location**
3	Car	1 occupant	Tx: $P_{Car\,3}$, Rx1: $P_{Car\,1}$, Rx2: $P_{Car\,4}$

3.3 Propagation simulation

An EM wave propagation simulation has been undertaken primarily to find the angular spread of the arriving energy. A secondary purpose of the simulation is to find the variation in total arriving energy with spatial separation. For simplicity, the propagation simulation was only performed for the vehicle-like cavity, as the regular geometry of this environment greatly simplified the simulator.

The simulator was written in *MATLAB* [76], and the programme allowed the transmitter and receiver to be located at any point in the cavity. Both transmitter and receiver were modelled as having isotropic radiation patterns, and the receiver was deemed to have received a ray if it passed within a circle centred on the receiver location, with area equal to the effective aperture of an isotropic antenna with 100 % efficiency. The frequency was set to 1.7 GHz, as analysis on the measurements showed this to be the Lowest Usable Frequency of the cavity, and thus Friis transmission equation [77] was used to find the diameter of the circle (56.2 mm) which constituted the receiver in the simulation.

The simulator was written such that a sphere around the transmitter was divided up in sections using equally spaced polar co-ordinates. Each section of the sphere was assumed to have power proportional to its area, and was modelled as a single ray, whose propagation was traced using geometry. The rays were propagated for a maximum period of 120 ns, and the step size of the polar angles was chosen such that after 120 ns the area of the largest ray was approximately equal to the area of the receiver (i.e., because the area which each ray covers increases with time). As the transmit power has been divided up over the sphere's surface area (see Fig. 1.3 for illustration), this is consistent with an incoherent isotropic point source model, and thus it is not possible to infer directly the impulse response of a input signal.

The power reflection co-efficient (i.e., for reflections off the cavity boundaries, and stirrer) was set to 0.97, to match the time constant of the simulation to that of the actual cavity. Whilst 0.97 is low for a perfect aluminium reflection, taking into account the corroded surfaces, imperfect sealing of adjacent panels, reflections off the stirrer (which is imperfect) and the slightly more complex cavity geometry (i.e., lips around the windows), this does not seem unreasonable. To further enhance the simulation, a simplified stirrer was introduced, this consisted of a single plane with corners at:

- (800, 390, 325) mm,
- (800, 750, 325) mm,
- (440, 390, 735) mm,
- (440, 750, 735) mm,

which is approximately the size and location of the actual stirrer, just with a much simplified geometry. For all the simulations performed, the stirrer (when present) blocked the LOS path between the transmitter and the receiver.

The propagation simulation was run for a single transmitter location, and multiple receiver locations. Table 3.4 summarises the simulations that were run, and whilst the propagation simulator remained the same for each run, it served two distinct purposes. In Simulation 4.1, the angular spread at a point was recorded, whereas in Simulation 4.2, the total arriving energy at various locations in space was recorded. In both simulations it was convenient to treat the transmission as an impulsive input with total energy 1 J.

Table 3.4: Propagation simulation.

Simulation	Frequency / GHz	Tx location / mm	Rx location / mm
4.1	1.7	(1000, 880, 510)	(300, 490, 440), (256, 210, 810), (300, 470, 440)
4.2	1.7	(1000, 880, 510)	x = 300 y = (412.6: 56.2: 637.4) z = (327.6: 56.2: 552.4)

For Simulation 4.2, Rx was located at each point on a 5 × 5 grid, where y and z are denoted (initial location: step: final location). The step is chosen such that the apertures just touch for adjacent receivers.

3.4 Chapter summary

This dissertation uses experimental data to support the proposed theory, and to demonstrate the capability of actual in-vehicle wireless communication system. This experimental data is gathered from measurements performed in actual road vehicles, and an EM cavity with vehicle-like features placed in an anechoic chamber.

Three types of measurements have been undertaken:

- SP measurements to infer the channel impulse response, investigate the EF distribution and investigate whether the vehicle cavity can be treated as an isolated environment. The SP measurements are also used in place of wireless network measurements, as for some of the analysis it is required that the complex channel response is available (and the wireless network measurements only provide the magnitude of the channel response).
- Spectrum measurements to investigate typical in-vehicle Doppler spreads.
- Wireless network measurements to demonstrate how the theory can improve the performance of an actual in-vehicle wireless communication system.

Also, a propagation simulation has been undertaken for the vehicle-like cavity, to aid the understanding of the angular spread, and the total arriving energy.

Chapter 4

A propagation model for the in-vehicle channel

As identified in Chapter 1, the time varying impulse response, $h_{\mathbb{H}}(t, \tau)$ completely defines the action of a wireless channel. It is, however, difficult to find a general statistical expression for $h_{\mathbb{H}}(t, \tau)$. This is because the range of possible changes affecting the propagation is vast, and any full characterisation would be extremely complicated.

Instead a more fruitful approach is to characterise the instantaneous impulse response (which can also be thought of as the impulse response of a time invariant channel), and the Doppler spread at a given frequency. The instantaneous impulse response can be used to find the channel delay spread, (and thus also the coherence bandwidth) and the Doppler spread can be used to find the coherence time. Knowledge of these parameters is crucial for the effective deployment of in-vehicle wireless communication systems and for evaluating the channel information capacity.

Specifically, in Section 4.1 the channel response to an impulse input of energy is investigated; and in Section 4.2 the Doppler spread is characterised in terms of its Power Spectral Density (PSD).

4.1 Impulse response of the in-vehicle channel

The instantaneous impulse response is modelled as a random process. As explained in Chapter 1, this is a justifiable approach, as it is unlikely that there will be precise information concerning the instantaneous geometry and material properties of all objects in the cavity, however it may be possible to parameterise the process in a more general way using a statistical method.

A statistical model is therefore derived for two situations:

I. A perfectly incoherent isotropic source, where all the energy arriving at a certain point is considered to be received, however it cannot meaningfully be expressed as a signal.

II. A perfectly coherent isotropic source, where all the energy arriving at a certain point is considered to be received as a signal.

The theoretical model is expressed in the form of a series of arriving rays (i.e., a ray is an infinitesimally narrow cone of the transmitted signal) of , as the response to an impulse input of energy. The term 'signal' denotes a quantity proportional to the square root of the power (given a constant impedance), and in general could be an electric field or a magnetic field when propagating as a wave, or a voltage or a current when in a circuit. As the model is a propagation model, it does not account for the effects of transmit and receive antenna radiation patterns. It is, however, demonstrated that for the coherent case, a reasonable agreement is found between the theory and measurements using omnidirectional antennas.

4.1.1 Assumptions

Assumption 1: All rays arrive independently.

Assumption 2: All rays are attenuated independently.

These assumptions arise because in general there need not be any underlying structure to the impulse response, i.e., caused by distinct clusters of arriving rays. Even where a clustered structure has been observed, such as by Sawada *et al* [34], in general in such a confined propagation environment two or more clusters may overlap to such an extent that they become indistinguishable. Together, these two assumptions are consistent with the Uncorrelated Scattering (US) assumption which is commonly used to model channels, as discussed in Chapter 2.

Moreover these assumptions are valid in the sense that they entirely model that which is currently known about the channel (i.e., the most general case). It may, however, prove to be the case that preliminary measurements show that the impulse response consistently has a clustered structure which could be exploited to improve the model.

Justification

Measurement Campaign 1.1 is used to justify these assumptions. The scattering parameters (SPs) acquired from the frequency sweep are used to approximate the impulse response by using the following process[1]:

I. The receive antenna collects energy over an aperture with area that is inversely proportional to the frequency of operation squared. The frequency sweep is therefore normalised by multiplying S_{21} by the frequency (i.e., as SPs have the same dimensions as the square root of power). This normalisation step is required as the desired impulse response is for the energy flux through a small, constant area. The analysis method is essentially the reverse of Friis transmission equation [77].

II. An inverse discrete Fourier transform (IDFT) is performed on the normalised S_{21} measurements.

III. A subjective judgement is made regarding the point at which the impulse response becomes indistinguishable from the noise floor, and the impulse response is truncated accordingly.

IV. A subjective judgement is made regarding a suitable threshold above which the received power is taken to be the result of received impulses, and all values below this are set to zero, leading to a discretised form of the impulse response.

V. All values at times before τ_0, i.e., the time of flight of a ray travelling along the Line-of-Sight (LOS) are set to zero ($\tau_0 = 3.52 \times 10^{-9}$ s for Measurement Campaign 1.1).

VI. The absolute value of the response at each time instant is squared to get the response to an impulse of energy.

VII. The total energy received is set to unity to normalise the results.

[1]This method is somewhat limited as it uses only a single frequency sweep measurement of the channel SPs. Although multiple measurements were taken, the channel was not sufficiently stable for these to be treated as identical realisations of the channel with independent additive noise. Specifically, this limits the potential to statistically analyse the results, however this is partially mitigated by the fact that the measurement environment (anechoic chamber) has a very low noise floor.

The two configurations measured in Measurement Campaign 1.1 (i.e., which differ because the Port 2 antenna has been rotated – full details available in Table 3.1) are named Measurement Campaign 1.1a and Measurement Campaign 1.1b. Figs. 4.1 and 4.2 show the approximate impulse responses for 1.1a and 1.1b respectively. There is no apparent clustered structure, however as to be shown in Section 4.1.4, these approximate impulse responses do exhibit properties which are consistent with the Assumptions 1 and 2.

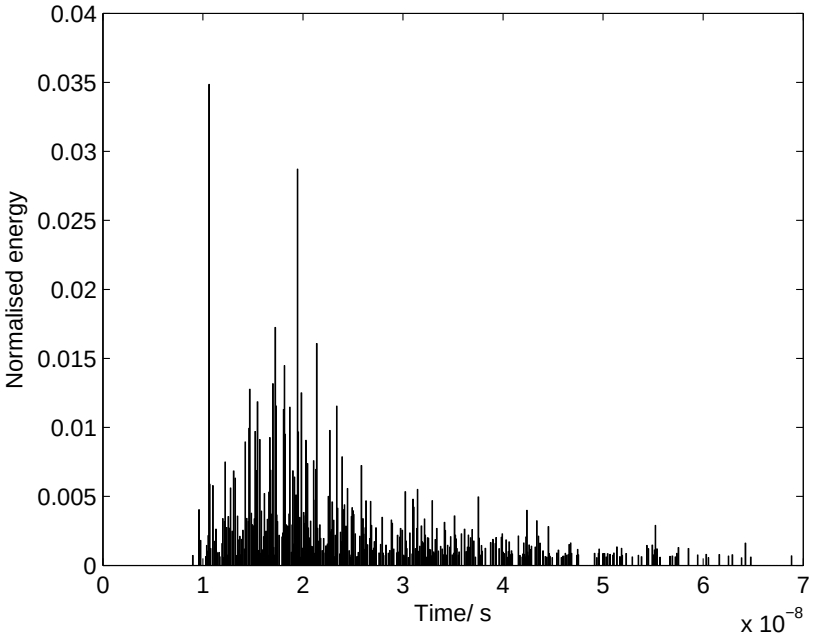

Figure 4.1: Impulse response of Measurement Campaign 1.1a

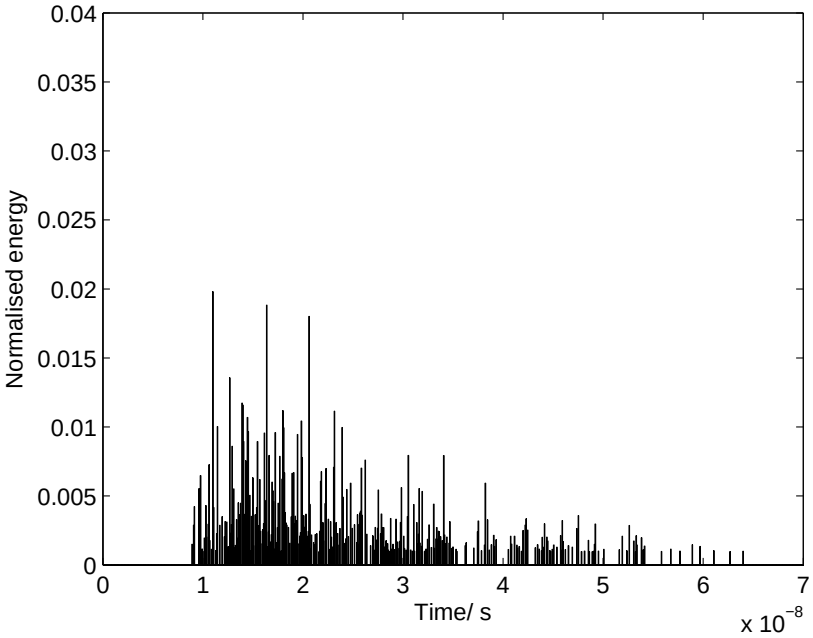

Figure 4.2: Impulse response of Measurement Campaign 1.1b

4.1.2 Theory for a perfectly incoherent isotropic point source transmitter

The theoretical impulse response model can be split into a random process to model the ray arrivals, and a random process to model the energy of a ray arriving at a given time delay. As it is the energy of the ray which is modelled, it is convenient to express the results in the form of the Power Delay Profile (PDP). Initially the impulse response of a perfectly incoherent isotropic point source is modelled. The incoherent source model cannot be used to find an impulse response in terms of signal (it is only valid in terms of power), however it is a useful starting point upon which the coherent source model will be based.

The PDP, $\mathrm{P}_{\mathbb{H}}(t_0, \tau)$ (i.e., at time t_0), is derived in terms of a number of received rays, of which the i^{th} has energy $\mathrm{E}_{\text{ray}}(\tau)$ (which may in general be a random variable), and delay τ_i:

$$\mathrm{P}_{\mathbb{H}}(t_0, \tau) = \sum_{i=1}^{\infty} \mathrm{E}_{\text{ray}}(\tau)\delta(\tau - \tau_i), \tag{4.1}$$

where $\delta(.)$ is the *Dirac* delta function.

Ray arrival process

The Poisson process models the most general arrival process, where all rays arrive independently [78]. The number of arrivals, n, in a time interval $\Delta\tau$ is modelled as a Poisson distribution, with Probability Mass Function (PMF):

$$P(n) = \frac{(k_b \Delta\tau)^n e^{-k_b \Delta\tau}}{n!}, \tag{4.2}$$

with ray arrival rate, $k_b\,[s^{-1}]$, (typically λ would be used, however k_b is used here to avoid ambiguity with wavelength). Here and below the notation '[.]' is used to denote the units of the given parameter.

Strictly speaking (4.2) is the PMF of the *Homogenous* Poisson process, and is only valid if the parameter, k_b does not vary with time. This is not the case for the in-vehicle channel impulse response, and therefore (4.2) is only valid where the time interval, $\Delta\tau$, is sufficiently short such that k_b is approximately constant (i.e., because k_b varies continuously with time).

To find the variation of k_b with time, consider a cavity which is completely enclosed by a perfectly reflective boundary, and consists of a constant, lossless medium. Let $\Delta\tau$ be sufficiently

short such that k_b is approximately constant. The expected energy, $\mathbb{E}\left(\mathrm{E}(\Delta\tau)\right)$, arriving in this time interval can be expressed:

$$\begin{aligned}\mathbb{E}\left(\mathrm{E}(\Delta\tau)\right) &= \mathbb{E}\left(\int_{\tau}^{\tau+\Delta\tau} \mathrm{P}_{\mathbb{H}}(t_0,\tau)\,\mathrm{d}\tau\right) &(4.3)\\ &= \mathbb{E}(n) \times \mathrm{E}_{\text{ray}}(\tau)\\ &\propto k_b\Delta\tau \times \tau^{-2}, &(4.4)\end{aligned}$$

where $\mathrm{E}_{\text{ray}}(\tau)$ is the energy of a ray arriving at τ, which is deterministic and proportional to τ^{-2} as the propagation speed through the medium is constant. The expectation of a Poisson random variable is equal to its parameter, in this case $k_b\Delta\tau$. In a lossless medium, to obey the law of the conservation of energy, (4.4) must always be proportional to $\Delta\tau$ for all τ, therefore $k_b \propto \tau^2$, and can be expressed in terms of the parameter k_{b0} [s^{-3}]:

$$k_b = k_{b0}\tau^2. \tag{4.5}$$

Allowing for a variable medium:

Consider a (theoretical) medium which is lossless, but has regions with varying propagation velocity. The assumption that the ray arrivals form a Poisson process is still valid. It is no longer the case that energy of a ray at time τ is proportional to τ^{-2}, in general only the expected energy of the ray $\mathbb{E}\left(\mathrm{E}_{\text{ray}}(\tau)\right)$ is proportional to τ^{-2}. Re-expressing (4.3) for the more general case where E_{ray} is a random variable:

$$\begin{aligned}\mathbb{E}\left(\mathrm{E}(\Delta\tau)\right) &= \mathbb{E}\left(\int_{\tau}^{\tau+\Delta\tau} \mathrm{P}_{\mathbb{H}}(t_0,\tau)\,\mathrm{d}\tau\right)\\ &= \sum_{n=0}^{\infty} nP(n)\mathbb{E}\left(\mathrm{E}_{\text{ray}}(\tau)\right)\\ &= \sum_{n=0}^{\infty} n\frac{(k_b\Delta\tau)^n\left(1+(-k_b\Delta\tau)+\frac{(-k_b\Delta\tau)^2}{2!}+\frac{(-k_b\Delta\tau)^3}{3!}+\ldots\right)}{n!}\mathbb{E}\left(\mathrm{E}_{\text{ray}}(\tau)\right) &(4.6)\end{aligned}$$

let $\Delta\tau \to 0$:

$$\begin{aligned}\mathbb{E}\left(\mathrm{E}(\Delta\tau)\right) &= k_b\Delta\tau \times \mathbb{E}\left(\mathrm{E}_{\text{ray}}(\tau)\right) &(4.7)\\ &\propto k_b\Delta\tau \times \tau^{-2}, &(4.8)\end{aligned}$$

therefore $k_b = k_{b0}\tau^2$ remains valid. In simple terms the random arrival process can be said to have absorbed the randomness of the time of flight, which means that the arrival process model generalises to the case where the rays propagate through a non-uniform medium.

Adjusting the arrival process for a cavity with apertures:

Consider a cavity with apertures. Now suppose that these apertures are enclosed by an arbitrary surface to form a completely closed boundary. The impulse response arrival process of this cavity (i.e., with the apertures closed) can be modelled as described previously, however when the apertures are re-introduced some of the rays will be lost to the outside world. A single ray undergoing a single reflection is modelled as a Bernoulli process, i.e., the ray is lost with a certain probability (if the ray reflected off a part of the boundary which was actually an aperture). Let $e^{-k'_e}$ be the probability that a ray is not lost, and let a given ray undergo m reflections with the cavity boundaries. Each reflection with a cavity boundary is assumed to be an Independent and Identically Distributed (IID) Bernoulli random process with a probability $e^{-k''_e}$ of not being lost. Therefore for a ray still to exist when the apertures are reintroduced, all reflections must still exist, hence:

$$\begin{aligned} e^{-k'_e} &= \prod_{i=1}^{m} e^{-k''_e} \\ &= e^{-mk''_e}. \end{aligned} \tag{4.9}$$

The number of reflections will be a random variable with the mean scaled by the time of flight, therefore defining parameter k_e [s^{-1}]:

$$e^{-k_e\tau} = e^{-mk''_e}. \tag{4.10}$$

Only $e^{-k_e\tau}$ of the rays are expected to remain when the apertures are re-introduced. Accordingly k_b must be scaled by $e^{-k_e\tau}$. Note that the Poisson arrival process is already a random process, so the parameter is scaled by the mean of the ray loss process, as the randomness will be absorbed by the Poisson process. The general form for the distribution of the number of arrivals, n, arriving in a short time interval, $\Delta\tau$, at a time lapse τ after an impulse can therefore be expressed as:

$$P(n) = \frac{(k_b\Delta\tau)^n e^{-k_b\Delta\tau}}{n!}, \tag{4.11}$$

$$k_b = k_{b0}\tau^2 e^{-k_e\tau}. \tag{4.12}$$

Ray attenuation process

Consider a ray to traverse a path which can be split into a large number, N, of short elements, consequently the ray's energy will be:

$$\mathrm{E}_{\text{incoh}}(\tau) \propto \prod_{i=1}^{N} \left(\frac{d_i}{d_{i-1}}\right)^{-2} e^{-z_i}, \tag{4.13}$$

where the subscript 'incoh' refers to the energy of a ray from a perfectly incoherent isotropic point source, d_i is distance to the end of the i^{th} element, and e^{-z_i} is attenuation. τ is related to d, as to be discussed. Note that ray power decay with distance can only be expressed in terms of ray power at some other distance, hence the distances are relative to a distance d_0, which is arbitrarily close to the source. An equivalent expression to (4.13) is:

$$\mathrm{E}_{\text{incoh}}(\tau) \propto \left(\frac{d_N}{d_0}\right)^{-2} e^{-\sum_{i=1}^{N} z_i}. \tag{4.14}$$

The N elements are assumed to be IID random variables. Whilst in reality this may not be correct, in the absence of a good model for how the elements are correlated, this is a sensible assumption to make since it will represent the most general case, moreover as the Central Limit Theorem (CLT) is subsequently to be applied this assumption should not matter so long as the ray passes through a sufficient number of independently attenuated regions of the cavity (including boundary reflections). Noting that the number of elements is proportional to the ray distance, the CLT is applied to the sum in (4.14) to yield:

$$\mathrm{E}_{\text{incoh}}(\tau) \propto \left(\frac{d_N}{d_0}\right)^{-2} e^{-Z'}, \tag{4.15}$$

$$Z' \sim \mathcal{N}(k'_c d_N, k'_d d_N), \tag{4.16}$$

where $\mathcal{N}(\text{mean}, \text{variance})$ is the Gaussian distribution, and k'_c and k'_d are parameters required for this intermediate step.

Expressing $\mathrm{E}_{\text{incoh}}(\tau)$ as a function of time of flight, rather than distance of flight is preferable, which can be achieved by making the assumption that τ is proportional to d_N. Strictly speaking this is only valid for propagation through a constant medium, which is not necessarily the case for all Electromagnetic (EM) cavities. For example in a vehicle cavity, even though the majority of the propagation is through air, there are short sections possibly through human tissue. In this case the relationship between time and distance is itself a random variable, however it is reasonable to neglect this effect since it is expected that the attenuation incurred owing to the change of medium (such as human tissue) will dominate over the small change in the ratio of time of flight to distance of flight. Moreover if a random variable were introduced to model the relationship between time and distance, this would not be independent of the attenuation process (since the same physical change of medium causes the attenuation and the change in ray propagation velocity), and it would significantly increase the complexity of the model to include the co-dependence of these two random processes.

Having justified that $\tau \propto d_N$ is a reasonable approximation, (4.15) and (4.16) can be re-

expressed as:

$$\mathrm{E}_{\text{incoh}}(\tau) = k_a \tau^{-2} e^{-Z}, \tag{4.17}$$

$$Z \sim \mathcal{N}(k_c \tau, k_d \tau), \tag{4.18}$$

where k_a [J s^2], k_c [s^{-1}] and k_d [s^{-1}] are parameters. The ray energy is therefore a lognormal random variable [79] with time varying parameters, and scaled by the inverse of the square of the time of flight.

4.1.3 Theory for a perfectly coherent isotropic point source transmitter

For a perfectly coherent isotropic point source, the ray arrival times will be identical to those of a perfectly incoherent isotropic point source, because this is solely a property of the cavity geometry. It is however necessary to reconsider a suitable representation of the ray power. For the coherent source, instead of dividing up the total power, it is necessary to divide up the total signal: Consider a sphere centred on the source, the signal of the energy propagating through part of the sphere is proportional to the area of that part of the sphere (for the incoherent source, it was implicitly assumed that the energy is proportional to the area). This can be justified by considering the situation where all the signal recombines (i.e., sums) in phase. In such an instance, to avoid violating the conservation of energy, it is necessary that, as the recombination takes the form of a sum of the signal, the original division must also be in terms of the signal.

The same reasoning which led to (4.17) and (4.18) can be applied again, noting that for the coherent source it is the signal, v, which is proportional to the cross-sectional area of each ray. By also noting that the attenuation of the signal of a ray is proportional to the square root of the attenuation of the power of a ray, this yields:

$$\begin{aligned} v_{\text{coh}}(\tau) &= k'_a \tau^{-2} e^{-\frac{Z}{2}}, \\ \implies \mathrm{E}_{\text{coh}}(\tau) &= k''_a \tau^{-4} e^{-Z}, \end{aligned} \tag{4.19}$$

where the subscript ‘coh’ refers the a perfectly coherent isotropic point source, and Z remains as defined in (4.18).

4.1.4 Experimental verification

The theoretical propagation model consists of a time varying Poisson process to model ray arrivals, detailed in (4.11) and (4.12), and a time varying lognormal distribution to model the ray attenuation, detailed in (4.18) and (4.19). The approximate impulse responses from Measurement Campaigns 1.1a and 1.1b, shown in Figs. 4.1 and 4.2, respectively, exhibit features which are consistent with the theoretical model. Furthermore, a compelling case for the validity of the theoretical model can be made by considering the total arriving energy.

Ray arrival process

Plotting the inter-arrival times of successive rays provides a simple way to verify the theoretical arrival process. The inter-arrival time between two successive rays for a Poisson process with parameter k_b will be an exponential random variable also with parameter k_b [78]. The mean inter-arrival time is k_b^{-1} and the variance is k_b^{-2}. Recalling from (4.12) that for the theoretical propagation process $k_b = k_{b0}\tau^2 e^{-k_e\tau}$, fitted functions for the mean inter-arrival time (k_b^{-1}) are shown in Figs. 4.3 and 4.4 along with the actual inter-arrival times of the rays in Measurement Campaigns 1.1a and 1.1b respectively. The fit appears to be a good one, and the variance of the inter-arrival time also appears to be greater when the mean is greater, as is to be expected.

In the time period approximately from 1.25×10^{-8} to 2.5×10^{-8} s, the energy appears to be arriving so rapidly that it is unlikely that individual rays have actually been resolved. This conjecture is supported by the much greater energy levels observed during this time interval of the impulse response shown previously in Figs. 4.1 and 4.2 .

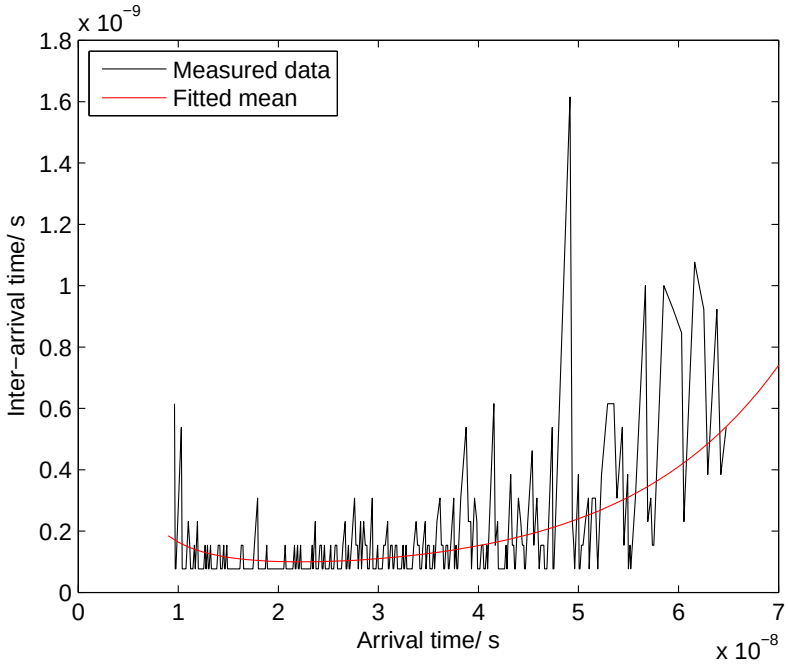

Figure 4.3: Arrival of rays in Measurement Campaign 1.1a

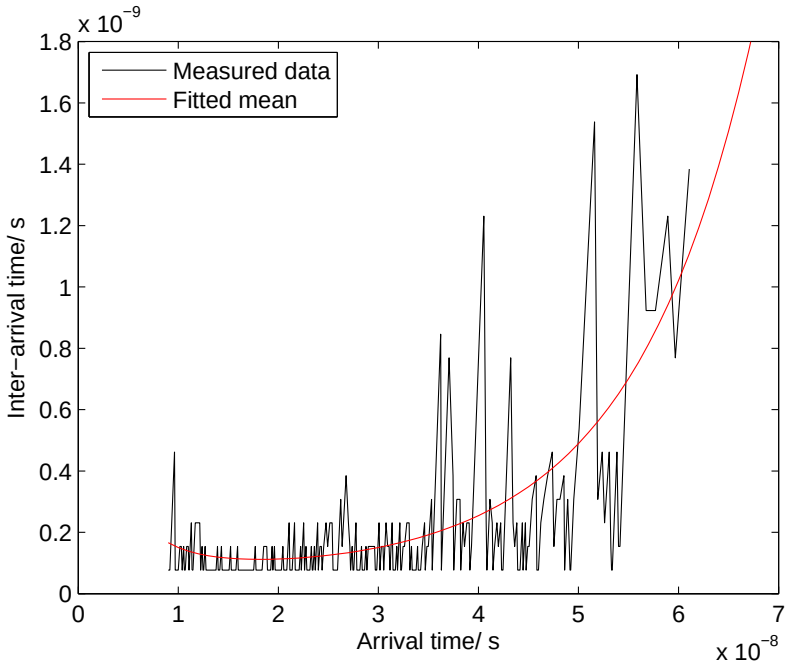

Figure 4.4: Arrival of rays in Measurement Campaign 1.1b

Ray attenuation process

Rays arriving around approximately 1×10^{-8} s are used to verify the attenuation process of the impulse response. This is because, as identified earlier in this section, it is likely that these are actually resolved impulses; and also because the arrival time is approximately constant, this simplifies the analysis since that the parameters of the attenuation process vary with time.

Recalling that, for the theoretical propagation model, the magnitudes of arriving rays should be lognormal random variables, the magnitudes of the arriving rays, along with lognormal fitted Cumulative Density Functions (CDFs) are shown in Figs. 4.5 and 4.6 for Measurement Campaign 1.1a and 1.1b respectively. The fit appears to be very good for both campaigns.

This verification, whilst appearing to be good, is somewhat limited in its scope: firstly it includes only a small number of resolved rays (33 and 35 for Measurement Campaigns 1.1a and 1.1b respectively), and secondly it provides no experimental verification that the theoretical model for the time variation of the lognormal parameters is valid.

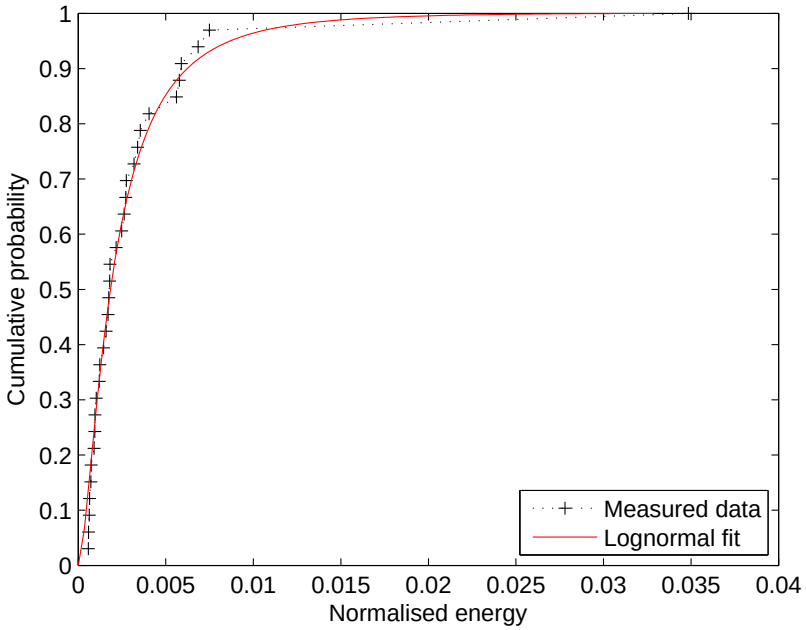

Figure 4.5: Attenuation of rays in Measurement Campaign 1.1a

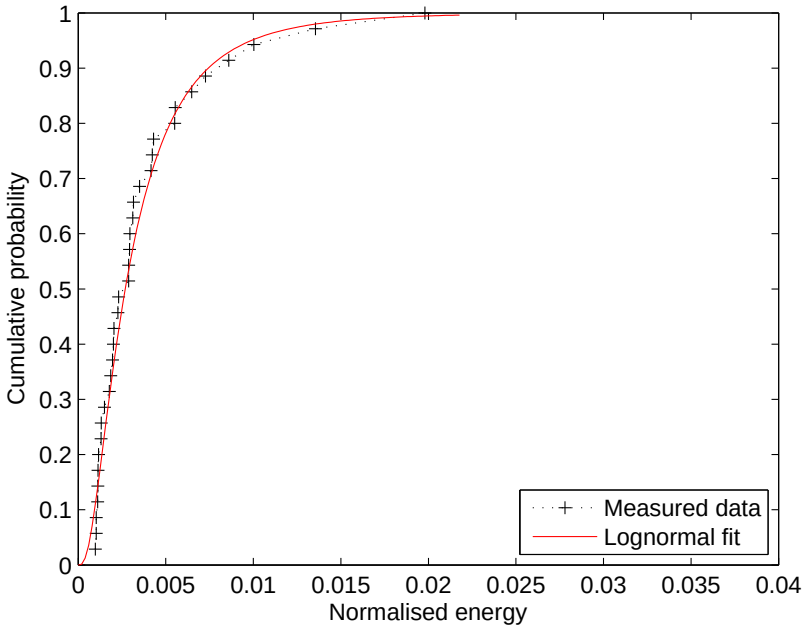

Figure 4.6: Attenuation of rays in Measurement Campaign 1.1b

Arriving energy

The total arriving energy can also be used as experimental evidence to support the theoretical results. Recall that the analysis leading to (4.7) is valid for both the incoherent and coherent sources, and that (4.12) provides an expression for k_b which is valid for both the incoherent and coherent sources. Substituting (4.12) into (4.7) yields:

$$\mathbb{E}\left(\mathrm{E}(\Delta\tau)\right) = k_{b0}\tau^2 e^{-k_e\tau}\Delta\tau \times \mathbb{E}\left(\mathrm{E}_{\text{ray}}(\tau)\right), \tag{4.20}$$

which can be related to the expected PDP:

$$\begin{aligned}\mathbb{E}\left(\mathrm{P}_{\mathbb{H}}(t_0,\tau)\right) &= \lim_{\Delta\tau\to 0}\frac{\mathbb{E}\left(\mathrm{E}(\Delta\tau)\right)}{\Delta\tau}\\ &= k_{b0}\tau^2 e^{-k_e\tau}\mathbb{E}\left(\mathrm{E}_{\text{ray}}(\tau)\right).\end{aligned} \tag{4.21}$$

To find the expected PDP for an incoherent source, (4.17) is substituted into (4.21). Noting that the expectation of a lognormal random variable with mean of the exponent μ and variance of the exponent σ^2 is $e^{\mu+\sigma^2/2}$:

$$\begin{aligned}\mathbb{E}\left(\mathrm{P}_{\mathbb{H}\,\text{incoh}}(t_0,\tau)\right) &= k_{b0}\tau^2 e^{-k_e\tau} k_a \tau^{-2} e^{-(k_c-k_d/2)\tau}\\ &= k_a k_{b0} e^{-(k_c-k_d/2+k_e)\tau}\\ &= k_1 e^{-\frac{\tau}{\tau_c}},\end{aligned} \tag{4.22}$$

where, by definition, $k_1 = k_a k_{b0}$ and $\tau_c = 1/(k_c - k_d/2 + k_e)$.

Likewise, to find the expected PDP for a coherent source, (4.19) is substituted into (4.21):

$$\begin{aligned}\mathbb{E}\left(\mathrm{P}_{\mathbb{H}\,\text{coh}}(t_0,\tau)\right) &= k_{b0}\tau^2 e^{-k_e\tau} k_a'' \tau^{-4} e^{-(k_c-k_d/2)\tau}\\ &= k_a'' k_{b0}\tau^{-2} e^{-(k_c-k_d/2+k_e)\tau}\\ &= k_2\tau^{-2} e^{-\frac{\tau}{\tau_c}},\end{aligned} \tag{4.23}$$

where, by definition, $k_2 = k_a'' k_{b0}$.

The term τ^{-2} in the right-hand side of (4.23) appears because the longer the time lapse, the more divided the signal has become. Consider an element of the transmitted power, with signal v, which arrives as a single ray, the arriving power is v^2. For an identical region of transmitted power, which arrives later as two rays each having signal of, say, $v/2$ (for simplicity), the received power (when averaged across all frequencies, as an impulse response can be interpreted by considering Parseval's theorem of energy conservation) is $(v/2)^2 + (v/2)^2 = v^2/2$. This apparent reduction in received power occurs because the signal becomes increasingly incoherent. This, however, is only valid if the input is genuinely a perfect impulse; indeed for any finite

bandwidth, if the rays arrive sufficiently close together (in time) that they cannot be resolved, they will appear to have arrived coherently, and thus the τ^{-2} term will not be observed. As previously noted, this appears to be the case for the majority of the arriving rays in Measurement Campaign 1.1. This phenomenon also means that any fading model will only be valid over a (relatively) small bandwidth, as the number of resolved rays (and hence the total power which will appear to have been received) will vary with the frequency.

This allows (4.23) to be re-expressed for a narrow bandwidth (i.e., the period of the largest frequency is small compared to the ray arrival rate), by dispensing with the term τ^{-2}. Furthermore, the PSD is often interpreted as an average, rather than a specific realisation (and this definition is more useful for the remainder of the dissertation), and thus the expectation term on the left-hand side of (4.23) is also dropped to give:

$$\mathrm{P}_{\mathbb{H}}(t_0, \tau) = k e^{-\frac{\tau}{\tau_c}}, \tag{4.24}$$

where k is a constant.

Therefore the theoretical model predicts that the expected power in the link will decay exponentially with time delay. This property is well known for reverberation chambers [18, 80], and has also been previously observed for vehicle cavities [9, 19, 23–25]. The consistency between the theoretical propagation model, and the well accepted exponentially decaying PDP provides compelling evidence for the validity of the model, and in particular supports the theoretical time variation of the lognormal parameters, which has not previously been verified.

To verify that the arriving energy in Measurement Campaign 1.1 is also consistent with the exponentially decaying PDP, consider for $\tau \geq \tau_0$ the expected total arriving energy $\mathbb{E}\left(\mathrm{E}_{\mathbb{H}}(t_0, \tau)\right)$:

$$\begin{aligned} \mathbb{E}\left(\mathrm{E}_{\mathbb{H}}(t_0, \tau)\right) &= \int_{\tau_0}^{\tau} \mathrm{P}_{\mathbb{H}}(t_0, \tau)\, \mathrm{d}\tau \\ &= k\left(\tau_0 e^{-\frac{\tau_0}{\tau_c}} - \tau e^{-\frac{\tau}{\tau_c}}\right). \end{aligned} \tag{4.25}$$

Figs. 4.7 and 4.8 show the total arriving energy for Measurement Campaigns 1.1a and 1.1b respectively, and in each case a very good fit is observed between the measurements and the exponential fit, which was estimated according to (4.25). The MMSE fitted plots have time constants (τ_c) of 17.2 ns and 16.6 ns for Measurement Campaigns 1.1a and 1.1b, respectively.

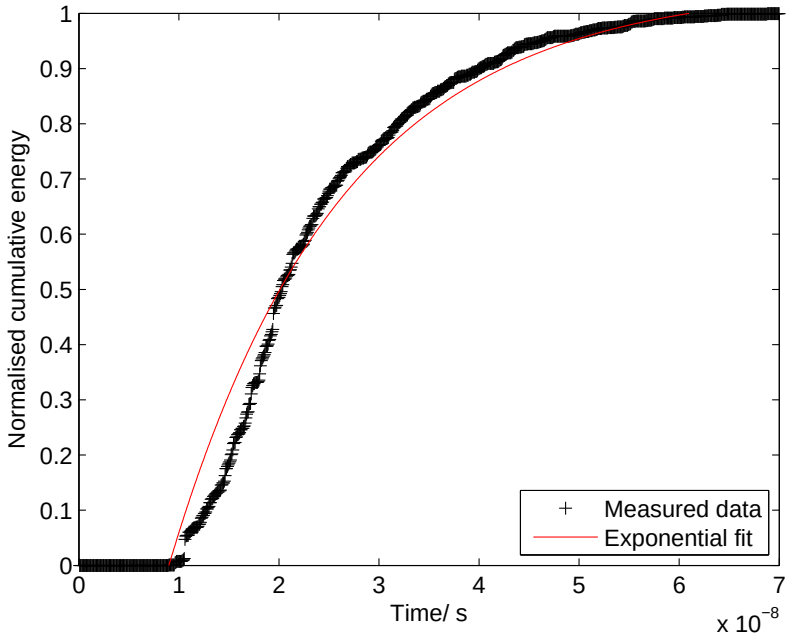

Figure 4.7: Cumulative arriving energy in Measurement Campaign 1.1a

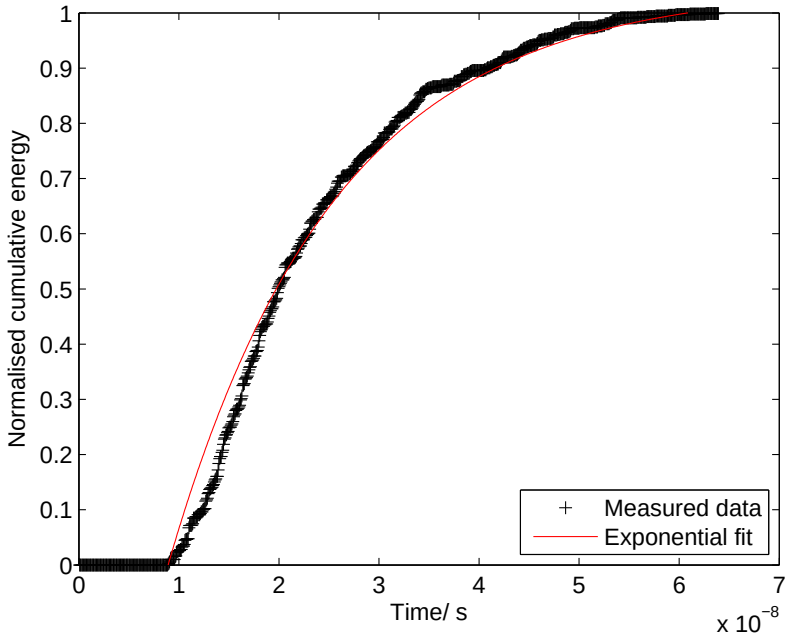

Figure 4.8: Cumulative arriving energy in Measurement Campaign 1.1b

4.2 Doppler spread of the in-vehicle channel

The Doppler spread of the in-vehicle channel is a direct result of the random motion of cavity occupants (or the random motion of the wireless devices, if they are mobile). This random motion is difficult to characterise, and neither is it trivial to derive the resulting Doppler spread in a chaotic environment such as an EM cavity. The Doppler spread characterisation to be presented in this chapter therefore takes a more general starting point, where four reasonable assumptions are made and subsequently used to upper bound the Doppler spread. This approach mitigates the risk of over-fitting the model to any particular pattern of channel variation caused by occupant motion.

It is more meaningful to derive the Doppler spread as an average, rather than for an instantaneous realisation, therefore the PSD is used to express the Doppler spread characterisation.

4.2.1 Assumptions

Assumption 3: At any given frequency, the channel is Wide-Sense Stationary (WSS).

Assumption 4: The Autocorrelation Function (ACF) at frequency f and time-shift ζ, $R_T(f;\zeta)$, is real and positive.

Assumption 5: $R_T(f;\zeta)$ decreases monotonically with $|\zeta|$, i.e., the channel becomes less correlated with time separation.

Assumption 6: The mean Doppler shift is zero.

Where the ACF of the time series of channel frequency responses, $z(f,t)$, is defined:

$$R_T(f;\zeta) = \mathbb{E}_t(z(f,t), z^*(f,t+\zeta)), \tag{4.26}$$

where * denotes complex conjugation. Note, that for a WSS process $R_T(f;\zeta) = R_T^*(f;-\zeta)$, therefore as the process is assumed to be real, $R_T(f;\zeta) = R_T(f;-\zeta)$.

Justification

Assumptions 3 – 6 can be justified primarily because they are physically reasonable. It is sensible to assume that the process is WSS, at least over short time scales. However, over longer time periods the statistics may change as various cavity occupants become more or less prone to move. Moreover it is usual to assume that reverberation chamber stirring is a WSS process [81–83], and as discussed in Chapter 2 there is precedent for treating vehicle cavities as

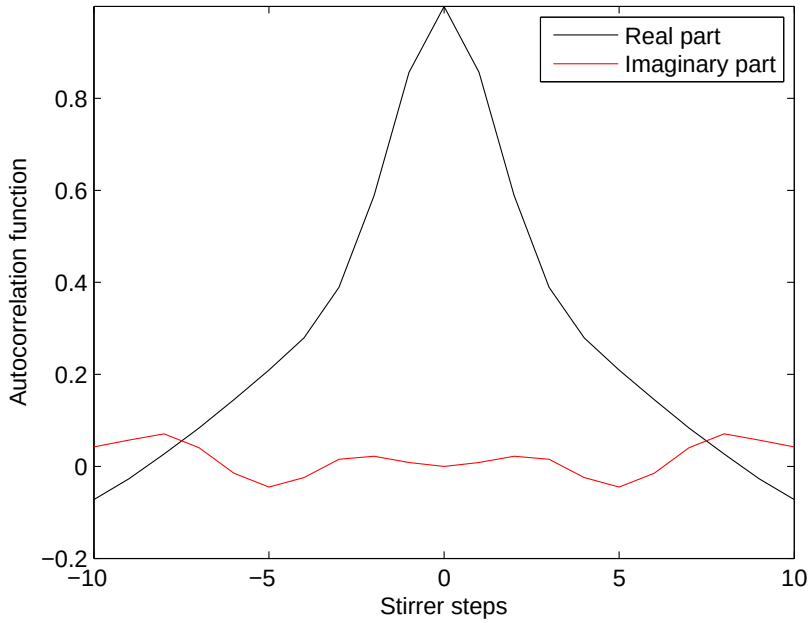

Figure 4.9: Autocorrelation function of the stirrer at 2.45 GHz

somewhat analogous to reverberation chambers. Assumptions 4 and 5 are consistent with a model where, after an arbitrary time interval, the received signal can be considered to be the sum of two components, the first being some fraction of that which was previously present (which is expected to decrease with time), and the second being that which has been disturbed, which is random and uncorrelated with the original signal. This model would appear to be reasonable, as the motion of the scatterers (or antennas) is jerky and unpredictable and involves motion with a range of speeds and directions. Situations where Assumptions 4 and 5 would not apply typically rely on constant motion of either the environment, or the antennas. Finally, Assumption 6 is made because there is no constant movement of either the transmit or receive antennas, or the environment. Given that the following analysis concerns only the statistical properties of the received signal, Assumption 6 is necessary in order to centre the analysis of the received signal around the frequency of the transmitted signal.

In addition to this qualitative discussion regarding Assumptions 3 – 6, some initial measurements that have been undertaken can also provide some evidence for their validity. Specifically Measurement Campaign 1.2, with the Port 1 antenna x-polarised; the cavity unloaded; and the stirrer on. Fig. 4.9 shows the ACF at 2.45 GHz for the forward voltage gain between Ports 1 and 3 (S_{13}), note that the stirrer was rotating at a constant rate, however 'stirrer steps' refers to the instantaneously measured values of S_{13}, recorded at regular time intervals. A full rotation consisted of approximately 100 stirrer steps. Fig. 4.9 supports Assumptions 4 and 5 that the ACF is predominantly real, positive and decreasing with the magnitude of time separation.

4.2.2 Theory

Given assumptions 3 – 6, three upper bounds exist on the PSD, $\mathrm{P}_H(f;\nu)$, at frequency shift ν.

Theorem 4.1:

There exists an upper bound, U_1 on the PSD:

$$\begin{aligned}\mathrm{U}_1 &= \mathrm{P}_H(f;0)\\ &\geq \mathrm{P}_H(f;\nu),\end{aligned} \tag{4.27}$$

with equality only at $\nu = 0$.

Proof:

Starting from the definition of $\mathrm{P}_H(f;\nu)$ from [[84] Equation (6.28)]:

$$\begin{aligned}\mathrm{P}_H(f;\nu) &= \int_{-\infty}^{\infty} R_T(f;\zeta)e^{-j2\pi\nu\zeta}\,\mathrm{d}\zeta\\ &= \int_{-\infty}^{\infty} R_T(f;\zeta)\cos(2\pi\nu\zeta)\,\mathrm{d}\zeta + j\int_{-\infty}^{\infty} R_T(f;\zeta)\sin(-2\pi\nu\zeta)\,\mathrm{d}\zeta\\ &= \int_{-\infty}^{\infty} R_T(f;\zeta)\cos(2\pi\nu\zeta)\,\mathrm{d}\zeta \qquad (4.28)\\ &\leq \int_{-\infty}^{\infty} R_T(f;\zeta)\times 1\,\mathrm{d}\zeta \qquad (4.29)\\ &= \mathrm{P}_H(f;0). \qquad (4.30)\end{aligned}$$

Note that (4.28) arises because $R_T(f;\zeta) = R_T(f;-\zeta)$, and the bound in (4.29) because $R_T(f;\zeta)$ is real and positive.

Theorem 4.2:

There exists an upper bound, U_2 on the PSD:

$$\begin{aligned}\mathrm{U}_2 &= \frac{1}{\pi\nu}\mathrm{P}_{\mathrm{Rx}}\\ &> \mathrm{P}_H(f;\nu),\end{aligned} \tag{4.31}$$

where P_{Rx} is received power.

Proof:

Starting from (4.28):

$$\begin{aligned}
\mathrm{P}_H(f;\nu) &= \int_{-\infty}^{\infty} R_T(f;\zeta)\cos(2\pi\nu\zeta)\,\mathrm{d}\zeta \\
&= 2\int_{0^+}^{\infty} R_T(f;\zeta)\cos(2\pi\nu\zeta)\,\mathrm{d}\zeta \\
&= 2\left[\frac{1}{2\pi\nu}\sin(2\pi\nu\zeta)R_T(f;\zeta)\right]_{\zeta=0^+}^{\infty} + 2\int_{0^+}^{\infty}\frac{-\mathrm{d}R_T(f;\zeta)}{\mathrm{d}\zeta}\,\frac{\sin(2\pi\nu\zeta)}{2\pi\nu}\,\mathrm{d}\zeta \\
&< 2\left[\frac{1}{2\pi\nu}\sin(2\pi\nu\zeta)R_T(f;\zeta)\right]_{\zeta=0^+}^{\infty} + 2\int_{0^+}^{\infty}\frac{-\mathrm{d}R_T(f;\zeta)}{\mathrm{d}\zeta}\,\frac{1}{2\pi\nu}\,\mathrm{d}\zeta \\
&< \frac{1}{\pi\nu}R_T(f;\infty) + \frac{1}{\pi\nu}\left(R_T(f;0^+) - R_T(f;\infty)\right) \qquad (4.32) \\
&= \frac{1}{\pi\nu}R_T(f;0) \\
&= \frac{1}{\pi\nu}\mathrm{P}_{\mathrm{Rx}}. \qquad (4.33)
\end{aligned}$$

The term 0^+ refers to a point infinitesimally to the right of the origin. The use of 0^+ is appropriate in this instance as the function $R_T(f;\zeta)$ is continuous and finite at $\zeta = 0$, however its derivative isn't necessarily continuous. The bound in (4.32) arises since throughout the region of interest (i.e., $\zeta > 0$), $R_T(f;\zeta) > 0$ and $\frac{-\mathrm{d}R_T(f;\zeta)}{\mathrm{d}\zeta} > 0$. These properties allow $\sin(2\pi\nu\zeta)$ to be replaced with 1 to find an upper bound on both the integral and the term inside the square brackets. Also, note that strictly speaking: $R_T(f;\infty) = \lim_{K\to\infty} R_T(f;K)$.

Corollary 4.3:

Using the property that $\mathrm{P}_{\mathrm{Tx}} \geq \mathrm{P}_{\mathrm{Tx}}$, where P_{Tx} is the transmitted power, there exists a further upper bound, $\mathrm{U}_{2\mathrm{A}}$, on the PSD:

$$\begin{aligned}
\mathrm{U}_{2\mathrm{A}} &= \frac{1}{\pi\nu}\mathrm{P}_{\mathrm{Tx}}, \\
&> \mathrm{P}_H(f;\nu). \qquad (4.34)
\end{aligned}$$

The results U_1, U_2 and $\mathrm{U}_{2\mathrm{A}}$ are of practical use as they provide a bound on the PSD if it is not measured (either at all or for some frequencies).

4.2.3 Experimental verification

Measurement Campaigns 2.1 and 2.2 are used to experimentally support the theory. These measurements were undertaken at 2.45 GHz, and concern four types of channel variation in the vehicle-like cavity:

- Absorptive stirring, i.e., a person moving and varying the channel.
- Reflective stirring, i.e., a reflective object moving and varying the channel.
- One antenna moving, i.e., a mobile to fixed channel.
- Two antennas moving, i.e., a mobile to mobile channel.

Also measured was the Doppler spread arising from a person sat in the van making movements typical of driving (albeit slightly exaggerated). Fig. 4.10 shows the input signal, and Fig. 4.11 shows the average received power to approximate the PSD, normalised such that for each plot the total received power equals one.

Fig. 4.12 shows a detailed view around the central frequency. U_1 is violated for one and two antennas moved – the maximum power is not at the central frequency, and U_2 is violated for one antenna moved, although all of these violations are small. Possible explanations for this are that the average over a small sample is not a perfect representation of the PSD, the antenna motion was not perfectly random (it is difficult in such measurements to achieve an actual typical motion pattern), and the constant wave source was not perfect (as shown in Fig. 4.10 it has non-zero bandwidth).

A more fundamental issue is that U_2 has been verified by a circular method. The total received power has been calculated assuming that there is not significant power received at Doppler shifts with magnitude greater than 50 Hz. Strictly U_2 is only valid if the total received power is known (or can itself be upper bounded) independently of the Doppler spread measurement, however for the purposes of measuring typical in-vehicle Doppler shifts these measurements are sufficient. An alternative would be to use U_{2A} however given the large attenuation due to path loss (typically of the order of 40 dB) this would require a PSD measurement over a very large bandwidth.

In general the Doppler spread is infinite, however at some shift the PSD will become negligible compared to the noise floor. Therefore this bounding method is most useful for relatively low Signal to Noise Ratio systems where the received power is known *a priori*. In such cases U_1 and U_2 can be used to significantly restrict the range of the measurement required to verify that the Doppler spread is acceptably small.

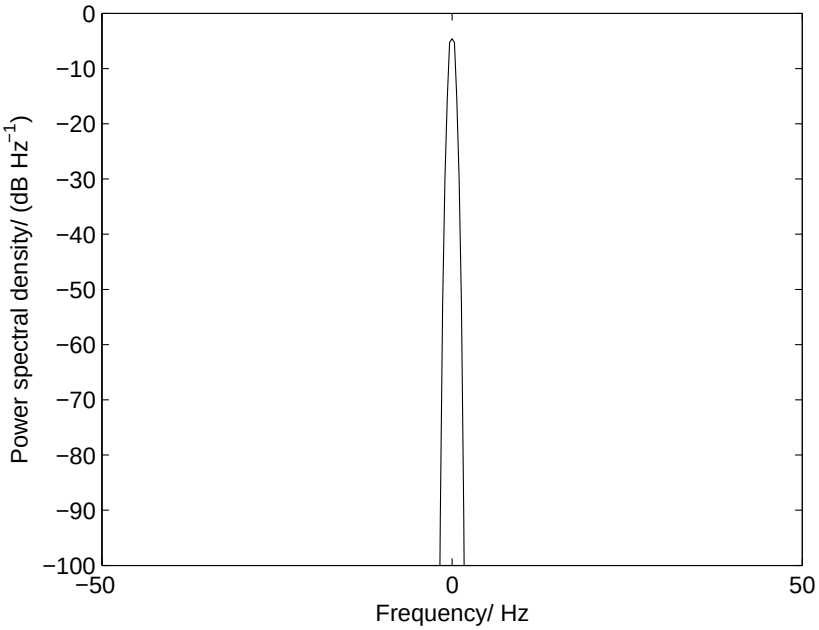

Figure 4.10: Normalised PSD of the input signal

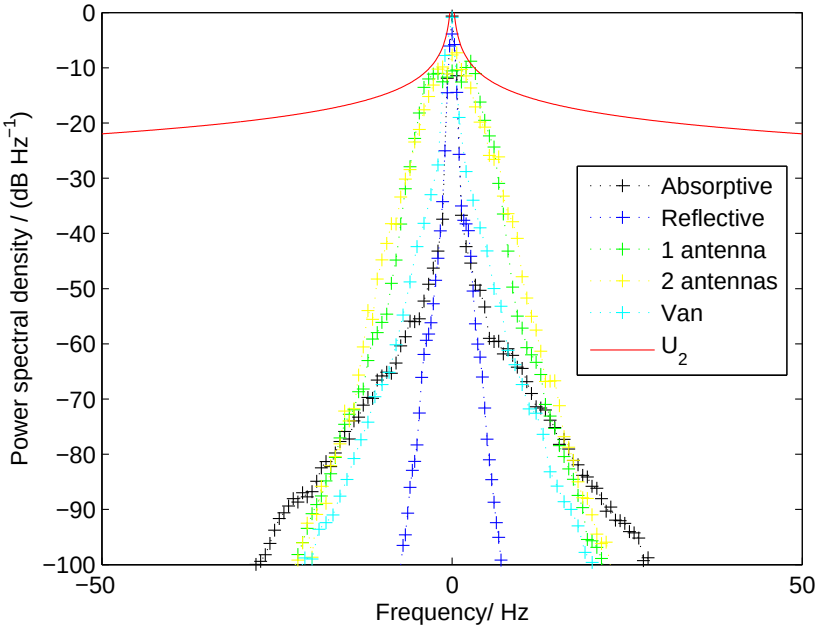

Figure 4.11: Normalised PSD of various stirring situations at 2.45 GHz

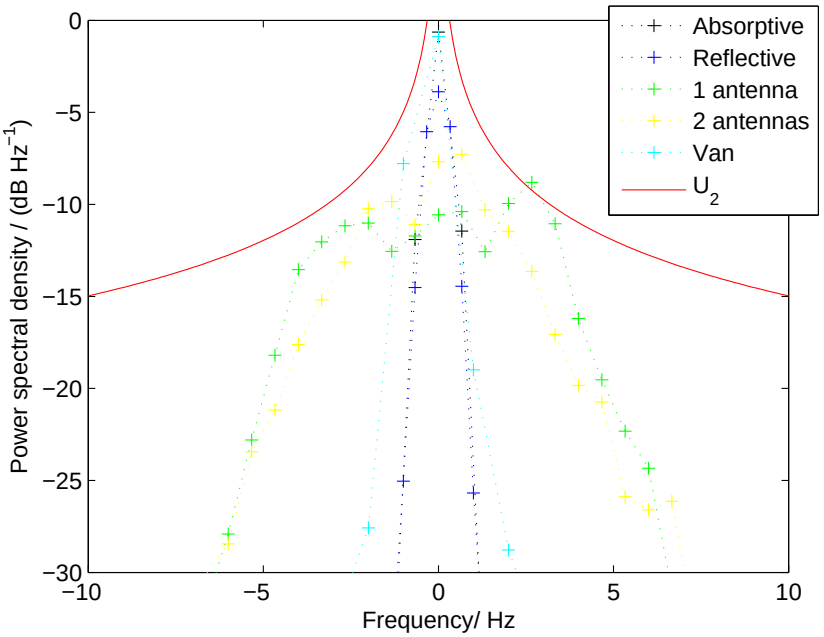

Figure 4.12: Normalised PSD of various stirring situations at 2.45 GHz (detailed)

4.2.4 Doppler spread variation with frequency and loading

To ensure a fair comparison between the Doppler spread with varying frequency and cavity loading, the stirrer is used at the same rotational speed (i.e., 0.19 revolutions per second). Due to their inherent variability antenna and human motion is not investigated. Details of the experimental method are given in Section 3.2.2, Measurement Campaign 2.3.

Fig. 4.13 shows that for a range of different transmission frequencies, there is a small decrease in Doppler spread as the cavity loading is increased. This is consistent with measurements performed by Chen *et al.* [39] in a reverberation chamber, although the effect in the vehicle cavity is significantly less pronounced. A possible explanation for this is because in the reverberation chamber, the high Q factor environment is altered significantly by the introduction of the Radiation Absorbent Material (RAM), and hence the mode density (and therefore Doppler spread) also varies. In the vehicle cavity, it is likely that the presence of the four windows dominate the effect of the RAM, and hence there is only a small change in the mode density with loading, and therefore the Doppler spread varies by a much smaller amount.

Fig. 4.13 does show that the Doppler spread increases with transmission frequency. To facilitate direct comparison Fig. 4.14 shows the Doppler spread for all of the measured transmission frequencies, with no cavity loading. The observed increase in the Doppler spread with frequency is consistent with previous work [38–40].

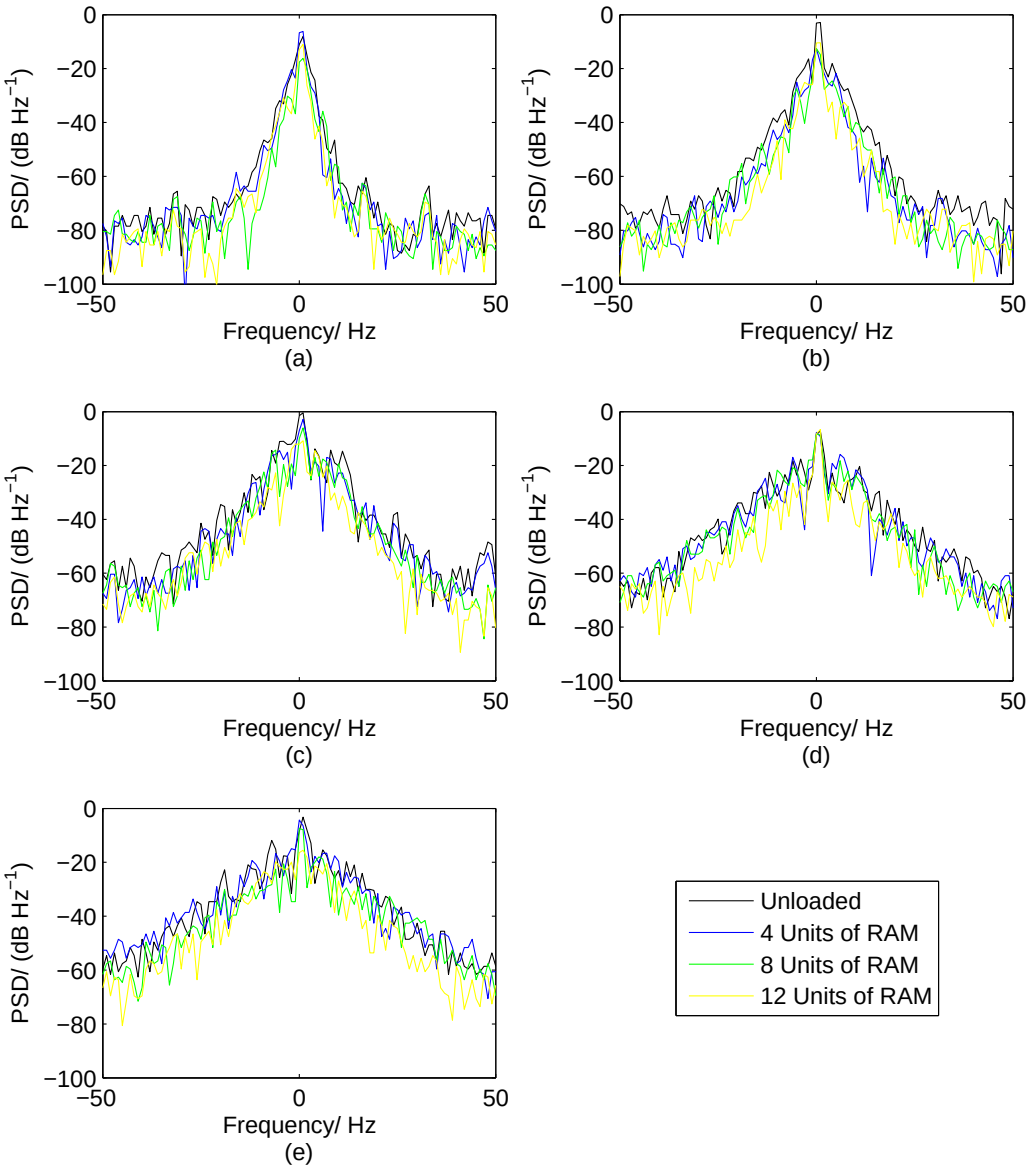

Figure 4.13: Normalised PSD with varying frequency and loading: (a) 3 GHz; (b) 6GHz; (c) 9 GHz; (d) 12 GHz; (e) 15 GHz

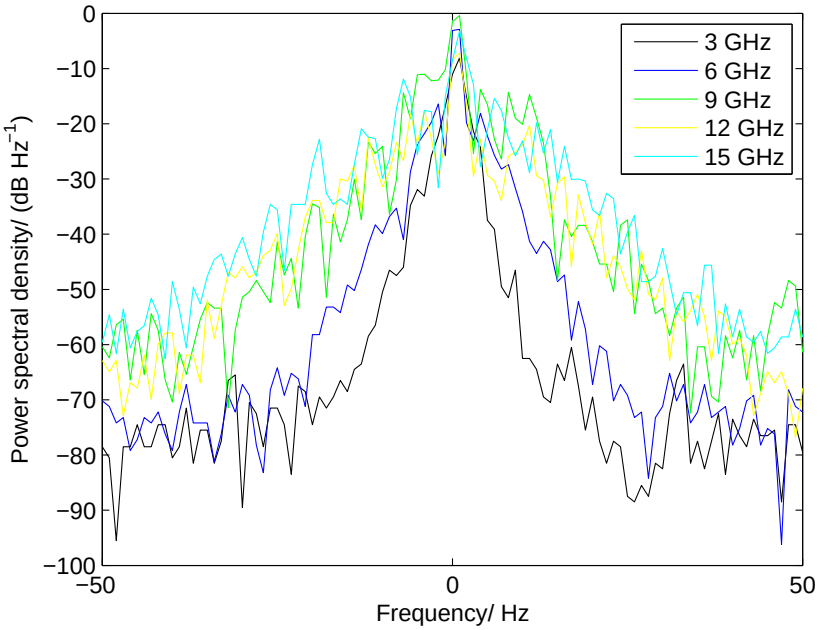

Figure 4.14: Normalised PSD with varying frequency (no cavity loading)

4.3 Chapter summary

A theoretical model for EM wave propagation in cavities has been derived. The propagation model is expressed in terms of a ray arrival process, and it has been derived from a general set of assumptions where each ray arrives independently, and each ray is attenuated independently. The ray arrival process is modelled as a Poisson process, with time varying parameters, and the ray attenuation is modelled as a random variable drawn from a lognormal distribution, with time varying parameters. A wideband frequency sweep performed in a vehicle-like cavity was used to approximate the impulse response (i.e., via an IDFT). There was found to be good agreement between the theoretical model, and the approximate impulse response, estimated from the measured data. Crucially, the theoretical model has the property that the PDP decays exponentially, which is well accepted for EM cavities including vehicle cavities.

The typical Doppler spread of in-vehicle channels has also been characterised. Given the inherent unpredictability of the occupant motion which leads to the Doppler spread, a very general set of assumptions was used to upper bound the Doppler spread. These assumptions are that the time variation of the channel is WSS, the channel autocorrelation function is real and monotonically non-increasing with time separation, and that the mean Doppler shift is zero. Spectrum measurements have been used to verify the validity of the upper bound for four types of channel variation: absorptive (human occupant) motion; reflective motion; a single antenna being moved; and both antennas being moved. Furthermore, Doppler spread measurements have been undertaken for a range of transmission frequency and loading scenarios, showing that the Doppler spread increases with frequency, but that variation in loading has little effect on the Doppler spread.

Chapter 5

A lower bound on the capacity of the in-vehicle channel

For any wireless channel, the information capacity is a crucial performance metric. The capacity for Additive White Gaussian Noise (AWGN) channels, with perfect receiver Channel State Information (CSI) is well known, as discussed in Chapter 2, however for real channels it is unrealistic to assume that CSI is available *a priori* at the receiver. Rather, the channel is assumed to be noncoherent, and thus any CSI will have to be learned at the receiver.

The characterisation undertaken in Chapter 4 reveals that the in-vehicle channel is typically highly underspread, i.e., the product of the delay spread (see Figs. 4.1 and 4.2) and the Doppler spread (see Figs. 4.11, 4.12, 4.13 and 4.14) is much smaller than one. In such situations, received wisdom states that, with sufficient bandwidth, the perfect receiver CSI capacity can be approached [49]. The purpose of this chapter is to demonstrate, using information theoretic analysis, that this is indeed the case.

5.1 Channel frequency response

As shown in Chapter 4, the instantaneous Power Delay Profile (PDP) of an in-vehicle channel decays exponentially:

$$\mathrm{P}_{\mathbb{H}}(\tau) = \begin{cases} 0 & \text{if } \tau < 0 \\ ke^{-\frac{\tau}{\tau_c}} & \text{if } \tau \geq 0 \end{cases} \tag{5.1}$$

where $\mathrm{P}_{\mathbb{H}}(\tau)$ is the PDP, k is a constant, τ time elapsed and τ_c is the cavity time constant. For the information theoretic analysis, a truncated version, $\mathrm{P}'_{\mathbb{H}}(\tau)$, of the PDP is required (τ_t is chosen such that the error between the truncated PDP and the original PDP is small, and this error will later be treated as additive noise):

$$\mathrm{P}'_{\mathbb{H}}(\tau) = \begin{cases} 0 & \text{if } \tau < 0 \text{ or } \tau > \tau_t \\ ke^{-\frac{\tau}{\tau_c}} & \text{otherwise.} \end{cases} \tag{5.2}$$

The bounding method requires information regarding the in-vehicle channel characterisation in the frequency domain. At a randomly chosen frequency, that is high compared to τ_c but low compared to the arrival rate of the rays (for the majority of the rays, i.e., so that the PDP in (5.1) is valid), the distribution of the phase of the various multipath components will be uniform, and thus the frequency response will be a Zero Mean Circularly Symmetric (ZMCS) Gaussian random variable; defining this as $z(\omega)$, let:

$$\underline{z}(\omega) \sim \mathcal{N}\left(\underline{z}(\omega); \underline{0}, \Sigma_z\right), \tag{5.3}$$

where $\mathcal{N}$ is the Gaussian distribution and ω is angular frequency (i.e., $\omega = 2\pi f$ where f is frequency) :

$$\Sigma_z = \begin{bmatrix} \sigma_z^2 & 0 \\ 0 & \sigma_z^2 \end{bmatrix}, \tag{5.4}$$

where σ_z^2 is the variance.

The bounding method also requires the conditional distribution of the frequency response, given the frequency response at a known separation, $(\Delta\omega)$, i.e., $P(z(\omega)|z(\omega - \Delta\omega))$.

Proposition 5.1

For the channel defined in (5.2), the conditional distribution of the frequency response, given the frequency response at a known separation can be expressed:

$$P(\underline{z}(\omega)|\underline{z}(\omega - \Delta\omega) = \underline{z}_{(\omega-\Delta\omega)}) = \mathcal{N}\left(\underline{z}(\omega); \underline{\mu}_a, \Sigma_a\right), \tag{5.5}$$

where:

$$\underline{\mu}_a = \underline{A}\underline{z}_{(\omega-\Delta\omega)}, \tag{5.6}$$

$$\Sigma_a = \sigma_z^2 \begin{bmatrix} 1-|a|^2 & 0 \\ 0 & 1-|a|^2 \end{bmatrix}, \tag{5.7}$$

and $\underline{z}_{(\omega-\Delta\omega)}$ is the realisation of $\underline{z}(\omega-\Delta\omega)$, $\underline{A}$ is the matrix version of the complex number a (i.e., according to the notation in (1.4)) and:

$$a = \frac{1}{1+j\Delta\omega\tau_c}\left(1-e^{-\tau_t((1/\tau_c)+j\Delta\omega)}\right)\left(1-e^{-\frac{\tau_t}{\tau}}\right)^{-1}. \tag{5.8}$$

Proof:

Consider splitting $\mathrm{P}'(\tau)$ into an integer number of time intervals each of duration $\Delta\tau$. Assuming that in each time interval there are many arriving rays, and that the frequency is sufficiently high such that the phase of each arriving ray can be considered to be a random variable drawn from a uniform distribution, then the resultant signal from each time interval is a ZMCS complex Gaussian random variable. Each of these will be independent, given the uncorrelated scattering assumption, which has already been demonstrated in Chapter 4 (i.e., Assumptions 1 and 2). The joint distribution of the signal from these intervals can thus be expresses as a multivariate complex Gaussian distribution: The discrete signal vector, $\mathbf{z}$, is of size K where $\mathrm{K} = \tau_t/\Delta\tau$ and the k^{th} element occurs at $\tau = \mathrm{k}\Delta\tau$ (k is used in non-italicised font to distinguish it from k in (5.1)):

$$\mathbf{z} \sim \mathcal{CN}(\mathbf{z}; \mathbf{0}, \Gamma, 0), \tag{5.9}$$

$$\begin{aligned}\Gamma &= \mathbb{E}\left(\mathbf{z}(\mathbf{z}^{*T})\right) \\ &= \mathrm{diag}(2\sigma_{\mathrm{k}}^2),\end{aligned} \tag{5.10}$$

where $\mathcal{CN}$ is the complex Gaussian distribution with covariance matrix Γ, * denotes the complex conjugate, ^{T} denotes the transpose (the operation $(.)^{*T}$ is sometimes referred to as the *Hermitian transpose*), and:

$$\sigma_{\mathrm{k}}^2 = \left(\mathrm{P}'_{\mathbb{H}}(\mathrm{k}\Delta\tau)\right)\Delta\tau. \tag{5.11}$$

By a Fourier transform, (5.9) can be used to approximate the frequency response at ω and $(\omega-\Delta\omega)$:

$$P\left(\begin{bmatrix} z(\omega) \\ z(\omega-\Delta\omega) \end{bmatrix}\right) \approx \lim_{\Delta\tau\to 0} \mathcal{CN}\left(\begin{bmatrix} z(\omega) \\ z(\omega-\Delta\omega) \end{bmatrix}; \mathbf{0}, \begin{bmatrix} \boldsymbol{f} \\ \boldsymbol{g} \end{bmatrix} \Gamma \begin{bmatrix} \boldsymbol{f} \\ \boldsymbol{g} \end{bmatrix}^{*T}, 0\right) \tag{5.12}$$

where $\boldsymbol{f}$ and $\boldsymbol{g}$ are row vectors, each of size K, with k^{th} elements:

$$f_{\mathrm{k}} = e^{-j\omega\mathrm{k}\Delta\tau}, \tag{5.13}$$

$$g_{\mathrm{k}} = e^{-j(\omega-\Delta\omega)\mathrm{k}\Delta\tau}. \tag{5.14}$$

Let:

$$\begin{bmatrix} \boldsymbol{f} \\ \boldsymbol{g} \end{bmatrix} \Gamma \begin{bmatrix} \boldsymbol{f} \\ \boldsymbol{g} \end{bmatrix}^{*T} = \begin{bmatrix} \gamma_1 & \gamma_2 \\ \gamma_3 & \gamma_4 \end{bmatrix}, \tag{5.15}$$

then, noting that $\tau = \mathrm{k}\Delta\tau$:

$$\gamma_1 = \sum_{\mathrm{k}=0}^{\mathrm{K}-1} e^{-j\omega\tau} \left(2\mathrm{P}'_{\mathbb{H}}(\tau)\Delta\tau\right) e^{j\omega\tau}, \tag{5.16}$$

$$\gamma_2 = \sum_{\mathrm{k}=0}^{\mathrm{K}-1} e^{-j\omega\tau} \left(2\mathrm{P}'_{\mathbb{H}}(\tau)\Delta\tau\right) e^{j(\omega-\Delta\omega)\tau}, \tag{5.17}$$

$$\gamma_3 = \sum_{\mathrm{k}=0}^{\mathrm{K}-1} e^{-j(\omega-\Delta\omega)\tau} \left(2\mathrm{P}'_{\mathbb{H}}(\tau)\Delta\tau\right) e^{j\omega\tau}, \tag{5.18}$$

$$\gamma_4 = \sum_{\mathrm{k}=0}^{\mathrm{K}-1} e^{-j(\omega-\Delta\omega)\tau} \left(2\mathrm{P}'_{\mathbb{H}}(\tau)\Delta\tau\right) e^{-j(\omega-\Delta\omega)\tau}. \tag{5.19}$$

Let: $\Delta\tau \to 0$ (and thus adjusting K such that τ_t does not vary):

$$\begin{aligned} \gamma_1 = \gamma_4 &= \int_0^{\infty} 2\mathrm{P}'_{\mathbb{H}}(\tau)\,\mathrm{d}\tau \\ &= 2k\tau_c \left(1 - e^{-\frac{\tau_t}{\tau_c}}\right), \end{aligned} \tag{5.20}$$

$$\begin{aligned} \gamma_2 &= \int_0^{\infty} 2\mathrm{P}'_{\mathbb{H}}(\tau) e^{-j\tau\Delta\omega}\,\mathrm{d}\tau \\ &= \frac{2k\tau_c}{1 + j\Delta\omega\tau_c} \left(1 - e^{-\tau_t(1/\tau_c + j\Delta\omega)}\right), \end{aligned} \tag{5.21}$$

$$\begin{aligned} \gamma_3 &= \int_0^{\infty} 2\mathrm{P}'_{\mathbb{H}}(\tau) e^{j\tau\Delta\omega}\,\mathrm{d}\tau \\ &= \frac{2k\tau_c}{1 - j\Delta\omega\tau_c} \left(1 - e^{-\tau_t(1/\tau_c - j\Delta\omega)}\right). \end{aligned} \tag{5.22}$$

Noticing that $[z(\omega); z(\omega - \Delta\omega)]$ is ZMCS complex Gaussian, it can be expressed as a zero mean multivariate Gaussian with covariance matrix Σ_t:

$$\begin{bmatrix} \underline{z}(\omega) \\ \underline{z}(\omega - \Delta\omega) \end{bmatrix} \sim \mathcal{N}\left(\begin{bmatrix} \underline{z}(\omega) \\ \underline{z}(\omega - \Delta\omega) \end{bmatrix}; \underline{\mathbf{0}}, \Sigma_{\mathrm{t}}\right), \tag{5.23}$$

where:

$$\Sigma_t = \sigma_z^2 \begin{bmatrix} 1 & 0 & \mathrm{Re}(a) & -\mathrm{Im}(a) \\ 0 & 1 & \mathrm{Im}(a) & \mathrm{Re}(a) \\ \mathrm{Re}(a) & \mathrm{Im}(a) & 1 & 0 \\ -\mathrm{Im}(a) & \mathrm{Re}(a) & 0 & 1 \end{bmatrix}, \tag{5.24}$$

and, by definition:

$$\sigma_z^2 = k\tau_c \left(1 - e^{-\frac{\tau_t}{\tau_c}}\right), \tag{5.25}$$

$$a = \frac{1}{1 + j\Delta\omega\tau_c} \left(1 - e^{-\tau_t((1/\tau_c) + j\Delta\omega)}\right) \left(1 - e^{-\frac{\tau_t}{\tau}}\right)^{-1}. \tag{5.26}$$

The conditional distribution of $(z(\omega)|z(\omega - \Delta\omega))$ can also be found, letting the realisation of $z(\omega - \Delta\omega) = z_{\omega-\Delta\omega}$:

$$(z(\omega)|z(\omega - \Delta\omega)) \sim \mathcal{N}(\underline{\mu}_a, \Sigma_a), \tag{5.27}$$

where:

$$\underline{\mu}_a = \underline{A}\underline{z}_{\omega-\Delta\omega}, \tag{5.28}$$

and:

$$\Sigma_a = \sigma_z^2 \begin{bmatrix} 1 - |a|^2 & 0 \\ 0 & 1 - |a|^2 \end{bmatrix}, \tag{5.29}$$

thus proving Proposition 5.1.

Experimental evidence to support Proposition 5.1

Proposition 5.1 follows directly from the known properties of the channel impulse response, with one exception. It has been implicitly assumed that, to an infinitely fine resolution, the impulse response can be split into ZMCS Independent Identically Distributed (IID) Gaussian random variables. In reality, the impulse response consists of many arriving rays, and the frequency response should be approximately equal to that derived in Proposition 5.1 if many rays arrive during a time interval during which the magnitude of the PDP does not change significantly. To investigate if this is true, the frequency domain measurements from Measurement Campaign 1.1a are used. Only the values in the frequency range 13 – 17 GHz are included, because, as explained in Section 4.1.4, the fading model is only valid within a frequency band which is narrow relative to the carrier frequency (note that the purpose of using this frequency band is merely to lend experimental support to the theoretical results rather than to limit the theoretical applicability to this frequency band alone).

From (5.5), (5.6) and (5.7) it is known:

$$P(\mathrm{Re}(\underline{z}_i - \underline{A}\underline{z}_{i-1})) = \mathcal{N}\left(\mathrm{Re}(\underline{z}_i - \underline{A}\underline{z}_{i-1}); \underline{0}, \Sigma_a\right), \tag{5.30}$$

$$P(\mathrm{Im}(\underline{z}_i - \underline{A}\underline{z}_{i-1})) = \mathcal{N}\left(\mathrm{Im}(\underline{z}_i - \underline{A}\underline{z}_{i-1}); \underline{0}, \Sigma_a\right), \tag{5.31}$$

where:

$$\Sigma_a = \sigma_z^2 \begin{bmatrix} 1-|a|^2 & 0 \\ 0 & 1-|a|^2 \end{bmatrix}, \tag{5.32}$$

and noticing that the response is effectively for a linear time-invariant channel and thus truncation of the PDP is not necessary. This is equivalent to letting $\tau_t \to \infty$ in (5.8):

$$a = \frac{1}{1 + j\tau_c \Delta\omega}. \tag{5.33}$$

Substituting $\Delta\omega = 20$ MHz (which has been chosen arbitrarily), and $\tau_c = 17.2$ ns (i.e., from Chapter 4) into (5.33), yields: $a = 0.176 - j0.381$. The measurements are normalised such that $\sigma_z^2 = 1$. Fig. 5.1 shows the real part of the measured data, against the theoretical result shown in (5.30). Likewise Fig. 5.2 shows the imaginary part of the measured data, against the theoretical result shown in (5.31). Clearly, there is a good agreement between the theoretical distribution and the measurements, thus providing experimental evidence to support the theoretical derivation. It is therefore appropriate to proceed with the information theoretic analysis assuming Proposition 5.1 to be valid.

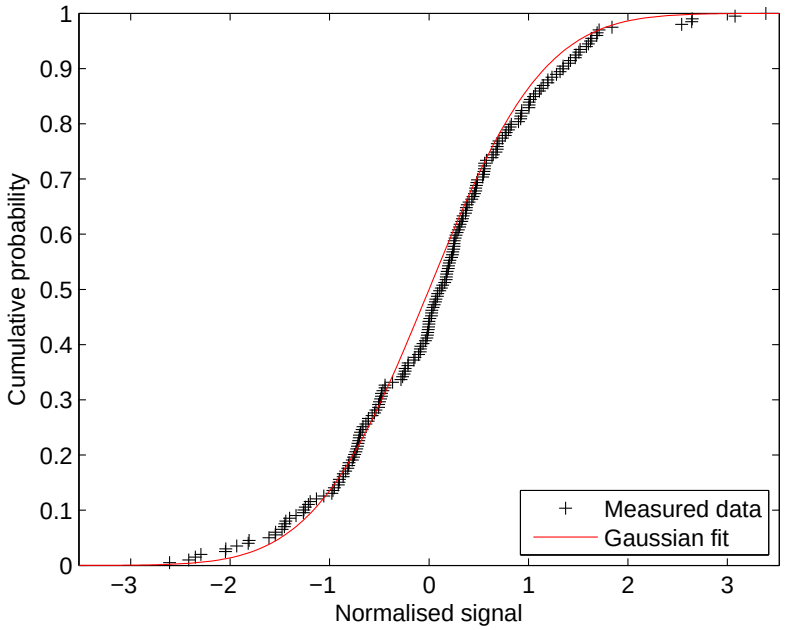

Figure 5.1: Conditional distribution, real part

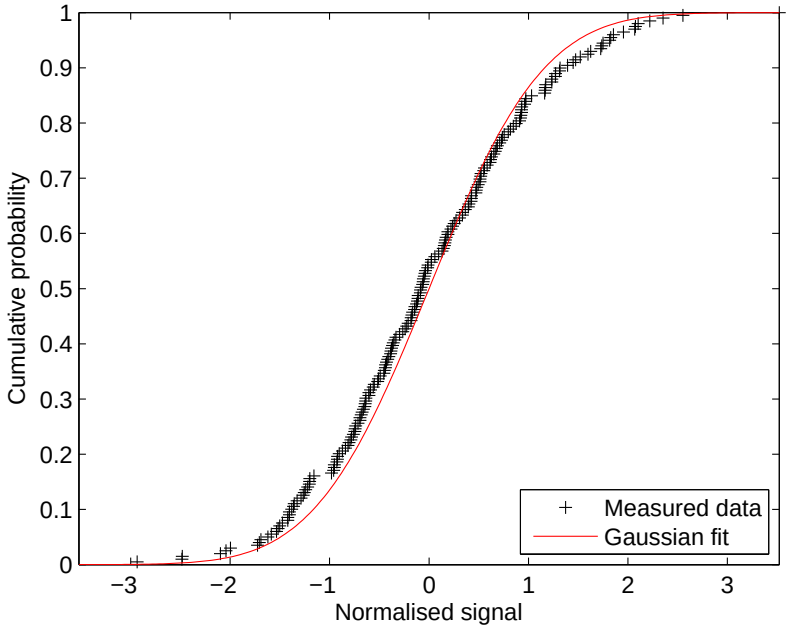

Figure 5.2: Conditional distribution, imaginary part

5.2 Using orthogonal frequency division multiplexing to find an achievable rate

Consider a block fading model [49, 85], where the continuously varying channel is split into blocks in which the fading is treated as identical, i.e., the channel remains virtually unchanged within one block. To find an achievable rate, an Orthogonal Frequency Division Multiplexing (OFDM) [49, 85] scheme is used. Owing to the fact that the channel is highly underspread, the block length can be chosen such that it is much longer than the truncated version of the PDP, $\mathrm{P}'(\tau)$.

The assumption that the channel has the Wide-Sense Stationary Uncorrelated Scattering property (i.e., from Assumptions 1, 2 and 3 in Chapter 4) means that, without loss of generality, the energy associated with the part of the channel impulse response which does vary during a block, and that owing to the part of the impulse response removed during the truncation to form $\mathrm{P}'(\tau)$, can both be treated as AWGN.

The channel is therefore split into blocks of length, T_B, each of which has a cyclic prefix of length, $T_t \geq \tau_t$, which can be chosen to be negligible compared to the block length (again due to the highly underspread property). T_B and T_t must be chosen such that WT_B and WT_t are integers (where W is the bandwidth, and $N = WT_B$ is the total number of subcarriers).

According to the Sampling Theorem [44, 48], the waveform in one block can be reconstructed from samples spaced $1/2W$ s apart. Performing an Inverse Discrete Fourier Transform (IDFT) on the resulting vector of samples (i.e., in the time domain) yields a vector of samples in the frequency domain. These are spaced $1/T_B$ Hz apart. Choosing to define the input signal in the frequency domain, the channel can be expressed:

$$\boldsymbol{y} = \boldsymbol{z} \odot \boldsymbol{x} + \boldsymbol{n}, \tag{5.34}$$

where $\boldsymbol{y}$ is a vector of outputs, $\boldsymbol{z}$ is a vector of the channel frequency response, $\boldsymbol{x}$ is a vector of the channel symbols, $\boldsymbol{n}$ is a vector of AWGN samples and $\odot$ denotes element-wise multiplication. All these vectors are of size $N = WT_B$. Noting that all the elements of the vectors are complex then (5.34) can be expressed:

$$\underline{\boldsymbol{y}} = \underline{Z}\underline{\boldsymbol{x}} + \underline{\boldsymbol{n}}. \tag{5.35}$$

Noting that the cyclic prefix allows cyclic convolution to be treated as linear convolution (i.e., as if the channel were LTI), the channel frequency response can be expressed:

$$P(\underline{z}_i) = \mathcal{N}\left(\underline{z}_i; \underline{0}, \Sigma_z\right), \tag{5.36}$$

$$P(\underline{z}_i | \underline{z}_{i-1}) = \mathcal{N}\left(\underline{z}_i; \underline{\mu}_a, \Sigma_a\right), \tag{5.37}$$

where:

$$\underline{\mu}_a = \underline{A}\underline{z}_{i-1}, \tag{5.38}$$

$$\Sigma_a = \sigma_z^2 \begin{bmatrix} 1-|a|^2 & 0 \\ 0 & 1-|a|^2 \end{bmatrix}, \tag{5.39}$$

where:

$$a = \frac{1}{1+j\tau_c/T_B}\left(1-e^{-\tau_t((1/\tau_c)+j/T_B)}\right)\left(1-e^{-\frac{\tau_t}{\tau_c}}\right)^{-1}, \tag{5.40}$$

i.e., by substituting $\Delta\omega = 1/T_B$ into (5.8). Notice that if the truncated part of $\mathrm{P}'(\tau)$ contains all but a negligible part of the power (i.e., $\tau_t \to \infty$):

$$a \approx \frac{1}{1+j\tau_c/T_B}, \tag{5.41}$$

and so when the channel is highly underspread (i.e., $T_B >> \tau_c$), then $a \approx 1$ and $\Sigma_a \approx 0$. Thus there is little variation in the channel frequency response given the previous frequency response. This is to be expected, and it is this property which allows the lower bound to be found.

5.3 A lower bound on the channel capacity

There is a non-zero probability that for any given time block, the channel will be in outage, however considering the channel as a whole (i.e., across several independent time blocks), an achievable rate, R, can be defined using the Channel Coding Theorem [48]:

$$\mathrm{R} \geq \frac{1}{N}\mathcal{I}(\boldsymbol{x}_0^{N-1}; \boldsymbol{y}_0^{N-1}) \text{ bit s}^{-1} \text{ Hz}^{-1}, \tag{5.42}$$

subject to:

$$\mathrm{P}_{\text{ave}} \geq \lim_{N'\to\infty} \frac{1}{N'} \sum_{i=0}^{N'-1} |x_i|^2, \tag{5.43}$$

where $\mathcal{I}(.;.)$ is mutual information and P_{ave} is the average power constraint. Note that this average is defined across an infinite number of input symbols, x_i, and thus an infinite number of time blocks.

The input distribution on x is chosen to be a series of IID ZMCS Gaussian random variables:

$$\underline{x}_i \sim \mathcal{N}(\underline{x}_i; \underline{0}, \Sigma_x), \tag{5.44}$$

where:

$$\Sigma_x = \begin{bmatrix} \sigma_x^2 & 0 \\ 0 & \sigma_x^2 \end{bmatrix} \tag{5.45}$$

Likewise, the additive white noise is modelled as IID ZMCS Gaussian random variables:

$$\underline{n}_i \sim \mathcal{N}(\underline{n}_i; \underline{0}, \Sigma_n), \tag{5.46}$$

where:

$$\Sigma_n = \begin{bmatrix} \sigma_n^2 & 0 \\ 0 & \sigma_n^2 \end{bmatrix}. \tag{5.47}$$

5.3.1 Bounding idea

The aim is to lower bound (5.42). In essence, the bounding method is similar to a *Kalman* filter [86], where the 'state' is the channel response at the discrete frequencies corresponding to the input (i.e., where successive frequency responses are correlated) and the noisy measurement is formed by the information signal input-output pair. For each successive discrete frequency response, some CSI is learned, and thus eventually (assuming the discrete frequency responses are very close together) the CSI approaches perfect CSI.

There is no feedback in the system, i.e., because successive values of x_i have no dependence on previous values of y_i, z_i or n_i. This property is used throughout the bounding process to simplify various expressions.

Theorem 5.2:

There exists a lower bound, L_1, on the achievable rate:

$$\mathrm{R} \geq \mathrm{L}_1 = \frac{1}{N} \sum_{i=0}^{N-1} \mathcal{I}_i \text{ bit s}^{-1} \text{ Hz}^{-1}, \tag{5.48}$$

where:

$$\mathcal{I}_i = \mathbb{E}\left(\log_2 \left(\frac{|\mu_i'|^2 \sigma_x^2 + \sigma_n^2}{|x_i|^2 \sigma_i^2 + \sigma_n^2} \right) \right), \tag{5.49}$$

and:

$$\sigma_i^2 = \begin{cases} \sigma_z^2 & \text{if } i = 0 \\ (1 - |a|^2)\sigma_z^2 + |a|^2(\sigma_{i-1}^{-2} + |x_{i-1}|^2 \sigma_n^{-2})^{-1} & \text{if } i > 0 \end{cases} \tag{5.50}$$

$$\underline{\mu}_i' \sim \mathcal{N}\left(\underline{\mu}_i'; \underline{0}, \begin{bmatrix} \sigma_z^2 - \sigma_i^2 & 0 \\ 0 & \sigma_z^2 - \sigma_i^2 \end{bmatrix} \right). \tag{5.51}$$

The term σ_i^2 and $\underline{\mu}_i'$ represent the variance and mean of the estimate of the i^{th} frequency response respectively. The term σ_i^2 generally decreases with i, and notice that as $\sigma_i^2 \to 0$:

$$\mathcal{I}_i \to \mathbb{E}\left(\log_2 \left(1 + |z_i|^2 \frac{\sigma_x^2}{\sigma_n^2} \right) \right), \tag{5.52}$$

i.e., the capacity with perfect receiver CSI [44]. Notice also that σ_i^2, $\underline{\mu}_i'$ and $|x_{i-1}|^2$ are random variables, whose joint distribution can be calculated recursively, thus making it a computationally efficient method to find a lower bound on the capacity.

Proof:

The chain rule of mutual information is used to lower bound the right-hand side (RHS) of (5.42):

$$\begin{aligned}\frac{1}{N}\mathcal{I}(\boldsymbol{x}_0^{N-1};\boldsymbol{y}_0^{N-1}) &= \frac{1}{N}\sum_{i=0}^{N-1}\mathcal{I}(x_i;\boldsymbol{y}_0^{N-1}|\boldsymbol{x}_0^{i-1}) \\ &= \frac{1}{N}\sum_{i=0}^{N-1}\sum_{j=0}^{N-1}\mathcal{I}(x_i;y_j|\boldsymbol{x}_0^{i-1},\boldsymbol{y}_0^{j-1}) \\ &\geq \frac{1}{N}\sum_{i=0}^{N-1}\mathcal{I}(x_i;y_i|\boldsymbol{x}_0^{i-1},\boldsymbol{y}_0^{i-1}),\end{aligned} \tag{5.53}$$

where $\mathcal{I}(.;.)$ is mutual information.

Lemma 5.3

For the channel defined in (5.35), the mutual information can be evaluated thus:

$$\mathcal{I}(x_i;y_i|\boldsymbol{x}_0^{i-1},\boldsymbol{y}_0^{i-1}) = \mathcal{I}(x_i;y_i|\hat{z}_i), \tag{5.54}$$

where:

$$\hat{z}_i = P(z_i|\boldsymbol{x}_0^{i-1},\boldsymbol{y}_0^{i-1}). \tag{5.55}$$

Proof:

$$\begin{aligned}\mathcal{I}(x_i;y_i|\boldsymbol{x}_0^{i-1},\boldsymbol{y}_0^{i-1}) &= \mathcal{H}(x_i|\boldsymbol{x}_0^{i-1},\boldsymbol{y}_0^{i-1}) - \mathcal{H}(x_i|y_i,\boldsymbol{x}_0^{i-1},\boldsymbol{y}_0^{i-1}) \\ &= \mathcal{H}(x_i) - \mathcal{H}(x_i|y_i,\boldsymbol{x}_0^{i-1},\boldsymbol{y}_0^{i-1}),\end{aligned} \tag{5.56}$$

where $\mathcal{H}(.)$ is entropy. Regarding the second term of the RHS of (5.56), consider:

$$\begin{aligned}P(x_i|y_i,\boldsymbol{x}_0^{i-1},\boldsymbol{y}_0^{i-1}) &= \int_{z_i} P(x_i|z_i,y_i,\boldsymbol{x}_0^{i-1},\boldsymbol{y}_0^{i-1})P(z_i|y_i,\boldsymbol{x}_0^{i-1},\boldsymbol{y}_0^{i-1})\,\mathrm{d}z_i \\ &= \int_{z_i} P(x_i|z_i,y_i)P(z_i|y_i,\boldsymbol{x}_0^{i-1},\boldsymbol{y}_0^{i-1})\,\mathrm{d}z_i,\end{aligned} \tag{5.57}$$

notice that for the second term on the RHS of (5.57), y_i and $(\boldsymbol{x}_0^{i-1}, \boldsymbol{y}_0^{i-1})$ are conditionally independent given z_i, thus:

$$\begin{aligned} P(z_i|y_i, \boldsymbol{x}_0^{i-1}, \boldsymbol{y}_0^{i-1}) &= \mathrm{f}\left(P(z_i|y_i), P(z_i|\boldsymbol{x}_0^{i-1}, \boldsymbol{y}_0^{i-1})\right) \\ &= \mathrm{f}\left(P(z_i|y_i), \hat{z}_i\right) \\ &= P(z_i|y_i, \hat{z}_i), \end{aligned} \tag{5.58}$$

where $\mathrm{f}(.)$ is a function. Therefore, substituting (5.58) into (5.57):

$$\begin{aligned} P(x_i|y_i, \boldsymbol{x}_0^{i-1}, \boldsymbol{y}_0^{i-1}) &= P(x_i|y_i, \hat{z}_i) \\ \implies \mathcal{H}(x_i|y_i, \boldsymbol{x}_0^{i-1}, \boldsymbol{y}_0^{i-1}) &= \mathcal{H}(x_i|y_i, \hat{z}_i), \end{aligned} \tag{5.59}$$

substituting (5.59) into (5.56)

$$\begin{aligned} \mathcal{I}(x_i; y_i|\boldsymbol{x}_0^{i-1}, \boldsymbol{y}_0^{i-1}) &= \mathcal{H}(x_i) - \mathcal{H}(x_i|y_i, \hat{z}_i) \\ &= \mathcal{I}(x_i; y_i|\hat{z}_i), \end{aligned} \tag{5.60}$$

which proves Lemma 5.3.

Lemma 5.4:

For the channel defined in (5.35), the conditional distribution of the frequency response, z_i, given all previous realisations of the input, x_i, and output, y_i is a Gaussian distribution:

$$(\underline{z}_i|\underline{\boldsymbol{x}}_0^{i-1}, \underline{\boldsymbol{y}}_0^{i-1}) \sim \mathcal{N}(\underline{z}_i; \underline{\mu}_i, \Sigma_i - \Sigma_\epsilon), \tag{5.61}$$

where :

$$\Sigma_i = \begin{bmatrix} \sigma_i^2 & 0 \\ 0 & \sigma_i^2 \end{bmatrix}, \tag{5.62}$$

$$\sigma_i^2 = \begin{cases} \sigma_z^2 & \text{if } i = 0 \\ (1 - |a|^2)\sigma_z^2 + |a|^2(\sigma_{i-1}^{-2} + |x_{i-1}|^2\sigma_n^{-2})^{-1} & \text{if } i \neq 0 \end{cases} \tag{5.63}$$

$$\leq \sigma_z^2, \tag{5.64}$$

$$\underline{\mu}_i \sim \mathcal{N}(\mu_i; \underline{0}, \Sigma_z - (\Sigma_i - \Sigma_\epsilon)), \tag{5.65}$$

and Σ_ϵ is some Positive Definite Symmetric (PDS) matrix or zero.

Proof:

Lemma 5.4 is proven using mathematical induction, for $i = 0$:

$$\underline{z}_0 \sim \mathcal{N}(\underline{z}_0; \underline{0}, \Sigma_z), \tag{5.66}$$

which is true by definition, as there are no previous values of x_i and y_i upon which z_0 is conditioned.

Next, it is shown that if Lemma 5.4 is true for $\underline{z}_{i-1}$ then it is also true for $\underline{z}_i$

$$P(z_i|\boldsymbol{x}_0^{i-1}, \boldsymbol{y}_0^{i-1}) = \int_{z_{i-1}} P(z_i|z_{i-1}, \boldsymbol{x}_0^{i-1}, \boldsymbol{y}_0^{i-1}) P(z_{i-1}|\boldsymbol{x}_0^{i-1}, \boldsymbol{y}_0^{i-1}) \, \mathrm{d}z_{i-1}. \tag{5.67}$$

Consider the first term in the integrand in (5.67)

$$P(z_i|z_{i-1}, \boldsymbol{x}_0^{i-1}, \boldsymbol{y}_0^{i-1}) = P(z_i|z_{i-1}, \boldsymbol{x}_0^{i-2}, \boldsymbol{y}_0^{i-2}), \tag{5.68}$$

and it is known from Proposition 5.1 that:

$$(\underline{z}_i|\underline{z}_{i-1}) \sim \mathcal{N}(\underline{z}_{i-1}; \underline{A}\underline{z}_{i-1}, \Sigma_a). \tag{5.69}$$

Consider the multivariate Gaussian:

$$\begin{aligned}\begin{bmatrix} \underline{z}_i & | & \underline{z}_{i-1}, \boldsymbol{x}_0^{i-2} \\ \boldsymbol{y}_0^{i-2} & | & \underline{z}_{i-1}, \boldsymbol{x}_0^{i-2} \end{bmatrix} &= \begin{bmatrix} \underline{z}_i & | & \underline{z}_{i-1} \\ \boldsymbol{y}_0^{i-2} & | & \underline{z}_{i-1}, \boldsymbol{x}_0^{i-2} \end{bmatrix} \\ &\sim \mathcal{N}\left(\begin{bmatrix} \underline{z}_i \\ \boldsymbol{y}_0^{i-2} \end{bmatrix}; \begin{bmatrix} \underline{A}\underline{z}_{-1} \\ \underline{\boldsymbol{\alpha}} \end{bmatrix}, \begin{bmatrix} \Sigma_a & \beta \\ \beta^T & \delta \end{bmatrix} \right),\end{aligned} \tag{5.70}$$

where the values of $\underline{\boldsymbol{\alpha}}$, β and δ are unimportant for this analysis. Therefore:

$$\begin{aligned} P(\underline{z}_i|\underline{z}_{i-1}, \boldsymbol{x}_0^{i-1}, \boldsymbol{y}_0^{i-1}) &= \mathcal{N}(\underline{z}_i; \underline{A}\underline{z}_{i-1} + \underline{\mu}_\epsilon, \Sigma_a - \Sigma'_\epsilon) \\ \implies P(\underline{A}^{-1}\underline{z}_i|\underline{z}_{i-1}, \boldsymbol{x}_0^{i-1}, \boldsymbol{y}_0^{i-1}) &= \mathcal{N}(\underline{A}^{-1}\underline{z}_i; \underline{z}_{i-1} + \underline{A}^{-1}\underline{\mu}_\epsilon, \\ &\qquad \underline{A}^{-1}\Sigma_a\underline{A}^{-T} - \underline{A}^{-1}\Sigma'_\epsilon\underline{A}^{-T}), \end{aligned} \tag{5.71}$$

where the value of $\underline{\mu}_\epsilon$ is unimportant for this analysis, as is $\Sigma'_\epsilon = \beta^T\delta^{-1}\beta$ which is a PDS matrix (i.e., because δ is a covariance matrix), or zero if the underlying process is actually a Markov process.

Consider the second term of the integrand in (5.67), and notice that it can be split into two conditionally independent terms:

$$(\underline{z}_{i-1}|\underline{x}_{i-1}, \underline{y}_{i-1}) \sim \mathcal{N}\left(\underline{z}_{i-1}; \underline{X}_{i-1}^{-1}\underline{y}_{i-1}, |x_{i-1}|^2\Sigma_n\right), \tag{5.72}$$

$$(\underline{z}_{i-1}|\underline{\boldsymbol{x}}_0^{i-2}, \underline{\boldsymbol{y}}_0^{i-2}) \sim \mathcal{N}\left(\underline{z}_{i-1}; \underline{\mu}_{i-1}, \Sigma_{i-1} - \Sigma''_\epsilon\right), \tag{5.73}$$

i.e., from the definition of Lemma 5.4 in (5.61). This expression is valid for $i = 1$, as $\underline{\boldsymbol{x}}_0^{i-2}, \underline{\boldsymbol{y}}_0^{i-2}$ consists of no elements, and thus it represents the unconditional distribution of $\underline{z}_0$, which is valid by the definition in (5.63), i.e., with $\Sigma''_\epsilon = 0$.

The conditional independence allows (5.72) and (5.73) to be fused together as a Kalman filter [86], i.e., in which the pair (x_{i-1}, y_{i-1}) forms a measurement, and there exists some prior estimate of the state $P(z_{i-1}|\boldsymbol{x}_0^{i-2}, \boldsymbol{y}_0^{i-2})$. This leads to:

$$(\underline{z}_{i-1}|\underline{\boldsymbol{x}}_0^{i-1}, \underline{\boldsymbol{y}}_0^{i-1}) \sim \mathcal{N}(\underline{z}_{i-1}; \underline{\mu}_\alpha, \Sigma_\alpha), \tag{5.74}$$

where the value of $\underline{\mu}_\alpha$ is unimportant for this analysis, and:

$$\begin{aligned}
\Sigma_\alpha &= \left(|x_{i-1}|^2\Sigma_n^{-1} + (\Sigma_{i-1} - \Sigma_\epsilon'')^{-1}\right)^{-1} && (5.75)\\
&= \left(|x_{i-1}|^2\Sigma_n^{-1} + \Sigma_{i-1}^{-1} + (\Sigma_\epsilon''')^{-1}\right)^{-1} && (5.76)\\
&= \left(|x_{i-1}|^2\Sigma_n^{-1} + \Sigma_{i-1}^{-1}\right)^{-1} - \Sigma_\epsilon'''', && (5.77)
\end{aligned}$$

where Σ_ϵ''' and Σ_ϵ'''' are PDS matrices. Lemma 5.5 is applied to $(\Sigma_{i-1} - \Sigma_\epsilon'')^{-1}$ in (5.75), noticing that Σ_{i-1} is proportional to the identity, to derive (5.76). Lemma 5.6 is applied to the RHS of (5.76), noticing that $(|x_{i-1}|^2\Sigma_n^{-1} + \Sigma_{i-1}^{-1})$ is proportional to the identity, to derive (5.77). The Lemma's are stated and proved in Appendix C.

Substituting (5.71) and (5.74) into (5.67), and performing the resulting convolution yields:

$$\begin{aligned}
P(z_i|\boldsymbol{x}_0^{i-1}, \boldsymbol{y}_0^{i-1}) &= \mathcal{N}\left(\underline{A}^{-1}\underline{z}_i; \underline{A}^{-1}\underline{\mu}_\epsilon + \underline{\mu}_\alpha, \underline{A}^{-1}\Sigma_a\underline{A}^{-T} - \underline{A}^{-1}\Sigma_\epsilon'\underline{A}^{-T} + \Sigma_\alpha\right)\\
&= \mathcal{N}\left(\underline{z}_i; \underline{\mu}_\epsilon + \underline{A}\underline{\mu}_\alpha, \Sigma_a - \Sigma_\epsilon' + \underline{A}\Sigma_\alpha\underline{A}^T\right)\\
&= \mathcal{N}\left(\underline{z}_i; \underline{\mu}_i, \Sigma_i - \Sigma_\epsilon\right), && (5.78)
\end{aligned}$$

where $\underline{\mu}_i$ is defined later in (5.83), and by performing substitutions from (5.7) and (5.77):

$$\begin{aligned}
\Sigma_\epsilon &= \Sigma_\epsilon' + \Sigma_\epsilon'''', && (5.79)\\
\Sigma_i &= \Sigma_a + |a|^2(\Sigma_{i-1}^{-1} + |x_{i-1}|^2\Sigma_n^{-1})^{-1}\\
&= (1 - |a|^2)\Sigma_z + |a|^2(\Sigma_{i-1}^{-1} + |x_{i-1}|^2\Sigma_n^{-1})^{-1}. && (5.80)
\end{aligned}$$

Noticing that if Σ_{i-1} is proportional to the identity, then so is Σ_i, let:

$$\Sigma_i = \begin{bmatrix} \sigma_i^2 & 0 \\ 0 & \sigma_i^2 \end{bmatrix}, \tag{5.81}$$

where:

$$\sigma_i^2 = (1 - |a|^2)\sigma_z^2 + |a|^2(\sigma_{i-1}^{-2} + |x_{i-1}|^2\sigma_n^{-2})^{-1}. \tag{5.82}$$

Consider that the overall distribution of z must be preserved, regardless of the input and noise, therefore:

$$\underline{\mu}_i \sim \mathcal{N}(\underline{0}, \Sigma_z - (\Sigma_i - \Sigma_\epsilon)). \tag{5.83}$$

To prove the final part of Lemma 5.4, i.e., that $\sigma_z^2 \geq \sigma_i^2$, consider again proof by induction. From (5.66) it is known that $\sigma_0^2 = \sigma_z^2$, and thus consider (5.82):

$$\begin{aligned}\sigma_z^2 &\geq \sigma_{i-1}^2 \\ &\geq (\sigma_{i-1}^{-2} + |x_{i-1}|^2\sigma_n^{-2})^{-1} \\ &\geq (1-|a|^2)\sigma_z^2 + |a|^2(\sigma_{i-1}^{-2} + |x_{i-1}|^2\sigma_n^{-2})^{-1} \\ &= \sigma_i^2. \end{aligned} \tag{5.84}$$

Proof of Theorem 5.2 (continued):

Using Lemma 5.3 to consider only the i^{th} frequency response, z_i, which is itself a random variable, from (5.35):

$$\underline{y}_i = \underline{Z}_i\underline{x}_i + \underline{n}_i, \tag{5.85}$$

and as shown in Lemma 5.4, z_i is a circularly symmetric Gaussian random variable, thus decomposing z_i such that:

$$\underline{z}_i' \sim \mathcal{N}\left(\underline{z}_i'; \underline{0}, \Sigma_i\right), \tag{5.86}$$

it follows that:

$$\underline{y}_i = \underline{M}_i\underline{x}_i + \underline{Z}_i'\underline{x}_i + \underline{n}_i, \tag{5.87}$$

where M is the capitalised version of μ, i.e., for the purposes of representing complex multiplication as a matrix operation. Further decomposing μ, such that:

$$\underline{\mu}_i' \sim \mathcal{N}(\underline{\mu}_i'; \underline{0}, \Sigma_z - \Sigma_i), \tag{5.88}$$

$$\underline{\mu}_i'' \sim \mathcal{N}(\underline{\mu}_i''; \underline{0}, \Sigma_\epsilon). \tag{5.89}$$

(5.87) can be expressed:

$$\underline{y}_i = \underline{M}_i'\underline{x}_i + \underline{M}_i''\underline{x}_i + \underline{Z}_i'\underline{x}_i + \underline{n}_i. \tag{5.90}$$

Consider the mutual information:

$$\mathcal{I}(x_i; y_i|\hat{z}_i) = \mathcal{H}(y_i|\hat{z}_i) - \mathcal{H}(y_i|x_i, \hat{z}_i). \tag{5.91}$$

Consider the first term of the RHS of (5.91):

$$\begin{aligned}\mathcal{H}(y_i|\hat{z}_i) &\geq \mathcal{H}(y_i|\hat{z}_i, z_i') \\ &= \log_2(2\pi e|\underline{M}_i'\Sigma_x(\underline{M}_i')^T + \underline{M}_i''\Sigma_x(\underline{M}_i'')^T + \underline{Z}_i'\Sigma_x(\underline{Z}_i')^T + \Sigma_n|^{1/2}) \\ &\geq \log_2(2\pi e||\mu_i|^2\Sigma_x + \Sigma_n|^{1/2}). \end{aligned} \tag{5.92}$$

Consider the second term of the RHS of (5.91):

$$\begin{aligned}\mathcal{H}(y_i|x_i,\hat{z}_i)=&\log_2(2\pi e|\underline{X}_i(\Sigma_i-\Sigma_\epsilon)\underline{X}_i^T+\Sigma_n|^{1/2})\\ =&\log_2\left(2\pi e||x_i|^2(\Sigma_i-\Sigma_\epsilon)+\Sigma_n|^{1/2}\right) \quad (5.93)\\ \leq&\log_2(2\pi e||x_i|^2\Sigma_i+\Sigma_n|^{1/2}), \quad (5.94)\end{aligned}$$

where (5.94) is derived from (5.93) by noticing that all terms within the determinant in (5.93) are proportional to the identity, except Σ'_ϵ which is PDS (as $\Sigma_i-\Sigma_\epsilon$ is a covariance matrix). Therefore applying Lemma 5.7, as detailed in Appendix C, yields this result.

Substituting (5.92) and (5.94) into (5.91):

$$\begin{aligned}\mathcal{I}(x_i;y_i|\hat{z}_i)&=\mathcal{H}(y_i|\hat{z}_i)-\mathcal{H}(y_i|x_i,\hat{z}_i)\\ &\geq\log_2(2\pi e||\mu'_i|^2\Sigma_x+\Sigma_n|^{1/2})-\log_2(2\pi e||x_i|^2\Sigma_i+\Sigma_n|^{1/2})\\ &=\log_2\left(\frac{|\mu'_i|^2\sigma_x^2+\sigma_n^2}{|x_i|^2\sigma_i^2+\sigma_n^2}\right)\\ &=\mathcal{I}_i, \quad (5.95)\end{aligned}$$

which proves Theorem 5.2.

Corollary 5.8:

There exists a lower bound, L_2, on the achievable rate:

$$\mathrm{R}\geq\mathrm{L}_2=\frac{1}{N}\sum_{i=0}^{N-1}\mathcal{I}'_i \text{ bit s}^{-1}\text{ Hz}^{-1}, \quad (5.96)$$

where:

$$\mathcal{I}'_i=\mathbb{E}\left(\max\left(\log_2\left(\frac{|\mu'_i|^2\sigma_x^2+\sigma_n^2}{|x_i|^2\sigma_i^2+\sigma_n^2}\right),0\right)\right). \quad (5.97)$$

Proof:

$$\mathcal{H}(y_i|\hat{z}_i)-\mathcal{H}(y_i|x_i,\hat{z}_i)\geq 0, \quad (5.98)$$

substituting (5.98) into (5.95):

$$\begin{aligned}\mathcal{I}(x_i;y_i|\hat{z}_i)&\geq\mathbb{E}\left(\max\left(\log_2\left(\frac{|\mu'_i|^2\sigma_x^2+\sigma_n^2}{|x_i|^2\sigma_i^2+\sigma_n^2}\right),0\right)\right)\\ &=\mathcal{I}'_i, \quad (5.99)\end{aligned}$$

which proves Corollary 5.8.

Corollary 5.9:

The lower bounds L_1 and L_2 can themselves be lower bounded by $\mathrm{L}_{1\mathrm{A}}$ and $\mathrm{L}_{2\mathrm{A}}$ respectively, by noticing that the sequence $\mathcal{I}(x_i; y_i|\hat{z}_i)$ is monotonically non-decreasing, and therefore a lower bound on the i^{th} term is automatically a lower bound on the $(i+j)^{\text{th}}$ term, $j \geq 0$. This is potentially useful as it means computation of the mutual information could be halted when a sufficiently tight lower bound has been achieved.

$$\mathrm{R} \geq \mathrm{L}_1 \geq \mathrm{L}_{1\mathrm{A}} = \frac{1}{N}\left(\sum_{i=0}^{N''-1} \mathcal{I}_i + (N - N'')\mathcal{I}_{N''}\right), \tag{5.100}$$

$$\mathrm{R} \geq \mathrm{L}_2 \geq \mathrm{L}_{2\mathrm{A}} = \frac{1}{N}\left(\sum_{i=0}^{N''-1} \mathcal{I}'_i + (N - N'')\mathcal{I}'_{N''}\right), \tag{5.101}$$

where:

$$0 < N'' \leq N. \tag{5.102}$$

Proof:

For $j > 0$, consider (5.95), and using Lemma 5.3:

$$\begin{aligned}\mathcal{I}(x_i; y_i|\hat{z}_i) &= \mathcal{H}(x_i|\hat{z}_i) - \mathcal{H}(x_i|y_i, \hat{z}_i) \\ &= \mathcal{H}(x_i|\boldsymbol{x}_0^{i-1}, \boldsymbol{y}_0^{i-1}) - \mathcal{H}(x_i|y_i, \boldsymbol{x}_0^{i-1}, \boldsymbol{y}_0^{i-1}) \\ &= \mathcal{H}(x_i) - \mathcal{H}(x_i|y_i, \boldsymbol{x}_0^{i-1}, \boldsymbol{y}_0^{i-1}),\end{aligned} \tag{5.103}$$

and:

$$\begin{aligned}\mathcal{I}(x_{i+j}; y_{i+j}|\hat{z}_{i+j}) &= \mathcal{H}(x_{i+j}|\boldsymbol{x}_0^{i+j-1}, \boldsymbol{y}_0^{i+j-1}) - \mathcal{H}(x_{i+j}|y_{i+j}, \boldsymbol{x}_0^{i+j-1}, \boldsymbol{y}_0^{i+j-1}) \\ &= \mathcal{H}(x_{i+j}) - \mathcal{H}(x_{i+j}|y_{i+j}, \boldsymbol{x}_0^{i+j-1}, \boldsymbol{y}_0^{i+j-1}),\end{aligned} \tag{5.104}$$

Therefore:

$$\begin{aligned}\mathcal{I}(x_{i+j}; y_{i+j}|\hat{z}_{i+j}) - \mathcal{I}(x_i; y_i|\hat{z}_i) &= \mathcal{H}(x_i|y_i, \boldsymbol{x}_0^{i-1}, \boldsymbol{y}_0^{i-1}) - \mathcal{H}(x_{i+j}|y_{i+j}, \boldsymbol{x}_0^{i+j-1}, \boldsymbol{y}_0^{i+j-1}) \\ &\geq 0,\end{aligned} \tag{5.105}$$

because the two terms in the RHS differ only by conditioning, and conditioning reduces entropy. Noticing that exactly the same analysis can be applied to $\mathcal{I}'_i$, this is a sufficient condition to prove Corollary 5.9.

5.4 Numerical example for the vehicle-like cavity

From the measurements presented in Chapter 4, it is possible to evaluate a lower bound on the information capacity of a wireless system operating in the vehicle-like cavity. A suitable example application is a wireless sensor network operating using *Zigbee* [62]. To evaluate the lower bound, it is necessary to find appropriate parameters to substitute into the expressions (5.48), (5.49), (5.50) and (5.51). These parameters derive from the fundamental parameters (i.e., the cavity time constant and system Signal to Noise Ratio SNR) via the parameters required to model the channel as a block fading system (i.e., the block length, cyclic prefix length and the adjustment to the SNR to account for the block fading model).

5.4.1 Parameters

The capacity of a channel with perfect receiver CSI can be expressed:

$$\begin{aligned} C &= \mathbb{E}\left(\log_2\left(1+|z|^2\frac{\sigma_x^2}{\sigma_n^2}\right)\right) \\ &= \mathbb{E}\left(\log_2\left(1+|z''|^2\frac{\sigma_z^2\sigma_x^2}{\sigma_n^2}\right)\right) \\ &= \mathbb{E}\left(\log_2\left(1+|z''|^2\mathrm{SNR}\right)\right), \end{aligned} \tag{5.106}$$

where, by definition:

$$\underline{z}'' \sim \mathcal{N}\left(\underline{z}''; \underline{0}, \begin{bmatrix} 1 & 0 \\ 0 & 1 \end{bmatrix}\right), \tag{5.107}$$

$$\mathrm{SNR} = \frac{\sigma_z^2\sigma_x^2}{\sigma_n^2}. \tag{5.108}$$

It can be shown that the specified 250 kbit/s for a single Zigbee channel (i.e., a frequency band of width 5 MHz) can be achieved at an SNR of 0.0180 (for this analysis it is irrelevant that actual Zigbee systems would typically have a much higher SNR).

From Chapter 4, and as used previously in this chapter in Section 5.1, the vehicle-like cavity time constant is 17.2 ns. Regarding the choice of block length, T_B, an appropriate criteria (i.e., for this example) is the time duration during which 0.99 of the energy is expected to remain undisturbed. Noting that the different types of stirring (i.e., in Fig. 4.11) have similar characteristics, it is most straightforward to find the time block length for the mechanically stirred scenario, as the Autocorrelation Function (ACF) has been found at 2.45 GHz (i.e., in Fig. 4.9). Approximately 1/10 of a stirrer step appears to fit the requirement that 0.99 of the energy is expected to be undisturbed (i.e., the autocorrelation co-efficient is 0.99). Noting that there are 100 stirrer steps in a full revolution, and that the stirrer operates at 0.19 revolutions per second leads

to a value of $T_B = 0.0053$ s. This result can be used to show: $N = 26500$ and $\Delta\omega = 189$ Hz. This method of finding the time block length, i.e., extrapolating the ACF to fractions of a stirrer step, is quite coarse, however alternative estimates have been made (i.e., from the Doppler spread graphs in Chapter 4), leading to time block lengths of the same order of magnitude.

Regarding the choice of cyclic prefix length, T_t, and noting that this must correspond to an integer number of samples in the time domain (i.e., according to the Sampling Theorem), consider choosing just a single time sample duration to be the cyclic prefix. This is equal to 200 ns, and the portion of the energy which is not expected to arrive during the same time block in which it was transmitted, $\mathbb{E}\left(\mathrm{E}_{\text{leak}}\right)$, can be evaluated:

$$\begin{aligned}\mathbb{E}\left(\mathrm{E}_{\text{leak}}\right) &= 1 - \frac{1}{\tau_c}\int_0^{T_t} e^{-\frac{\tau}{\tau_c}}\,\mathrm{d}\tau \\ &= e^{-\frac{T_t}{\tau_c}} \\ &= 8.91 \times 10^{-6},\end{aligned} \tag{5.109}$$

where $T_t = 200$ ns, note that the term $1/\tau_c$ is included for normalisation, such that the total energy is unity. To allow for the fact that only 0.99 of the energy actually does not vary during one time block, and that $1-8.91\times10^{-6}$ of the energy leaks from one time block into subsequent time blocks, it is necessary to adjust the SNR. This is achieved by assuming that an infinite number of time blocks have preceded the current one, and treating the energy leaking into the current time block (i.e., from previous time blocks) as noise, and also treating the energy which varies within one time block as noise:

$$\begin{aligned}\text{SNR}' &= \frac{\text{SNR} \times 0.99 \times (1 - 8.91 \times 10^{-6})}{1 + \text{SNR}(1 - 0.99 \times (1 - 8.91 \times 10^{-6}))} \\ &= \frac{0.018 \times 0.99 \times (1 - 8.91 \times 10^{-6})}{1 + 0.018(1 - 0.99 \times (1 - 8.91 \times 10^{-6}))} \\ &= 0.0178,\end{aligned} \tag{5.110}$$

where SNR' is the adjusted SNR.

Substituting τ_c, T_B and $\tau_t = T_t$ into (5.40) yields $|a|^2 = 1 - 1.03 \times 10^{-11}$. To determine appropriate values of σ_z^2, σ_x^2 and σ_n^2, the adjusted SNR is sufficient. As one parameter is used to determine three parameters, there is some choice and it necessary to establish whether the bounding method imposes any restrictions on this choice.

Proposition 5.10

The bound in (5.48) relies only on the value of SNR as defined in (5.108), and not the individual realisations of σ_z^2, σ_x^2 and σ_n^2.

Proof:

Using the location scale property of the Gaussian distribution, let:

$$\begin{aligned} x_i' &= \frac{1}{\sigma_x} x_i \\ &\sim \mathcal{N}\left(x_i'; \underline{0}, \begin{bmatrix} 1 & 0 \\ 0 & 1 \end{bmatrix}\right), \end{aligned} \tag{5.111}$$

$$\begin{aligned} (\sigma_i')^2 &= \frac{1}{\sigma_z^2}\sigma_i^2 \\ &= (1-|a|^2) + |a|^2 \left((\sigma_{i-1}')^{-2} + \frac{\sigma_z^2\sigma_x^2}{\sigma_n^2}|x_{i-1}'|^2\right)^{-1}, \end{aligned} \tag{5.112}$$

$$\begin{aligned} \mu_i''' &= \frac{1}{\sigma_z}\mu_i \\ &\sim \mathcal{N}\left(\mu_i'''; \underline{0}, \begin{bmatrix} 1-(\sigma_i')^2 & 0 \\ 0 & 1-(\sigma_i')^2 \end{bmatrix}\right). \end{aligned} \tag{5.113}$$

Substituting the results into (5.48) yields:

$$\begin{aligned} \mathcal{I}_i &= \mathbb{E}\left(\log_2\left(\frac{\sigma_z^2|\mu_i'''|^2\sigma_x^2 + \sigma_n^2}{\sigma_x^2|x_i'|^2\sigma_z^2(\sigma_i')^2 + \sigma_n^2}\right)\right) \\ &= \mathbb{E}\left(\log_2\left(\frac{\frac{\sigma_z^2\sigma_x^2}{\sigma_n^2}|\mu_i'''|^2 + 1}{\frac{\sigma_z^2\sigma_x^2}{\sigma_n^2}|x_i'|^2(\sigma_i')^2 + 1}\right)\right). \end{aligned} \tag{5.114}$$

Therefore (5.112), (5.113) and (5.114) show that the bound only relies on $\sigma_z^2\sigma_x^2/\sigma_n^2$, thus proving Proposition 5.10.

Given that the choice of σ_z^2, σ_x^2 and σ_n^2 is arbitrary, so long as they combine to form the correct SNR, $\sigma_z^2 = 0.5$, $\sigma_x^2 = 0.0356$ and $\sigma_n^2 = 1$ are chosen. A summary of all the parameters is given in Table 5.1.

Table 5.1: Summary of parameters.

Type	**Name**	**Value**
Fundamental	τ_c	1.7×10^{-8} s
	W	5×10^{6} Hz
	SNR	1.80×10^{-2}
Block fading & OFDM	T_B	5.30×10^{-3} s
	T_t	2×10^{-7} s
	N	26500
	$\Delta\omega$	1.89×10^{2} Hz
	SNR'	1.78×10^{-2}
Lower bound	$\lvert a\rvert^2$	$1 - 1.03 \times 10^{-11}$
	σ_z^2	5×10^{-1}
	σ_x^2	3.56×10^{-2}
	σ_n^2	1

5.4.2 Results

The lower bound L_2, i.e., from (5.96), has been found for the parameters specified in Section 5.4.1. It should, however, be noted that to rigorously lower bound the channel, it is necessary to take into account the fact that no information is transferred during the cyclic prefix:

$$\begin{aligned} C &\geq \mathrm{L}_{2\mathrm{B}} \\ &= \mathrm{L}_2 \times \frac{T_B}{T_B + T_t}, \end{aligned} \tag{5.115}$$

where $\mathrm{L}_{2\mathrm{B}}$ is the lower bound.

The result of the bounding process is shown in Fig. 5.3. Also shown, in Fig. 5.4, is a detailed close-up of the bound at low values of bandwidth. The main obstacle to tightness of the bound is the adjustment to the SNR, and the main contribution comes from the energy which varies during one coherence time interval. Therefore, if T_B could be shortened such that, for example, 0.999 of the energy is expected to not vary, then the bound will tighten accordingly. For the purposes of demonstrating the principle of the bound, however, these plots are sufficient.

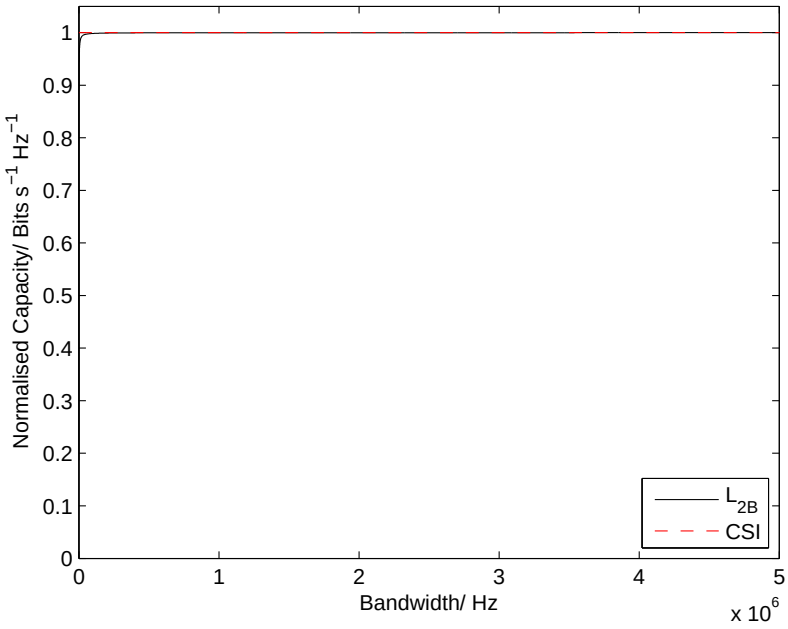

Figure 5.3: Capacity lower bound

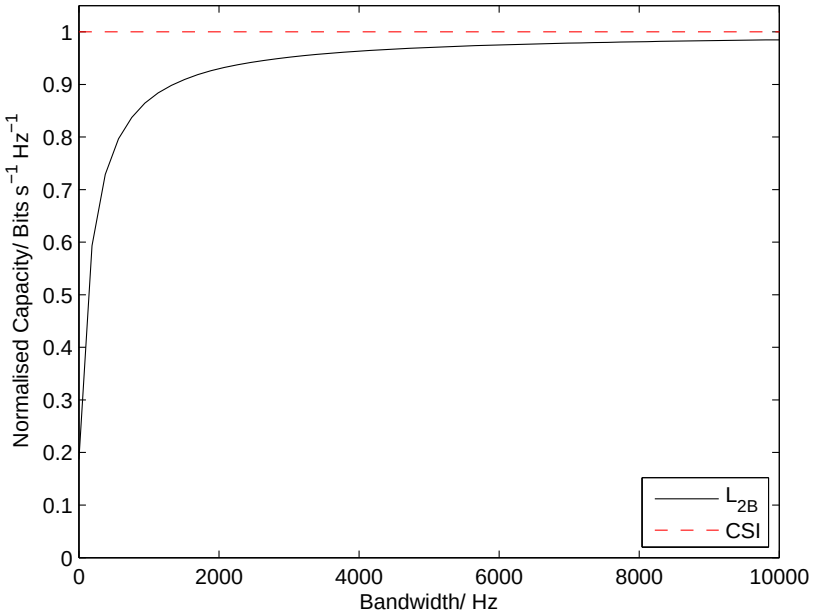

Figure 5.4: Capacity lower bound (detailed)

5.5 Chapter summary

Having established that the channel is highly underspread (to a very good approximation), it is to be expected that the information capacity approaches that of an AWGN channel with perfect receiver CSI. Nonetheless, it is desirable to demonstrate this rigorously by lower bounding the channel capacity.

This has been achieved by expressing the channel as a block fading model, and using an OFDM scheme to find an achievable rate. The input for each block is defined in the frequency domain, at constant discrete frequency intervals. The frequency correlation is used to learn CSI at the receiver, through a Kalman filter. The derived bound is strictly a lower bound on the channel capacity.

The bound has been evaluated for typical in-vehicle channel. The time variation and cavity time constant found in Chapter 4 were used, along with a typical value of SNR, to find the parameters required for the bound. It was found that the lower bound is indeed approximately the AWGN capacity, with perfect receiver CSI.

Chapter 6

The analogy between vehicle cavities and reverberation chambers

As elaborated upon in Chapter 2, there is an implicit assumption in much of the published literature that the Electromagnetic (EM) environment in vehicle cavities is closely related to that in a reverberation chamber. Also the propagation model for the in-vehicle channel, derived in Chapter 4 from a general set of starting assumptions, has an exponentially decaying Power Delay Profile (PDP), as is the case for the reverberation chamber. It is therefore of interest to investigate at a deeper level to what extent reverberation chamber properties apply to vehicle cavities.

Having established the extent to which reverberation chamber analysis can be applied to vehicle cavities, it is then important to demonstrate how this can be used to improve communication systems deployed in vehicles. This is achieved by using reverberation chamber analysis to estimate, for in-vehicle channels, the delay spread, angular spread, and coherence distance, which are important parameters for the deployment of effective wireless communication systems.

6.1 Investigating whether reverberation chamber properties apply to vehicle cavities

The reverberation chamber has five definitive properties (also detailed in Chapter 2):

I. The energy retained in the cavity at time τ, after a unit impulse input of energy at $\tau = 0$ is proportional to $e^{-\frac{\tau}{\tau_c}}$, where τ_c is the cavity time constant.

II. The reverberation chamber is an isolated EM environment.

III. Within the working volume, the Electric Field (EF) distribution is isotropic.

IV. Within the working volume, the EF distribution is homogeneous.

V. Within the working volume, the EF distribution is ergodic, i.e., the same field distribution can be obtained by sampling in frequency or time (if a well designed stirrer is deployed to vary the EF).

The working volume is defined for any given reverberation chamber as a certain integer of half-wavelengths from the cavity walls [17]. Together, properties III, IV and V define a *uniform* EF distribution. With regard to Property V, under normal operating conditions, vehicle cavities do not have well designed stirrers, therefore the property of ergodicity does not necessarily apply (although it should be noted that a stirrer has been introduced for some of the experiments presented in this chapter).

6.1.1 In vehicle power delay profile

Reverberation chamber Property I, from Section 6.1 means that the PDP for a wireless link in a reverberation chamber decays exponentially (a link is the communication channel between two antennas at known locations, the term link is used to avoid ambiguity with 'channel' which is used for different communication frequencies for any given link). This is consistent with the derivation of the impulse response in Chapter 4. However, within a given cavity it has not been determined whether the time constant is necessarily the same for each link.

To investigate this further, Measurement Campaigns 1.2, 1.3, 1.4 and 1.5 are used, which consist of frequency sweeps between 0.5 – 3 GHz or 1 – 3 GHz, with step size 5 MHz. In each case, only the part of the frequency sweep between 1 – 3 GHz is used, as between 0.5 – 1 GHz the antenna efficiency is unknown. These campaigns include measurements in four environments: the vehicle-like cavity, the front of the van, the rear of the van and the car, and in each case the

loading in the cavity has been varied. For the measurement in the vehicle-like cavity, the stirrer was switched off.

A simplified version of the process detailed in Section 4.1.1, I – VII, is used to infer the PDP from the frequency sweep measurements:

$$\mathbf{p} = \left| \text{IDFT}\left(\frac{\boldsymbol{s}_{\alpha 1} \odot \boldsymbol{f}}{\sqrt{\eta_{\text{Tx}}\eta_{\text{Rx}}}} \right) \right|^2, \tag{6.1}$$

where $\mathbf{p}$ is a vector of the received power after an impulse input, 'IDFT' is the inverse discrete Fourier transform, $\boldsymbol{s}_{\alpha 1}$ is a vector of the measured values of the forward voltage ratio (where α can be either 2, 3 or 4) corresponding to the vector of frequencies, $\boldsymbol{f}$, at which $\boldsymbol{s}_{\alpha 1}$ was measured (and $\odot$ denotes element-wise multiplication), η_{Tx} is the transmit antenna efficiency and η_{Rx} is the receive antenna efficiency. The resulting time domain response has a resolution of 0.5 ns and a duration of 200 ns.

From Chapter 4, it is known that the PDP, $\mathrm{P}_{\mathbb{H}}$, decays exponentially with time:

$$\begin{aligned} \mathrm{P}_{\mathbb{H}} &= k e^{-\frac{\tau}{\tau_c}} \\ \implies \log_e\left(\mathrm{P}_{\mathbb{H}}\right) &= \log_e k - \frac{\tau}{\tau_c}, \end{aligned} \tag{6.2}$$

where k is a constant, τ is time lapse and τ_c is the cavity time constant.

This enables the time constant to be estimated using a Minimum Mean Square Error (MMSE) linear fit, to the plot of $\mathbf{p}$ against τ in semi-logarithmic form. This is shown for the vehicle-like cavity, the van front, the van rear and the car in Figs. 6.1, 6.2, 6.3 and 6.4 respectively. In each case, the length of time over which the line was fitted was determined heuristically, and so as to apply to all links for the given environment. For each environment, the plot shown is the maximum loading scenario. It is reassuring to observe that, for each plot, it appears that the exponentially decaying model fits the data well.

Table 6.1 shows the time constant estimates for all the links in the vehicle-like cavity and the actual vehicles. For the measurements in the vehicle like cavity, 'loading' refers to the number of units of Radiation Absorbent Material (RAM) and $\tau_{c1} - \tau_{c6}$ refer to τ_{cxz}, τ_{cxx}, τ_{cxy}, τ_{czz}, τ_{czx} and τ_{czy} respectively (i.e., where the first term in the subscript is the polarisation of the transmit antenna, and the second is the polarisation of the receive antenna). For the measurements in the actual vehicles, $\tau_{c1} - \tau_{c6}$ refer to various random antenna locations (and orientations), and 'loading' refers to the number of human occupants. The mean and standard deviation of the six time constants are denoted $\langle \tau_c \rangle$ and σ_{τ_c} respectively. It can be seen that for each environment and loading configurations, that the time constant is approximately equal for all links.

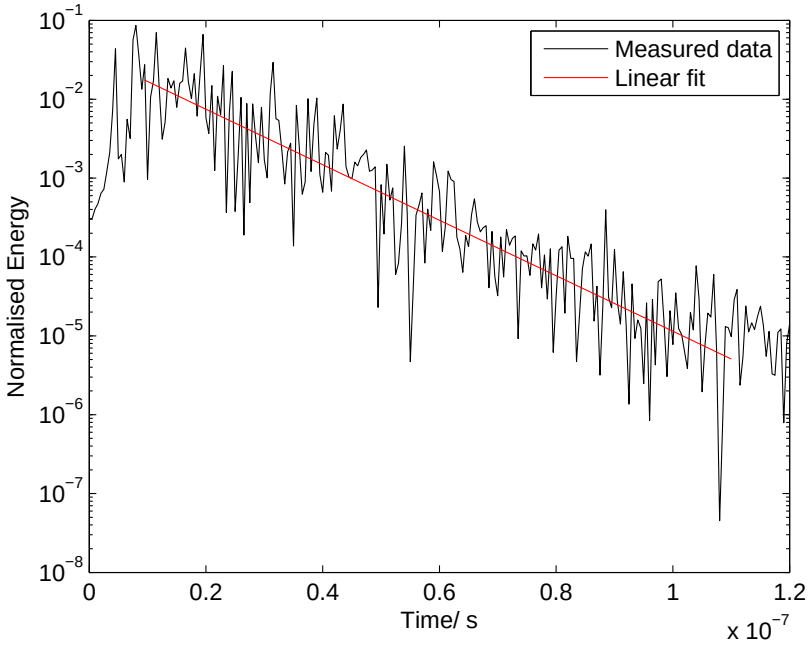

Figure 6.1: Example of exponential decay, vehicle-like cavity loaded with 12 units of RAM

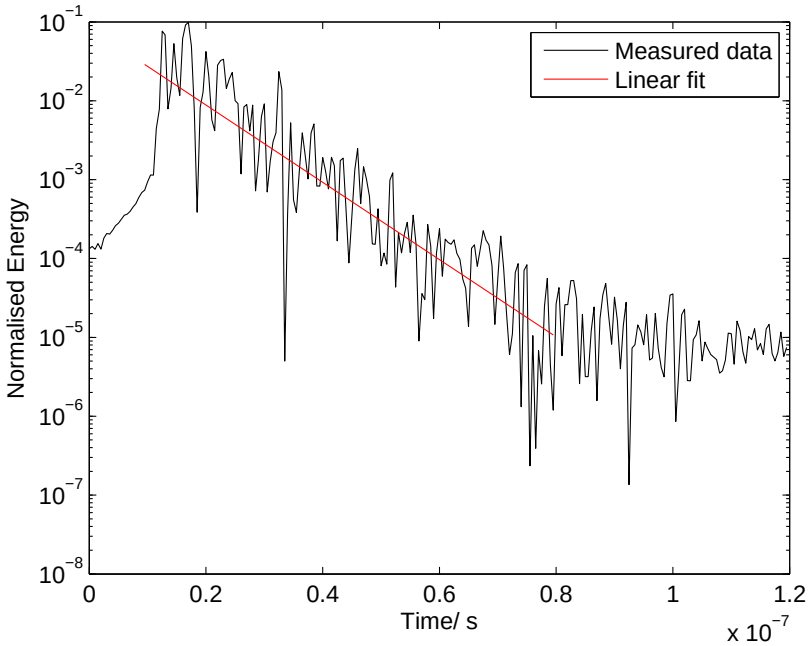

Figure 6.2: Example of exponential decay, front of van with three occupants

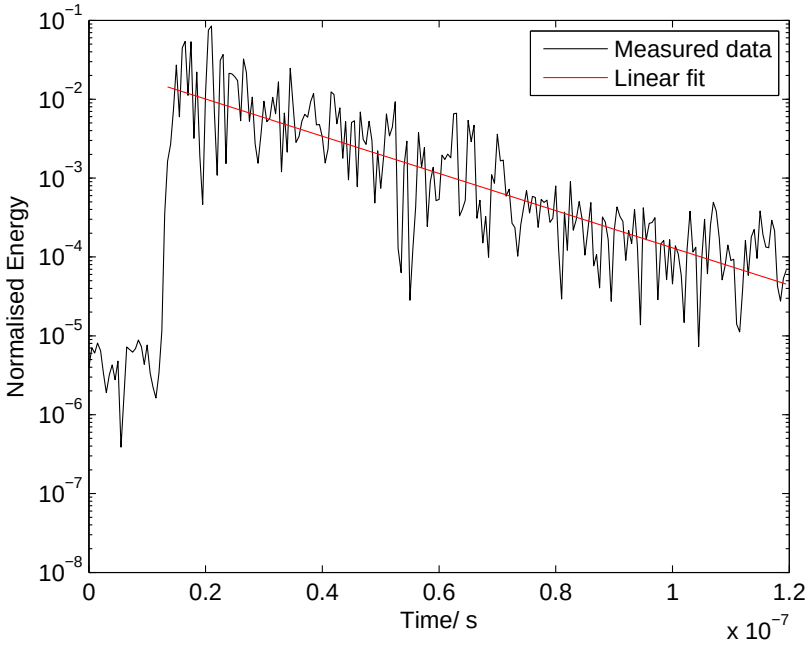

Figure 6.3: Example of exponential decay, rear of van

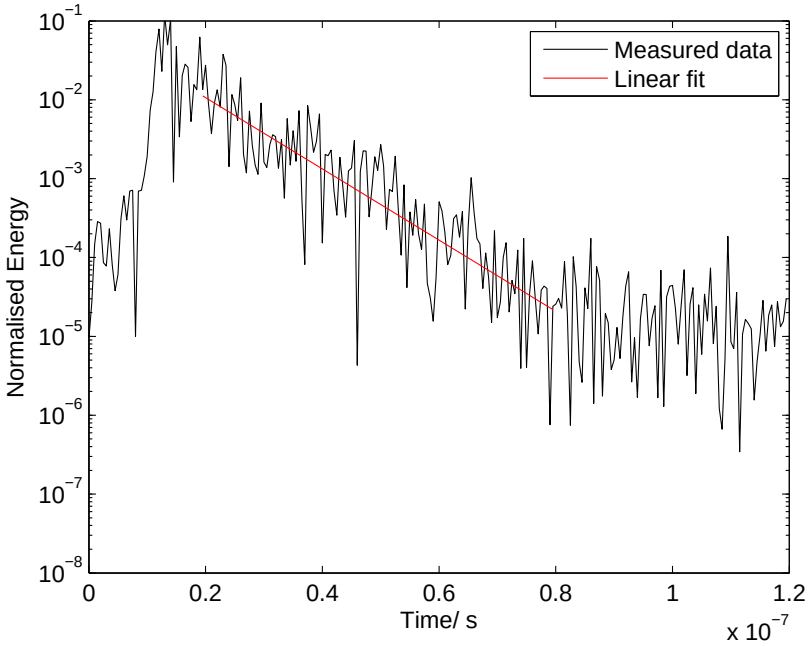

Figure 6.4: Example of exponential decay, car with five occupants

Table 6.1: Time constant estimation for a vehicle-like cavity, and actual vehicles.

Location	**Loading**	**Time constant/ ns**							
		τ_{c1}	τ_{c2}	τ_{c3}	τ_{c4}	τ_{c5}	τ_{c6}	$\langle\tau_c\rangle$	σ_{τ_c}/ **ns**
Vehicle-like cavity	0	22.9	22.8	24.0	26.6	24.4	24.0	24.1	1.38
Vehicle-like cavity	4	17.0	16.2	17.6	17.6	17.7	18.5	17.4	0.77
Vehicle-like cavity	8	14.3	12.9	13.6	13.6	14.5	15.7	14.1	0.97
Vehicle-like cavity	12	13.4	12.1	12.5	13.8	12.7	11.8	12.7	0.76
Car	0	12.4	14.7	15.5	12.9	11.6	14.8	13.6	1.56
Car	1	10.9	12.1	13.3	11.8	12.4	11.6	12.0	0.81
Car	2	10.3	10.8	12.9	12.3	10.2	10.5	11.2	1.14
Car	3	13.0	10.4	10.9	10.7	12.5	12.1	11.6	1.07
Car	4	9.8	11.3	10.3	13.6	10.6	9.8	10.9	1.44
Car	5	10.1	11.1	10.6	9.6	10.7	12.3	10.7	0.93
Van (front)	0	12.1	13.4	15.3	13.4	12.7	13.6	13.4	1.08
Van (front)	1	10.2	9.9	10.9	10.1	9.8	9.8	10.1	0.42
Van (front)	2	7.5	8.1	9.8	10.6	7.5	7.7	8.5	1.33
Van (front)	3	8.3	8.9	9.0	9.3	10.2	6.4	8.7	1.23
Van (rear)	n/a	18.4	18.4	18.4	18.1	17.7	18.6	18.3	0.32

'Loading' in the vehicle-like cavity refers to the number of units of RAM, whereas in the actual vehicles it refers to the number of occupants. All time constant values are given to one decimal place and the standard deviation is given to two decimal places to align the decimal point.

6.1.2 Investigating whether the vehicle cavity is an isolated electromagnetic environment

In general, for an environment to be electromagnetically isolated it must be the case that:

I. The EM wave propagation between that environment and the outside is negligible.

II. Objects outside of the environment have a negligible effect on the EM wave propagation within the environment.

In vehicle cavities, with large apertures (i.e., windows), criteria I clearly does not apply. This has, however, been implicitly accounted for, by the reduction in time constant (i.e., derived in Chapter 4) which accounts for the cavity apertures. Also, that EM waves which originate outside the cavity and propagate in can be considered to be noise, and thus the noise floor estimate can be adjusted accordingly.

Regarding criteria II, it is important to establish whether external objects have an effect on the EM environment in vehicle cavities. This is investigated using the results from Measurement Campaign 1.6, in which a frequency sweep was performed with three different external objects close to the vehicle-like cavity, as well as a measurement where there were no external objects. In each case the time constant was evaluated according to the method detailed in Section 6.1.1, with the time constant only varying a small amount (22.8 – 23.3 ns). It can therefore be concluded that external objects have only a negligible effect on EM wave propagation in vehicles.

6.1.3 Vehicle cavity electric field uniformity

In order for an electric field to be uniform, it must be isotropic and homogeneous (i.e., Properties III and IV in Section 6.1). In general there may not be a stirrer present in the cavity, therefore it is not possible to test for ergodicity (Property V).

Investigating whether the electric field distribution is isotropic

By definition the EF distribution is isotropic if, for any point in the cavity, the three orthogonal components of the EF are Independent Identically Distributed (IID) zero mean circularly symmetric complex Gaussian random variables. In this case the magnitude of the EF for each component will therefore be an IID Rayleigh random variable. To investigate whether this is the case, Measurement Campaign 1.2 is used, with the stirrer on. For each frequency and spatial point, samples from the independent stirrer positions are used, as well as frequency samples out to ± 50 MHz (and the channel frequency is defined at the centre frequency). The EF is found

by noting that $S_{\alpha 1}$ is proportional to the EF (where α denotes Port 2, 3 or 4) and the EF is normalised by setting the greatest sampled value to equal one.

The results are plotted in Figs. 6.5 and 6.6 for 600 MHz and 1.7 GHz respectively. At 600 MHz it appears that the EF is not isotropic, however at 1.7 GHz the plots in Fig. 6.6 provide evidence that the EF distribution may be isotropic. This is because for the pairs of plots in Fig. 6.6 (a), (b); (c), (d); and (e), (f), the antennas were in identical locations, and the only difference was that one was rotated to be orthogonal to its original position (full details are given in Section 3.2.1).

Given that it appears that the EF distribution is isotropic at 1.7 GHz but not at 600 MHz, it is important to establish the lowest frequency at which an EF distribution which is approximately isotropic can be obtained. This is termed the Lowest Usable Frequency (LUF) [17]. Given that an isotropic EF distribution has been obtained at sufficiently high frequencies, there are two conditions required for an isotropic EF distribution to be obtained at a given frequency, f:

I. The distribution of the phase of the arriving rays must be uniform, and independent of the ray magnitude. For this to be the case, it is necessary that the period of the carrier wave is much smaller than the cavity time constant. This can be expressed as: $f >> 1/\tau_c$.

II. The standing EM wave pattern must have at least 60 modes (this is a good general rule, although there is some evidence that isotropic EF distributions can be obtained below this frequency [87]). Strictly speaking this is only valid if the stirrer is very efficient, or there are two independent stirrers, which isn't the case in the vehicle-like cavity (and it is not clear to what extent the frequency stirring mitigates this), therefore the 60 mode rule can only be used as a guideline in this instance.

For a rectangular cavity, 60 modes are present at a frequency approximately 3 times the lowest resonant frequency. The lowest resonant frequency can be found from the equation given by Dawson and Arnaut [80], and for the vehicle-like cavity this is 342 MHz. Therefore the 60 mode rule should apply at frequencies above 1.03 GHz. The lowest value of τ_c is 12.7 ns, when the cavity is loaded with 12 units of RAM, therefore $1/\tau_c = 78.7 \times 10^6$ s^{-1}, and thus $f >> 1/\tau_c$ when $f \geq 1.03$ GHz. The effect of loading not only has an effect on the time constant, it also potentially affects the number of modes, with greater loading leading to fewer modes [88] and therefore a higher LUF. It has also, however, been reported that the opposite effect may happen for example Arnaut shows that the LUF is proportional to the third root of the Quality Factor (QF) (and hence time constant) [89].

The relationship between loading and the EF distribution is therefore unclear, and thus an experimental method is taken to determine the LUF. Applying the same analysis to the data from

Measurement Campaign 1.2 as described previously, plots resembling Figs. 6.5 and 6.6 are generated for all measured frequencies. To determine whether the field distribution is isotropic at a given frequency, a subjective approach is taken, by observing the appearance of the fit of the Rayleigh distribution and the similarity of the orthogonally polarised channel pairs for the given antenna locations. It can also be shown that for a Rayleigh distribution the ratio of the mean to the standard deviation is 1.91, and this can be compared to the same ratio for the measured data to further investigate the goodness of fit of the Rayleigh distribution. The results show that a EF distribution which is close to isotropic can be obtained at frequencies greater or equal to 1.7 GHz and 2.7 GHz for the cavity loaded with 0 and 4 units of RAM respectively. However, for 8 and 12 units of RAM an isotropic EF distribution is not obtained even at the maximum measured frequency of 2.9 GHz. Therefore it appears that the LUF is sensitive to the amount of loading. It should be noted that while a subjective approach has been taken here, for any given application an objective criteria could be applied to decide whether or not the EF distribution is isotropic, and thus the LUF could be found.

To determine whether the EF distribution is uniform, it is required to know whether or not the EF distribution is isotropic. Determining the EF uniformity is important for the Multiple Input Multiple Output (MIMO) and beamforming antenna systems discussed in Section 6.2. Furthermore, much of the information theoretic analysis assumes that the channel response has a zero mean circularly symmetric complex Gaussian distribution, and if the EF distribution is isotropic then this provides a sufficient condition to make this assumption. It is, however, important to note that effective communication is possible below the LUF, and there is a sizeable amount of literature devoted to understanding the statistical properties of EM wave propagation below the theoretical LUF [89–94].

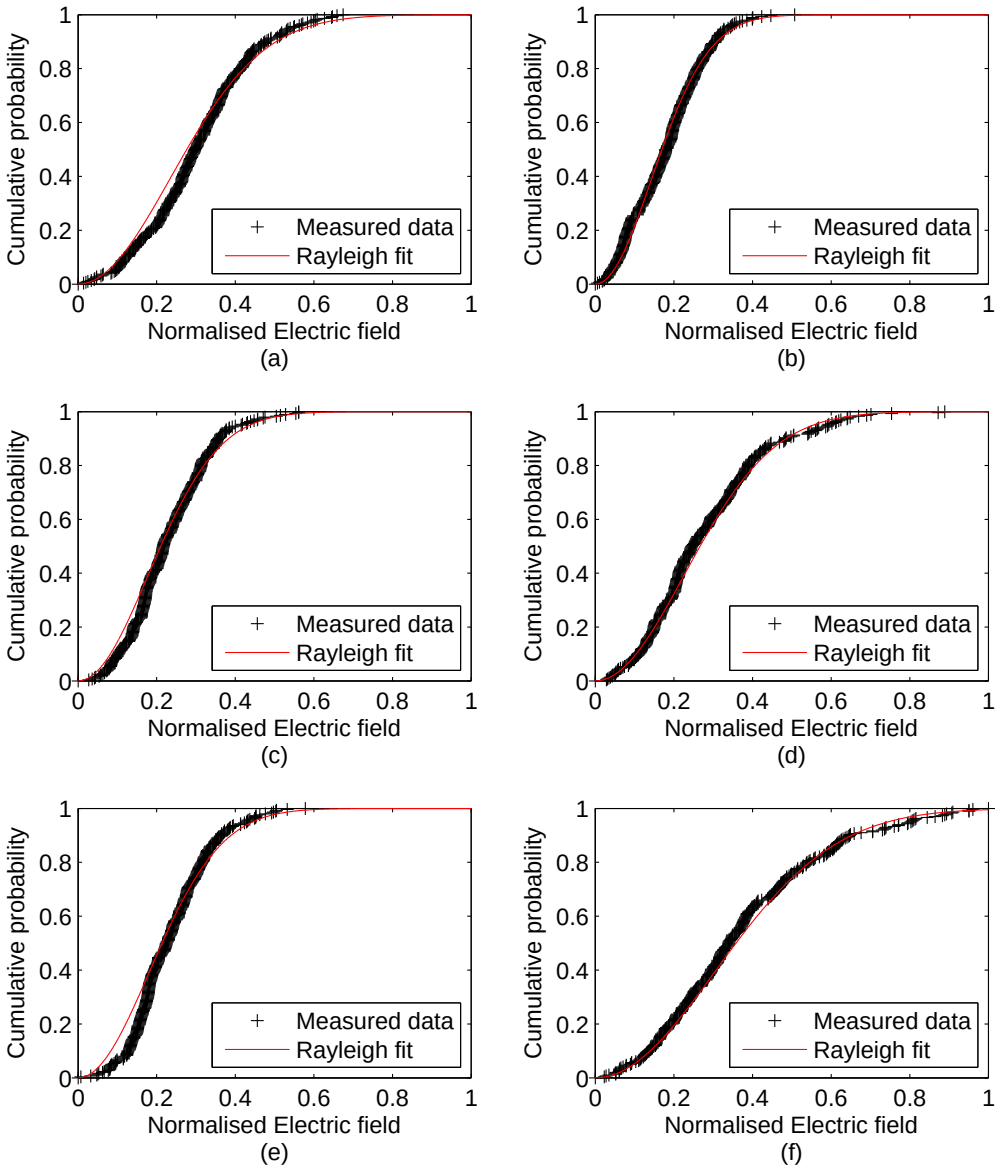

Figure 6.5: Electric field distribution at 600 MHz; cavity loaded with 12 units of RAM: (a) E_{xz}; (b) E_{zz}; (c) E_{xx}; (d) E_{zx}; (e) E_{xy}; (f) E_{zy}

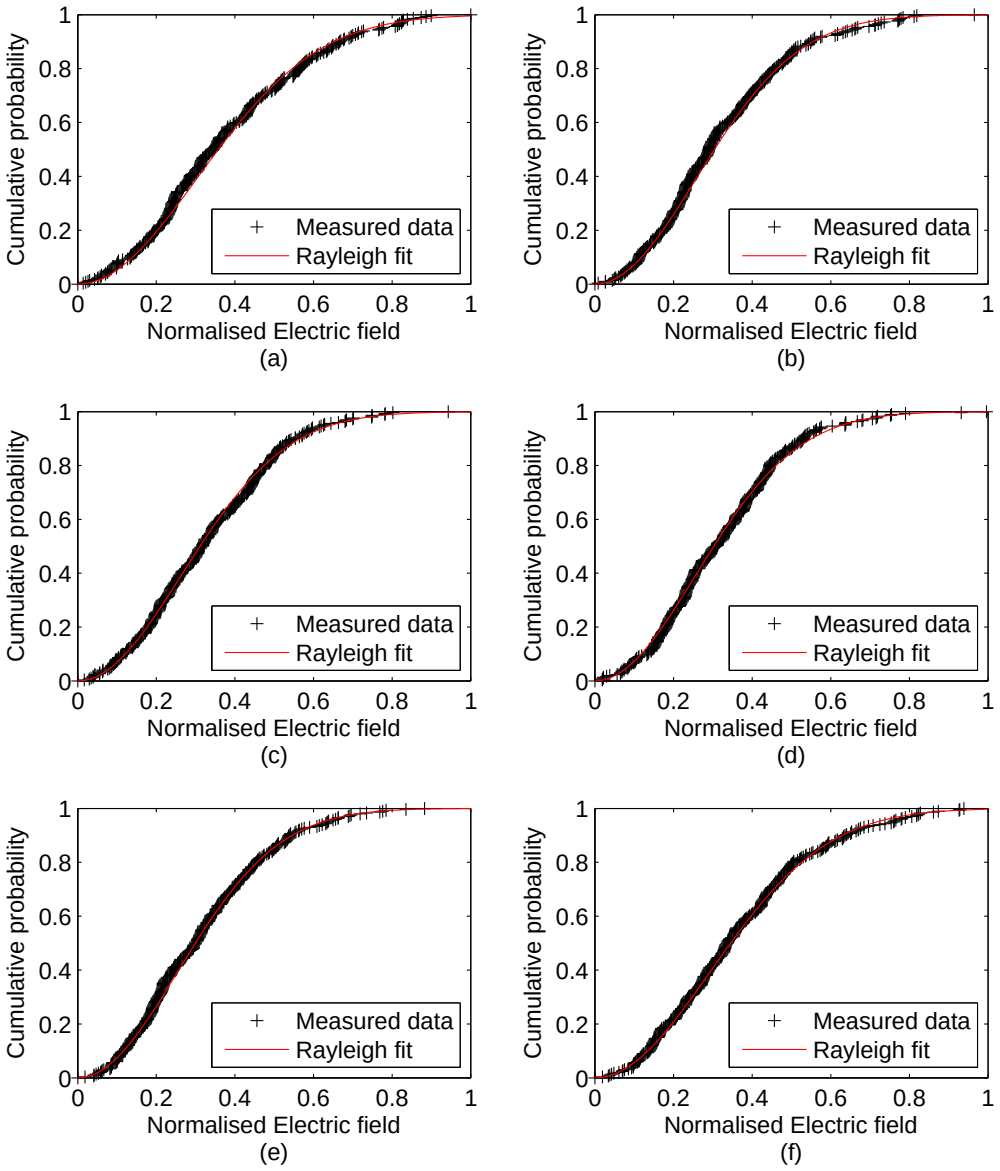

Figure 6.6: Electric field distribution at 1.7 GHz; cavity unloaded: (a) E_{xz}; (b) E_{zz}; (c) E_{xx}; (d) E_{zx}; (e) E_{xy}; (f) E_{zy}

Investigating whether the electric field distribution is homogeneous

To investigate whether the EF distribution is homogeneous, consider the cavity QF, which can be related to the time constant, also detailed previously in (2.3):

$$Q_{\tau_c} = 2\pi f \tau_c, \tag{6.3}$$

where Q is the QF (with the subscript to denote that it has been calculated from the time constant) and f is the frequency of operation. An alternative method to find the QF is using a Power Average method (denoted by the subscript PA), also detailed previously in (2.2):

$$Q_{\text{PA}} = \frac{16\pi^2 V}{\eta_{\text{Tx}}\eta_{\text{Rx}}\lambda^3}\left\langle \frac{\mathrm{P}_{\text{Rx}}}{\mathrm{P}_{\text{Tx}}} \right\rangle, \tag{6.4}$$

where V is the cavity volume; λ is the wavelength; P_{Rx} is the received power; and P_{Tx} is the transmitted power. The average $\langle \mathrm{P}_{\text{Rx}}/\mathrm{P}_{\text{Tx}} \rangle$ takes place over a sufficient number (usually 200 or more) of independent EF realisations, which is typically achieved in a reverberation chamber by using a stirrer. The derivation of (6.4) by Hill [[18] Section 7.6] uses as a starting point the fact that the energy density is equal at all locations in the cavity. Therefore $Q_{\tau_c} = Q_{\text{PA}}$ is a necessary condition for the EF to be homogeneous. Measurements to investigate whether Q_{τ_c} is equal to Q_{PA} are conducted at two frequencies: 1.7 GHz, i.e., the LUF of the unloaded cavity; and 2.45 GHz, i.e., in the Industrial, Scientific and Medical band.

To find Q_{PA} for the vehicle-like cavity, Measurement Campaign 1.2 is used with the stirrer on. To find Q_{PA} for the van (front), van (rear) and car, Measurement Campaigns 1.3, 1.4 and 1.5 are used respectively. The average $\langle \mathrm{P}_{\text{Rx}}/\mathrm{P}_{\text{Tx}} \rangle$ is taken over all links, and for all frequency samples across a bandwidth of 100 MHz (i.e., to introduce extra independent samples at the expense of some frequency resolution). For the vehicle-like cavity, the independent stirrer positions are also included in the average. Q_{τ_c} is calculated using (6.3) from the average of the previous measured values of the time constant, i.e., $\langle \tau_c \rangle$.

The results are presented in Table 6.2. It can be observed that, for all environments, loading and frequency combinations, Q_{τ_c} is not equal to Q_{PA}. Indeed, Q_{τ_c} and Q_{PA} are sufficiently different, that it is not plausible that this has arisen from imperfections in the analysis, such as the cavity volumes only being approximately known for the car and van. It can therefore be concluded that in typical vehicle and vehicle-like cavities the EF is not homogeneous. This is unsurprising, given that the in-vehicle time constant is of the order 10 ns, during which EM waves travel about 3 m, which is of the order of the dimensions of the cavity. Therefore the separation distance of the two antennas is a significant factor in the received energy, and hence the cavity is not homogeneous. The values of in-vehicle QF given in Table 6.2 are consistent with those from previous work, as presented previously in Table 2.1.

Table 6.2: Quality factor estimation.

Location	**Loading**	$\langle\tau_c\rangle$**/ ns**	**1.7 GHz**		**2.45 GHz**	
			Q_{τ_c}	Q_{PA}	Q_{τ_c}	Q_{PA}
Vehicle-like cavity	0	24.1	257	105	371	150
Vehicle-like cavity	4	17.4	186	69	268	110
Vehicle-like cavity	8	14.1	151	60	217	78
Vehicle-like cavity	12	12.7	136	52	196	64
Car	0	13.6	146	162	210	276
Car	1	12.0	128	100	185	354
Car	2	11.2	119	172	172	346
Car	3	11.6	124	63	179	159
Car	4	10.9	116	57	168	206
Car	5	10.7	115	47	165	65
Van (front)	0	13.4	143	4	207	113
Van (front)	1	10.1	108	8	156	66
Van (front)	2	8.5	91	4	131	46
Van (front)	3	8.7	93	2	134	20
Van (rear)	n/a	18.3	251	111	362	123

'Loading' in the vehicle-like cavity refers to the number of units of RAM, whereas in the actual vehicles it refers to the number of occupants. To align the decimal point, all time constants values are given to one decimal place, and all QF *values are given to the nearest integer.*

6.2 Using reverberation chamber properties to improve communication systems in vehicles

A cavity classification system is proposed to establish exactly how the reverberation chamber analysis can lead to improved estimates of wireless communication parameters:

Type I: Properties I – IV in Section 6.1 all apply (as does Property V if a stirrer is deployed), and thus full reverberation chamber analysis can be applied.

Type II: For all possible links in the cavity, i.e., regardless of the locations of antennas and any moveable internal objects, the PDP decays exponentially, with the same time constant. The cavity can be treated as an isolated environment. There is a further division of Type II:

- **II A:** At a point, the EF distribution is isotropic (if the frequency is sufficiently high).
- **II B:** At a point, the EF distribution is not necessarily isotropic.

Type III: For any given link, the PDP decays exponentially, however the time constant is not necessarily the same for each link in the cavity.

The subdivision of Type II cavities is important for determining the angular spread and coherence distance of communication links, as to be discussed in Section 6.2.2. The requirement that the links operate in the working volume of the cavity may not be satisfied for all practical deployments of wireless communication systems in cavities. However, as long as any antennas located close to the cavity walls are designed such that the ground plane is taken into account, the analysis will still apply. For instances where propagation is between two antennas both close to the cavity walls, the effect of any propagation via surface currents is neglected, as this analysis only applies where the EM waves propagate through the cavity.

The Type III cavity model arises as it has been shown in Section 4.1 that in general the PDP for links in EM cavities is exponentially decaying. It should, however, be noted that this derivation assumes that all the rays arrive independently. This is probably not the case for the first few arriving rays, where there may be a clustered structure. Therefore for certain links, where the propagation is dominated by the first few arriving rays, it may be more appropriate to fit a clustered propagation model. An example of this is given by Sawada *et al.* [34], where it is shown that for some links, the earliest arriving clusters dominate the total arriving energy.

As shown in Table 6.1, for each environment and loading scenario, the time constant is approximately equal for all the measured links. However, as shown in Table 6.2 the EF distribution

is not homogeneous. Therefore the Type II channel model is appropriate for the vehicle and vehicle-like cavities. For the vehicle-like cavity, the investigation into whether or not the EF distribution is isotropic enables the subdivision of Type II cavities to be assessed.

From Section 6.1.3, the vehicle-like cavity is a Type IIA cavity when unloaded or loaded with four units of RAM, because isotropic EF distributions have been obtained above 1.7 GHz and 2.7 GHz respectively. As isotropic EF distributions have not been obtained for the vehicle-like cavity loaded with eight or twelve units of RAM, for any of the measured frequencies, it is unknown whether they should be classified as Type IIA or Type IIB cavities.

6.2.1 In-vehicle channel root mean square delay spread

The channel Root Mean Square (RMS) delay spread is an important parameter for effective wireless communication system deployment. Theoretically, in Type II cavities the RMS delay spread should be the same for each link in the cavity as the PDP is the same for each link. It can be shown that the theoretical RMS delay spread, τ_{rms}, is equal to the cavity time constant [95]. Comparing the actual value of τ_{rms} from the measurements to the cavity time constant for each environment and loading configuration, as detailed in Table 6.3, shows that it is indeed the case that the RMS delay spread is approximately equal to the cavity time constant.

This means that the delay spread is common for all links in a Type II cavity (which has been shown to be a good model for many vehicle cavities). This property can be exploited by wireless communication system designers, for example if the cavity time constant is known then when a link is first turned on, there will immediately be information available regarding its delay spread and coherence bandwidth prior to any direct channel estimation. Furthermore, it should be possible to aggregate data from many different links to improve the estimate of the cavity time constant.

From the RMS delay spread, the channel coherence bandwidth can be found [96, 97]. Lee [96] defines the coherence bandwidth as the bandwidth over which the autocorrelation co-efficient is greater or equal to 0.7, and shows that this is equal to $1/(50\tau_{\text{rms}})$. As the coherence bandwidth is a function of the delay spread, it also is common for all links in a Type II cavity. For the environment and loading configurations measured the time constant was found to be between 8.58 and 24.1 ns, leading to coherence bandwidths in the range 0.830 – 2.33 MHz. Other definitions of coherence bandwidth which can be calculated from the RMS delay spread are available [97].

Table 6.3: Root mean square delay spread.

Environment	**Loading**	$\langle\tau_c\rangle$**/ ns**	**RMS delay spread/ ns**					
			$\tau_{\mathrm{rms}\,1}$	$\tau_{\mathrm{rms}\,2}$	$\tau_{\mathrm{rms}\,3}$	$\tau_{\mathrm{rms}\,4}$	$\tau_{\mathrm{rms}\,5}$	$\tau_{\mathrm{rms}\,6}$
Vehicle-like cavity	0	24.1	23.1	23.4	23.5	21.1	24.3	23.7
Vehicle-like cavity	4	17.4	18.5	16.1	18.4	14.3	18.1	16.7
Vehicle-like cavity	8	14.1	13.7	14.0	15.7	11.0	15.3	14.4
Vehicle-like cavity	12	12.7	12.8	11.9	11.9	9.1	12.0	12.0
Car	0	13.6	13.3	13.9	13.7	12.7	12.0	14.0
Car	1	12.0	12.7	12.2	12.4	11.5	12.7	12.2
Car	2	11.2	11.7	10.6	13.0	11.9	9.1	10.9
Car	3	11.6	11.9	10.5	11.1	11.1	11.6	11.3
Car	4	10.9	9.7	11.9	11.6	11.0	10.4	10.5
Car	5	10.7	10.2	10.7	10.8	9.6	10.4	13.0
Van (front)	0	13.4	10.3	12.2	13.2	10.5	10.7	12.2
Van (front)	1	10.1	8.5	10.9	11.5	9.8	8.5	10.2
Van (front)	2	8.5	6.5	7.6	8.1	10.5	7.6	7.0
Van (front)	3	8.7	7.3	8.3	8.7	9.1	9.3	5.2
Van (rear)	n/a	18.3	18.7	16.8	17.7	19.3	17.3	18.1

'Loading' in the vehicle-like cavity refers to the number of units of RAM, whereas in the actual vehicles it refers to the number of occupants. All values are given to one decimal place to align the decimal point.

6.2.2 In-vehicle channel angular spread and coherence distance

Simulation 4.1 is used to investigate the angular spread of EM wave propagation at 1.7 GHz in the vehicle-like cavity. This simulation, detailed in Section 3.3, is for a perfectly incoherent isotropic point source, and hence cannot be used to evaluate the arriving signal. Nonetheless, it is sufficient to investigate the angular spread and arriving energy. Figs. 6.7 and 6.8 show the results for the situation with and without the stirrer respectively. The locations of the transmitter and the receiver are (1000, 880, 510) mm and (300, 490, 440) mm respectively (i.e., corresponding to the first receiver locations in Table 3.4, with similar results achieved at the other two locations). In these figures, plot (a) confirms that the propagation model is consistent with the exponential PDP observed in the measurements, and plots (b), (c) and (d) show the angular spread for three planar cuts. The angular spread appears to be uniform with the stirrer (Fig. 6.8) and close to uniform without the stirrer (Fig. 6.7). This is consistent with the measurements which indicate that the EF distribution is isotropic.

As the angular spread is uniform (and the EF distribution is isotropic), it follows that if the EF is locally homogeneous, then the coherence distance is well defined, i.e., by the analysis undertaken by Hill [[18] Section 7.4]. Simulation 4.2 is used to investigate if the EF distribution is locally homogeneous. The results are presented in Tables 6.4 and 6.5 for the situations without and with the stirrer respectively. The results show that the total received energy varies only by a small amount, and it appears to vary continuously, therefore the EF distribution is indeed locally homogeneous. This leads to a situation where a MIMO antenna array can be used to improve the performance. For example, if the antenna array spans an area over which the EF is homogeneous, then the spatial correlation is well defined, and thus an informed decision can be made as to the spacing of the MIMO elements.

Given that it has been shown that vehicle cavities are typically Type II cavities, the overall conclusion is that in Type IIA cavities a MIMO antenna array can be used to exploit the properties of the EF, given that the coherence distance is well defined. Whereas in Type IIB cavities, where the EF distribution is not necessarily isotropic (and thus the angular spread is not necessarily uniform) beamforming can be used. It has previously been reported that MIMO antenna arrays do lead to performance improvements in vehicles [98–101]. Also, Sawada *et al.* [34] measure channels in a vehicle where the angular spread is not uniform, and it can clearly be seen that beamforming would lead to improvements in performance.

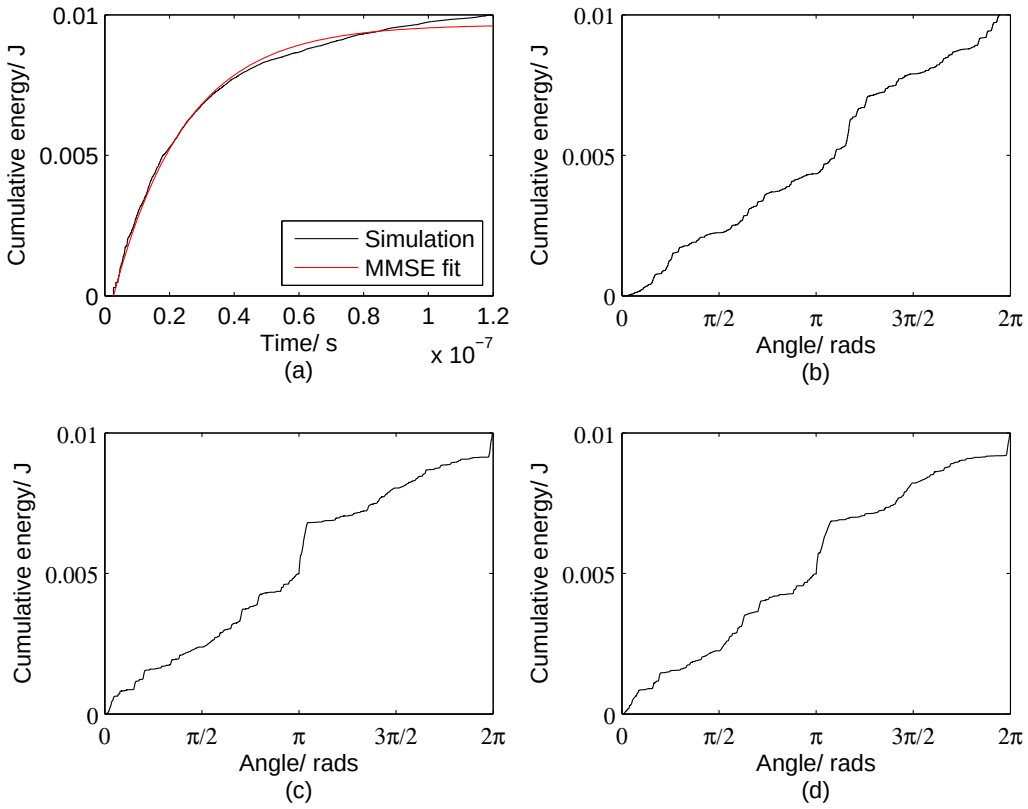

Figure 6.7: Propagation model without stirrer: (a) cumulative energy with time; (b) angular spread in the plane $z = 440$ mm; (c) angular spread in the plane $y = 490$ mm; (d) angular spread in the plane $x = 300$ mm

Table 6.4: Total arriving energy (J) without stirrer, for locations in the plane $x = 300$ mm.

		z **location**				
		413 mm	467 mm	525 mm	581 mm	637 mm
y **location**	328 mm	0.0102	0.0101	0.0104	0.0098	0.0102
	384 mm	0.0102	0.0101	0.0103	0.0097	0.0102
	440 mm	0.0101	0.0100	0.0103	0.0096	0.0100
	496 mm	0.0099	0.0099	0.0101	0.0094	0.0099
	552 mm	0.0100	0.0100	0.0102	0.0094	0.0099

All values are given to four decimal places to align the decimal point.

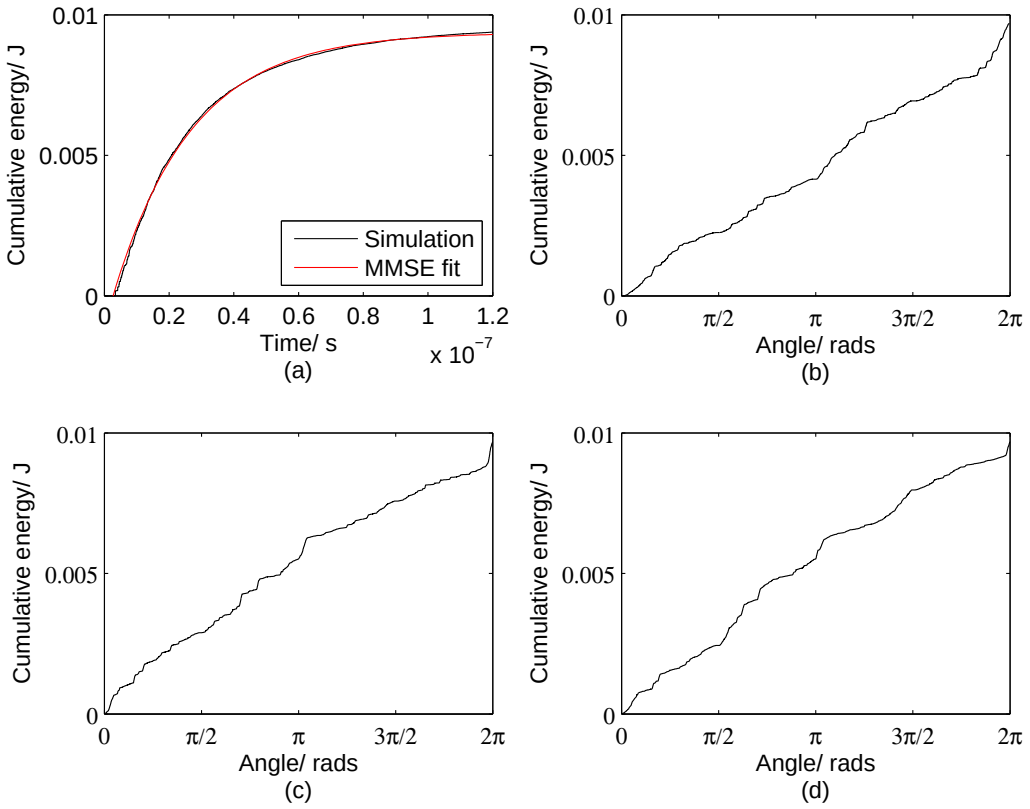

Figure 6.8: Propagation model with stirrer: (a) cumulative energy with time; (b) angular spread in the plane $z = 440$ mm; (c) angular spread in the plane $y = 490$ mm; (d) angular spread in the plane $x = 300$ mm

Table 6.5: Total arriving energy (J) with stirrer, for locations in the plane $x = 300$ mm.

		z **location**				
		413 mm	467 mm	525 mm	581 mm	637 mm
y **location**	328 mm	0.0092	0.0091	0.0093	0.0093	0.0096
	384 mm	0.0092	0.0094	0.0095	0.0096	0.0099
	440 mm	0.0096	0.0097	0.0099	0.0100	0.0101
	496 mm	0.0098	0.0100	0.0101	0.0100	0.0103
	552 mm	0.0100	0.0105	0.0106	0.0103	0.0104

All values are given to four decimal places to align the decimal point.

6.3 Chapter summary

The analogy between vehicle cavities and reverberation chambers has been investigated. Specifically the PDP of vehicle cavity channels, environment isolation and EF distribution uniformity have been measured and simulated for vehicle and vehicle-like cavities, and the results compared to the ideal reverberation chamber case. It has been shown, that for typical vehicle cavities, the PDP decays exponentially, with the same time constant for all links. Furthermore, the vehicle cavity can be treated as an isolated EM environment, and the EF distribution is not homogeneous, but may be isotropic.

To aid the deployment of communication systems in vehicles, a cavity classification method has been proposed. Vehicle cavities are typically Type II cavities, meaning that for all links in the cavity, the PDP is an exponential decay, with the same time constant. This means that the RMS delay spread, which is an important parameter for communications, is the same for all links in the cavity (and by extension, the coherence bandwidth, another important communications parameter is equal for all links in the cavity).

The Type II cavity classification is further divided into two sub-classes: Type IIA where at a point, the EF distribution is isotropic; and Type IIB where at a point, the EF distribution is not necessarily isotropic. In general, vehicle cavities can be either Type IIA or Type IIB cavities. It has been shown that for Type IIA cavities the spatial correlation is well defined over short distances, and thus MIMO antenna arrays should lead to enhanced performance. For Type IIB cavities, the non-uniformity in the angular spread should enable beamforming to lead to an enhanced performance.

Chapter 7

Deployment of an in-vehicle wireless communication system

Having characterised the propagation of Electromagnetic (EM) waves in cavities, the question remains: How can this characterisation be exploited to improve wireless communication systems deployed in vehicles? Specifically, it has been established in Chapter 6 that the Root Mean Square delay spread is approximately equal for all links in a given vehicle cavity, and is equal to the cavity time constant. Whether a typical in-vehicle wireless communication system can accurately estimate the cavity time constant is therefore investigated. Also, to what extent the characterisation of the time variation of a channel in a vehicle cavity, presented in Chapter 4 can be used to track the channel response is investigated.

For simplicity, the deployed system is Single Input Single Output and uses omnidirectional antennas (i.e., there is no beamforming). Furthermore the wireless network nodes transmit only on the *802.15.4* channels [74] (of which there are 16 in total) in the 2.4 GHz Industrial Scientific and Medical band (for example a *Zigbee* [62] based Wireless Sensor Network (WSN)).

7.1 Time constant estimation

Measurement Campaigns 1.7 and 1.8 are used to investigate time constant estimation in the van, and the car respectively. In these measurement campaigns, WSN style units are deployed at locations which are expected to be representative of an actual in-vehicle WSN (i.e., close to the cavity boundaries, in unobtrusive positions). Rather than attaching the unit antennas to actual WSN nodes, they are instead connected via co-axial cable to a vector network analyser. This approach enables the measurement of the complex channel frequency response.

Two methods of estimating the cavity time constant are proposed. The first uses only the magnitude of the complex channel frequency response, and when squared this corresponds to the Received Signal Strength Indicator (RSSI), which is available on most commercially available WSN nodes. The second method uses the complex channel frequency response.

7.1.1 Time constant estimation Method 1

In Chapter 4, the expected energy arriving a time τ after an impulse is given in (4.25), re-writing this for the total arriving energy (i.e., $\tau \to \infty$):

$$\begin{aligned} \mathbb{E}\left(\mathrm{E}_{\mathbb{H}}\right) &= k\tau_0 e^{-\frac{\tau_0}{\tau_c}} \\ \implies \log_e\left(\left(\mathbb{E}\left(\mathrm{E}_{\mathbb{H}}\right)\right)\right) &= \log_e(k\tau_0) - \frac{\tau_0}{\tau_c}. \end{aligned} \tag{7.1}$$

For a constant wave input, the term inside the logarithm on the left-hand side of (7.1) is proportional to the expected received power, which itself can be approximated by the average received power across the 16 frequency channels, $\langle \mathrm{P} \rangle$. This allows (7.1) to be re-written:

$$\log_e\langle \mathrm{P} \rangle \approx k' - \frac{\tau_0}{\tau_c}, \tag{7.2}$$

where k' is a constant.

If the separation between all the nodes is known, then τ_0 can be approximated by the time of flight of a ray travelling along the direct Line-of-Sight (LOS) path. Therefore plotting the logarithm of the average received power against the LOS time of flight for each link, and fitting a straight line using a Minimum Mean Squared Error (MMSE) method, the cavity time constant is approximately the negative inverse of the gradient.

Fig. 7.1 shows a plot of the time constant estimation by Method 1 for the car. The exponential decay (shown by the red line, labelled *Method 1 fit*) appears to fit the measured data reasonably

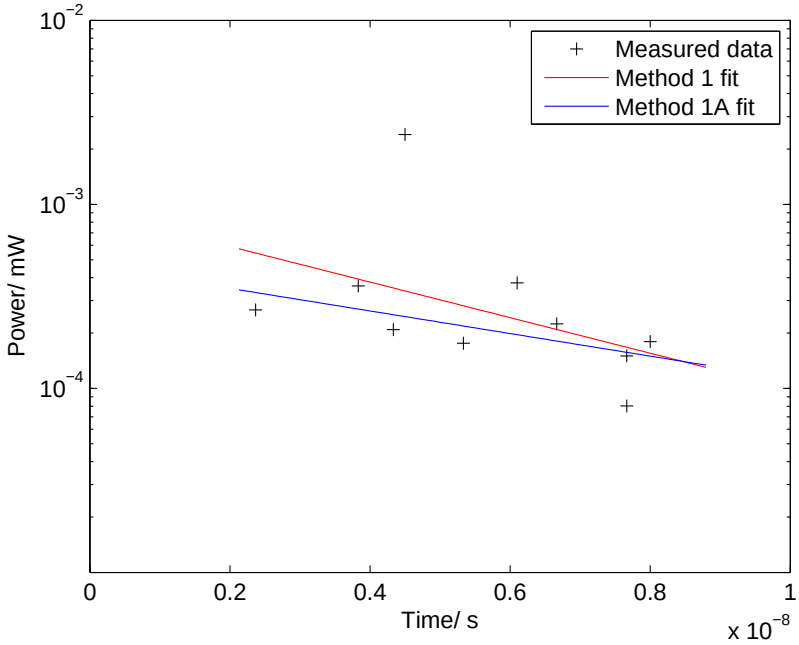

Figure 7.1: Time constant estimation for the car by Method 1 and Method 1A

well, with the exception of one anomaly (i.e., with power approximately equal to 2×10^{-3} mW). The variation in τ_0 is approximately 6 ns, with the time constant approximately 13.6 ns (from Chapter 6). Note that for the van, there was not sufficient difference in τ_0 for the various links to get meaningful results.

Time constant estimation Method 1A

Should higher level processing be available to identify and neglect clear anomalies (such as that in Fig. 7.1 with power approximately equal to $2 \times 10^{-}3$ mW), then an improved time constant estimate can be found, as detailed in Table 7.1. This is named Method 1A, and is also shown in Fig. 7.1.

7.1.2 Time constant estimation Method 2

The previous time constant estimation method provides an intuitive starting point. However, by being a little more specific about the statistical processes occurring, it is possible to find a method which uses the available information to find a time constant estimate that is in some sense optimal. Let the number of wireless links in the cavity equal n, and $\boldsymbol{z}_i$ be a row vector with elements giving the complex frequency response of the i^{th} link for each of the 16 frequency channels. The matrix Z can thus be defined: $Z = [\boldsymbol{z}_1; \boldsymbol{z}_2; ...\boldsymbol{z}_n]$.

Taking a Bayesian approach, the time constant can be estimated by finding the maximum *a posteriori* value, given the matrix of channel responses, $P(\tau_c|Z)$:

$$\begin{aligned} P(\tau_c|Z) &= \frac{P(Z|\tau_c)P(\tau_c)}{P(Z)} \\ &= P(Z|\tau_c), \end{aligned} \tag{7.3}$$

because a uniform prior is assumed, the maximum *a posteriori* estimate equals the maximum likelihood estimate.

The matrix of the channel frequency responses, Z, is a matrix of zero mean circularly symmetric Gaussian random variables, however its elements are not independent as there is frequency correlation. It is not trivial to see how the statistical propagation model enables the estimation of the joint likelihood of Z. However, by taking an Inverse Discrete Fourier Transform (IDFT) of $\boldsymbol{z}_i$ for each link, which is denoted $\mathbf{z}_i$ (i.e., not italicised), and thus working in the time domain, it is possible to estimate this joint distribution. This process can be thought of as instead of transforming the statistical model into the frequency domain, the vector of channel frequency responses is transformed into the time domain. It is important to note that as the IDFT is merely a deterministic operation, the maximum likelihood estimate (and likelihood value) will be the same as that which would be obtained if it were possible to estimate directly in the frequency domain.

Further expressing (7.3), assuming that the links are all mutually independent:

$$\begin{aligned} P(Z|\tau_c) &= \prod_{i=0}^{n-1} P(\boldsymbol{z}_i|\tau_c) \\ &= \prod_{i=0}^{n-1} P(\mathbf{z}_i|\tau_c). \end{aligned} \tag{7.4}$$

The vector $\mathbf{z}_i$ has 16 elements, shifting the first element of the impulse response to be centred on zero, the elements correspond to the complex sum of rays arriving in discrete time 'bins', each

of duration 12.5 ns (note that this is an approximation as the operation of the IDFT does not exactly correspond to discrete bins in the time domain). Vectors τ_- and τ_+ have been defined to represent the start and end of each of the 16 bins:

$$\begin{aligned}\tau_- = (&0; 6.25; 18.75; 31.25; 43.75; 56.25;\\ &68.75; 81.25; 93.75; 106.25; 118.75;\\ &131.25; 143.75; 156.25; 168.75; 181.25)\,\text{ns},\end{aligned} \tag{7.5}$$

$$\begin{aligned}\tau_+ = (&6.25; 18.75; 31.25; 43.75; 56.25; 68.75;\\ &81.25; 93.75; 106.25; 118.75; 131.25;\\ &143.75; 156.25; 168.75; 181.25; 193.75)\,\text{ns},\end{aligned} \tag{7.6}$$

strictly speaking the first bin should include the period from 193.75 ns to 200 ns, as the IDFT wraps around, however, this is neglected for simplicity.

The transmission frequency (2.4 GHz) is high compared to the frequency range, consequently it can be assumed that the arriving rays within a bin each have an independent random phase drawn from a uniform distribution. Thus, the magnitude of the sum of the arriving rays follows a Rayleigh distribution. This allows the maximum likelihood function to be further expressed:

$$P(\mathbf{z}_i|\tau_c) = \prod_{j=0}^{15} \mathcal{R}\left(\mathrm{z}_{i,j}; \sigma_j\right), \tag{7.7}$$

where $\mathcal{R}(.;\sigma)$ is the Rayleigh distribution with parameter σ, and:

$$\sigma_j = \sqrt{\frac{\Omega_j}{2}} + ((\tau_+)_j - (\tau_-)_j)\sigma_n, \tag{7.8}$$

where σ_n is noise, and:

$$\Omega_j = \begin{cases} \int_{\max((\tau_-)_j,\tau_0)}^{(\tau_+)_j} k e^{-\frac{\tau}{\tau_c}}\,\mathrm{d}\tau & \text{if } (\tau_+)_j > \tau_0 \\ 0 & \text{otherwise} \end{cases} \tag{7.9}$$

Thus (7.7) is a function of τ_c which is maximised to estimate τ_c. This approach can best be visualised by observing that the decay of each channel in space is identical, once the first ray has arrived. Fig. 7.2 shows the 6 links in the van, and it can be observed that the decay is indeed similar for each. Likewise, Fig. 7.3 shows the 10 links in the car, and again the decay is similar for each.

It should also be noted that after approximately 80 ns the signal reaches the noise floor, and therefore an additive white Gaussian noise term is included in the time constant estimate. Note the apparent rise at the end of the plot is an artefact of the IDFT, and that the IDFT processing distorts the values of power. However since it is the shape of the curve which is relevant, not its absolute value, this effect can be neglected.

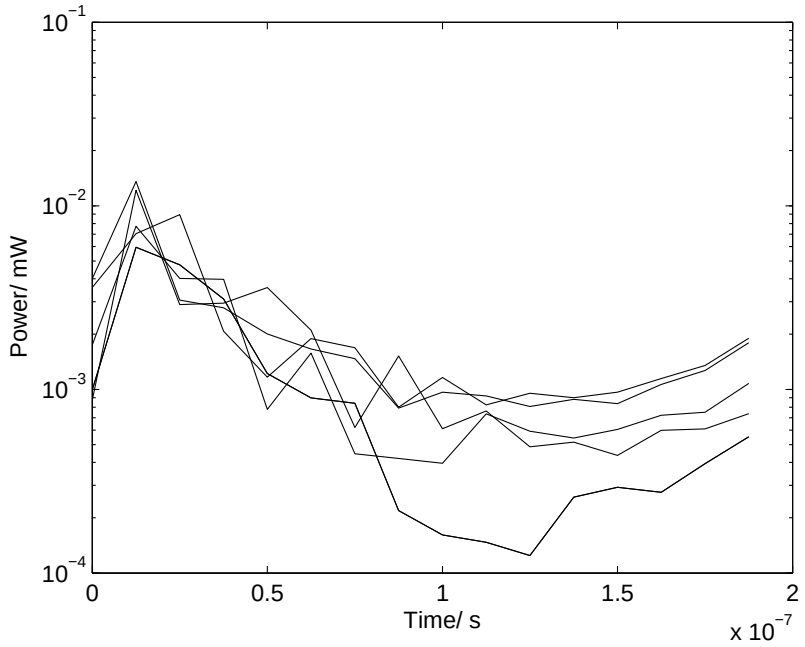

Figure 7.2: Time constant estimation for the various links in the van by Method 2

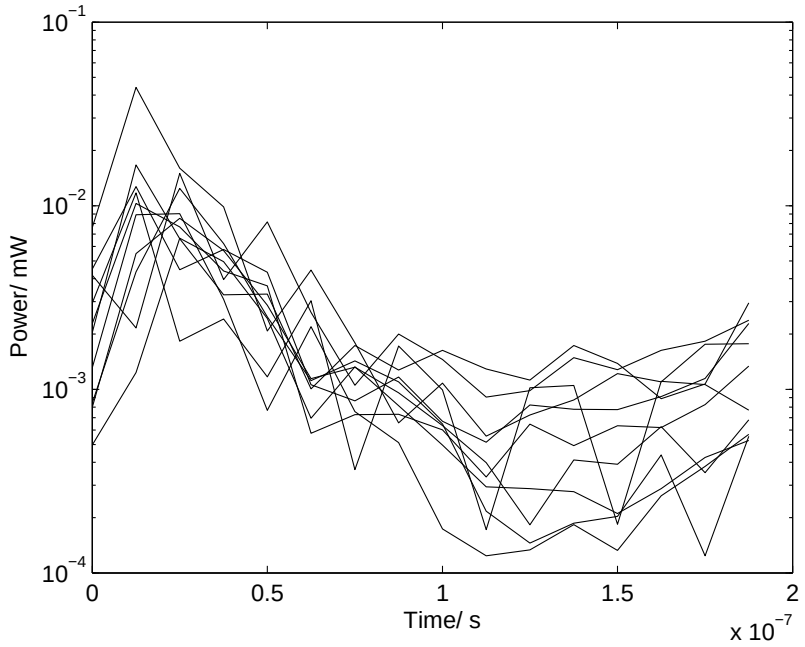

Figure 7.3: Time constant estimation for the various links in the car by Method 2

Table 7.1: Time constant estimation.

	$\langle\tau_c\rangle$ **/ ns**	τ_{c1} **/ ns**	$\tau_{c1\mathrm{A}}$ **/ ns**	τ_{c2} **/ ns**
Van	13.4	n/a	n/a	13.4
Car	13.6	4.49	7.08	11.7

7.1.3 Results and discussion

The time constant estimate from Chapter 6 is treated as the ground truth for the purposes of assessing the effectiveness of the time constant estimation methods presented in this chapter. This is because this estimate aggregated data for 6 different spatial configurations of the transmit and receive antennas, and measured the channel over a much broader frequency sweep (2 GHz) compared to that of the WSN system (80 MHz).

Table 7.1 shows the results of the time constant estimation by Methods 1, 1A and 2, denoted τ_{c1}, $\tau_{c1\mathrm{A}}$ and τ_{c2} respectively, as well as the average estimate from Chapter 6, denoted $\langle\tau_c\rangle$. As previously noted, Methods 1 and 1A were not possible for the van. It should also be noted that the van used previously in Chapter 6 was a slightly different model, however this appears to have little effect on the time constant.

Method 1 appears to estimate the time constant very poorly, however Method 1A offers some improvement. Furthermore, if the variation in τ_0 for the links was greater relative to the cavity time constant then it may be the case that the time constant estimate according to method 1 is much more accurate. Method 2 provides a good estimate for both the car and the van.

It can therefore be concluded, that if the complex channel frequency response is available, then Method 2 is the most accurate way to estimate the cavity time constant. However, in some circumstances Method 1 may work well, and in such cases it has the benefit of requiring only the magnitude of the channel response (available on most WSN from the RSSI value) which is not the case for Method 2. It should also be noted that, from the magnitude of the channel response alone, the envelope correlation function can be found, which will be the same for all the links (i.e., because this is a deterministic function of the power delay profile). For some systems this parameter may be all that is required, and thus it is unnecessary to evaluate an estimate of the time constant.

7.2 Time variation estimation

As well as estimating the cavity time constant, it is also useful to track and estimate the time variation of channels within the cavity. To do this, the time varying frequency response of the channel, $T_{\mathbb{H}}(f,t)$, is measured at regular time intervals, at a single frequency, f_0. This process was undertaken in Measurement Campaign 3, where the time varying frequency response was measured every 0.125 s at 2.45 GHz. Measurement Campaigns 3a and 3b refer to the measurements with the receiver at locations $\mathrm{P}_{\mathrm{Car}\,1}$ and $\mathrm{P}_{\mathrm{Car}\,4}$ respectively. Figs. 7.4 and 7.5 show the raw data for Measurement Campaigns 3a and 3b respectively, note that in Measurement Campaign 3a there was a problem with the experiment which led to later samples not being recorded (hence why the plot in Fig. 7.4 shows the results for a shorter time duration than Fig. 7.5).

Whether the channel analysis can lead to an improved prediction of the channel at the next time instant, compared to a simple predictor where the channel is estimated as if the magnitude of each time sample is an Independent Identically Distributed (IID) Rician random variable is investigated. The Rician case arises as it is known that the Electric Field (EF) consists of the sum of an unstirred (deterministic) EF, and a stirred EF which in general can be considered to have a zero mean, circularly symmetric complex Gaussian distribution. Further evidence that the Rician distribution is appropriate can be observed in Figs. 7.6 and 7.7 for Measurement Campaigns 3a and 3b respectively. These plots show the distribution of all the received channel samples, and although the actual measurements are discretised (i.e., owing to the RSSI process only logging the power to 1dBm), it appears that the Rician generally fits the data well.

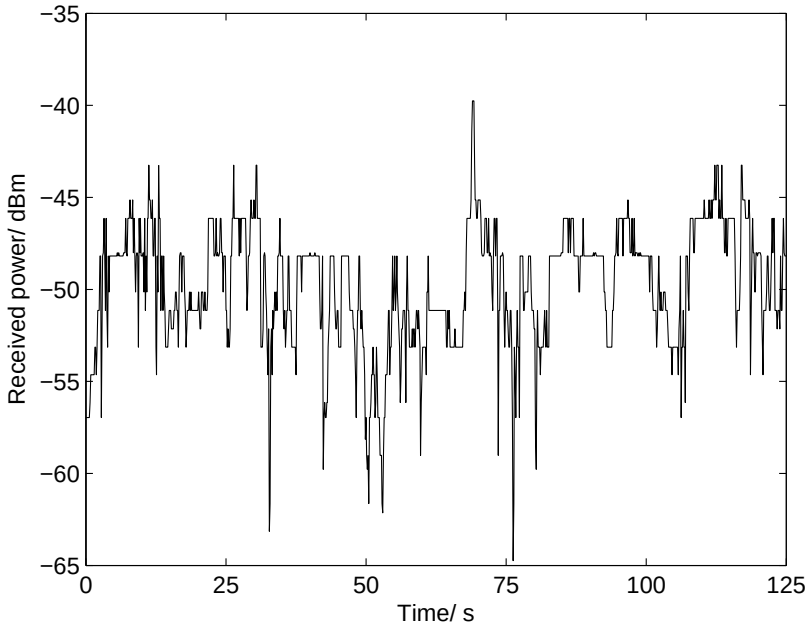

Figure 7.4: Measurement Campaign 3a raw data

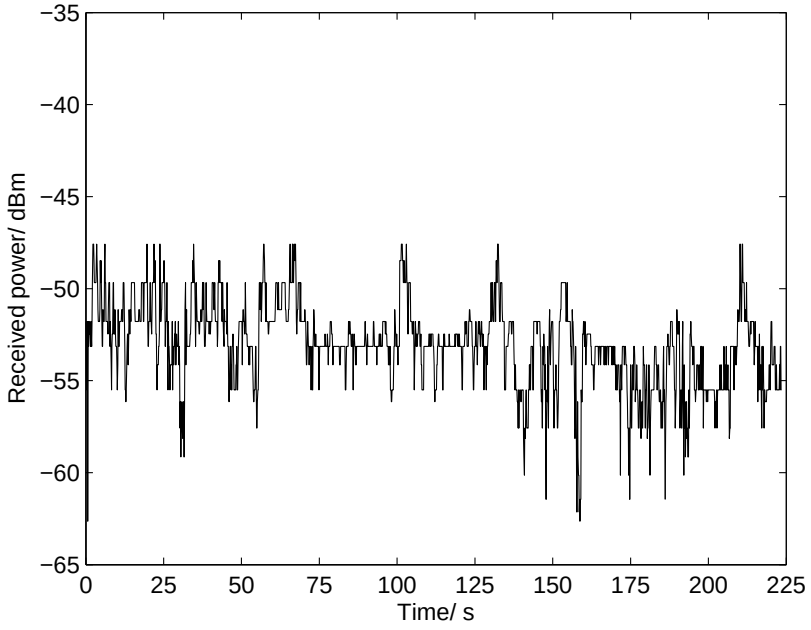

Figure 7.5: Measurement Campaign 3b raw data

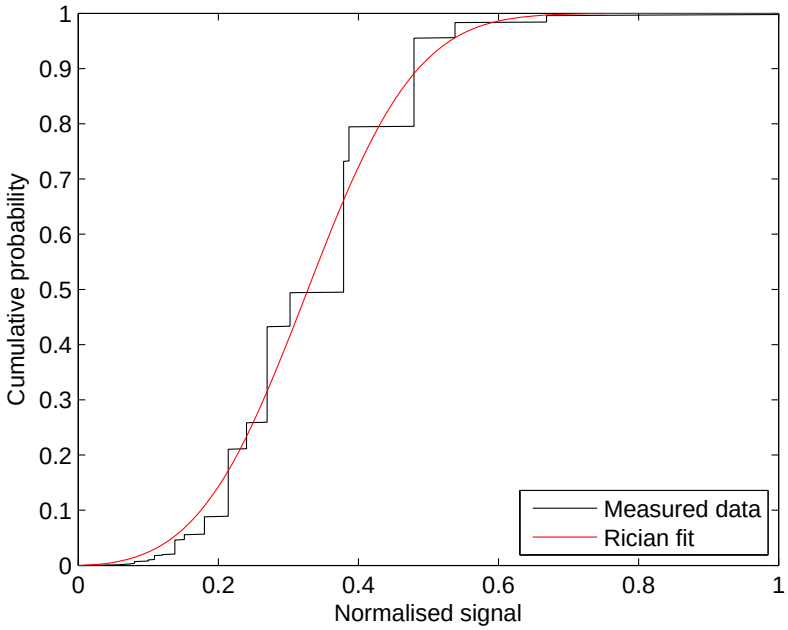

Figure 7.6: Measurement Campaign 3a Rician fit

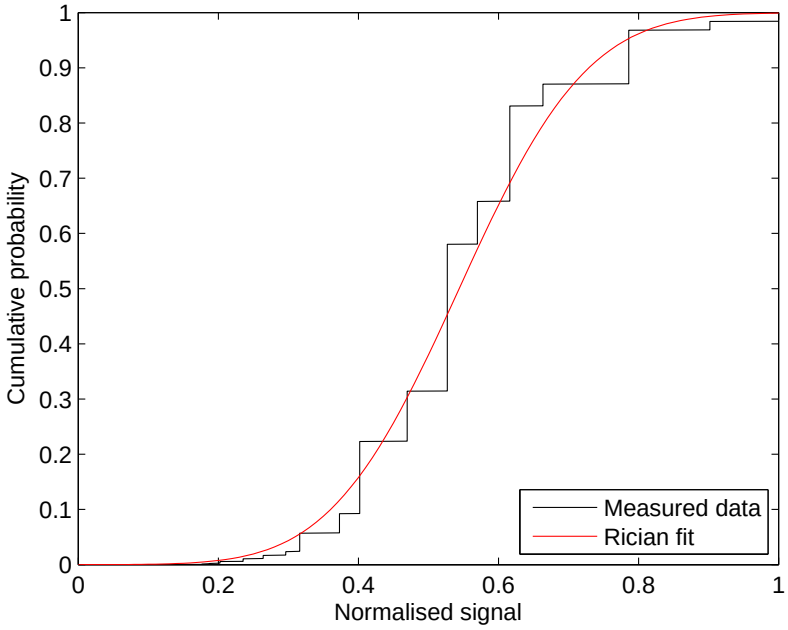

Figure 7.7: Measurement Campaign 3b Rician fit

7.2.1 A heuristic model for time variation

Let Δt be the time between successive samples, and $\mathbf{z}'$ be a vector of the time varying frequency responses at 2.45 GHz, with the first element z'_0 occurring at $t = 0$ (the dash has been included to avoid ambiguity with the previous use of z in Section 7.1). Assumptions 3 – 6 stated in Section 4.2.1 continue to be made, and in addition:

Assumption 7: The process is Markov for all Δt, therefore:

$$P(\mathrm{z}'_i|\mathrm{z}'_{i-1}, ...\mathrm{z}'_0) = P(\mathrm{z}'_i|\mathrm{z}'_{i-1}). \tag{7.10}$$

The Markov assumption has been made heuristically, it has a specific purpose to serve (in this case to enable enhanced estimation of the channel time varying frequency response) rather than to necessarily reflect an absolute truth regarding the underlying process. In such a case it is valid merely to estimate the value of the channel time varying frequency response from that immediately preceding it alone, even if there is dependence on other previous values. There is, however, some physical basis for why the Markov assumption may be valid in general. Consider the case where a random process is not Markov, in such an instance there is some smooth evolution of successive states. The Markov assumption can therefore be reasoned physically for the vehicle cavity by noting that in general the cavity occupants do not move in a smooth way. Furthermore, the mode pattern within a cavity is chaotic, and therefore even motion which is fleetingly smooth will not necessarily correspond to a smooth variation in the channel response.

These assumptions (i.e., 3 – 7) are consistent with modelling the sampled time series as a first order autoregressive (AR1) process:

$$\mathrm{z}'_i = B(\mathrm{z}'_{i-1} - \mu) + \epsilon_i + \mu, \tag{7.11}$$

where B is real, between zero and one, ϵ_n is an independent Gaussian random variable and μ is the process mean. Noting that in general Δt is arbitrary, if the sampled process really is an AR1 process, then the underlying continuous time process must be an Ornstein-Uhlenbeck process [102], which has Autocorrelation Co-efficient (ACC):

$$\mathbb{E}((\mathrm{z}'_i - \mu)(\mathrm{z}'_{i-1} - \mu)) = \sigma^2 e^{-\theta|\Delta t|}, \tag{7.12}$$

where σ^2 is the process variance and θ is a constant, therefore from (7.11), $B = e^{-\theta\Delta t}$.

Verifying for the measurements, that B does indeed approximately equal $e^{-\theta|\Delta t|}$ would provide some evidence that the assumptions are valid. It is, however, not possible to estimate the ACC

directly (and therefore verify the exponential shape) from the measurements, as only the magnitude is available. A slightly more sophisticated approach is therefore taken, using (7.11) as a starting point:

$$\begin{aligned}|\mathrm{z}'_i|^2 &= |B(\mathrm{z}'_{i-1} - \mu) + \epsilon_i + \mu|^2 \\ &= (B\mathrm{Re}(\mathrm{z}'_{i-1}) + (1-B)\mathrm{Re}(\mu) + \mathrm{Re}(\epsilon_i))^2 \\ &\quad +(B\mathrm{Im}(\mathrm{z}'_{i-1}) + (1-B)\mathrm{Im}(\mu) + \mathrm{Im}(\epsilon_i))^2. \end{aligned} \tag{7.13}$$

From (7.13), it can be shown:

$$\begin{aligned}\mathbb{E}(|\mathrm{z}'_i|^2|\mathrm{z}'_{i-1}|^2) &= \alpha B^2 + \beta B + \gamma \\ &= \alpha e^{-2\theta|\Delta t|}\sigma^4 + \beta e^{-\theta|\Delta t|}\sigma^2 + \gamma \\ &= \alpha' e^{-2\theta|\Delta t|} + \beta' e^{-\theta|\Delta t|} + \gamma, \end{aligned} \tag{7.14}$$

where α, β, and γ are constants that depend on $\mathrm{Re}(\mu)$, $\mathrm{Im}(\mu)$, $\mathrm{Re}(\mu)\mathrm{Im}(\mu)$, $\mathbb{E}(\epsilon^2)$, $\mathbb{E}(\mathrm{Re}(\mu)^2)$, $\mathbb{E}(\mathrm{Im}(\mu)^2)$ and $\mathbb{E}(\mathrm{Re}(\mu)\mathrm{Im}(\mu))$. To simplify the notation α' and β' are introduced.

The term $\mathbb{E}(|\mathrm{z}'_i|^2|\mathrm{z}'_{i-1}|^2)$ is approximated by $\langle|\mathrm{z}'_i|^2|\mathrm{z}'_{i-1}|^2\rangle$ (where $\langle.\rangle$ denotes the average over the measured data), and this is used to find a MMSE fit for the parameters α', β', γ and θ. Figs. 7.8 and 7.9 show that the proposed model fits reasonably well with the measured data for Measurement Campaigns 3a and 3b respectively. Previous work has estimated the coherence time of the in-vehicle channel as 1 – 10 s [36, 37], and Figs. 7.8 and 7.9 show that this is consistent with the measurements in Measurement Campaigns 3a and 3b. Figs. 7.8 and 7.9 also show a line of best fit according to (7.14) which appears to be good. It should, however, be noted that whilst the observed fit is encouraging, (7.14) is a quadratic and thus has three independent degrees of freedom, and therefore this alone does not constitute unequivocal evidence that the underlying process has been found.

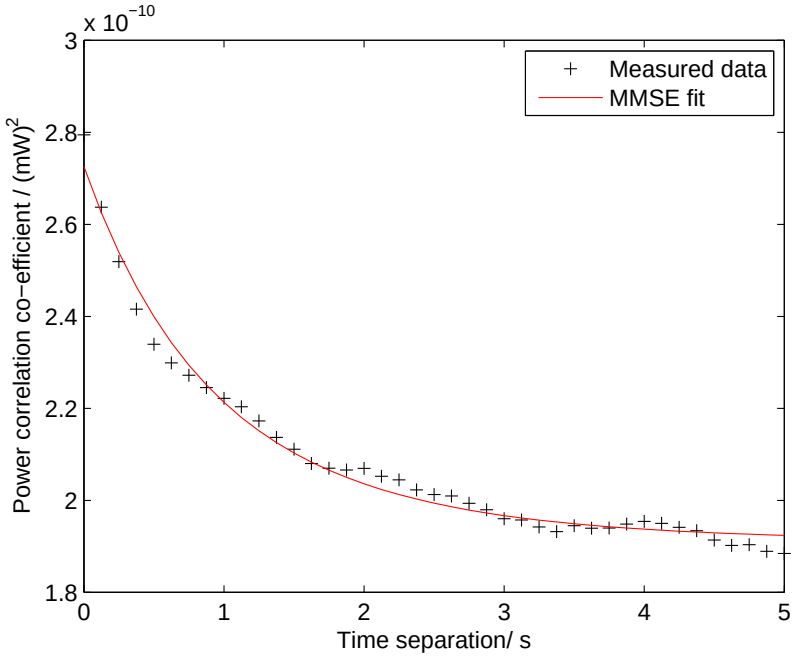

Figure 7.8: Power correlation function for Measurement Campaign 3a (not normalised)

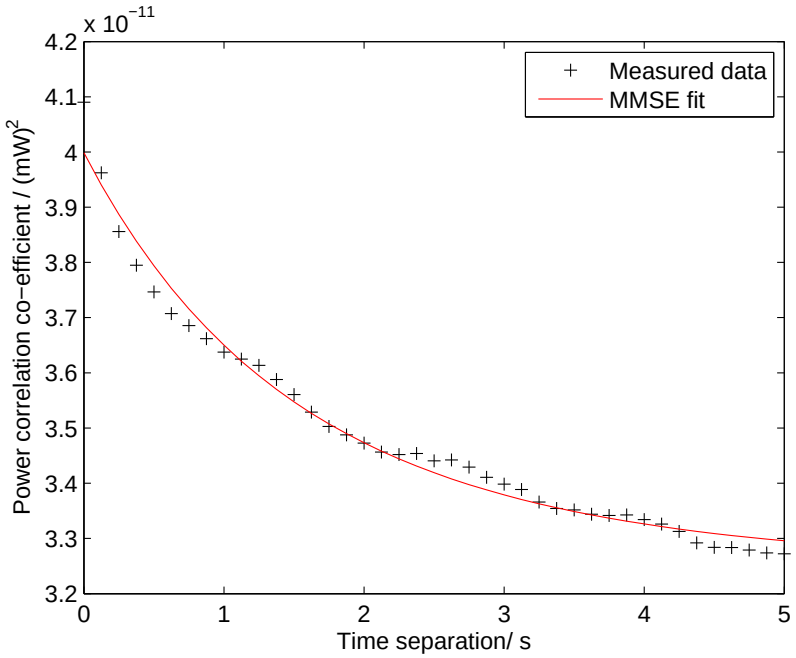

Figure 7.9: Power correlation function for Measurement Campaign 3b (not normalised)

7.2.2 Results and discussion

Having established that the Ornstein-Uhlenbeck model appears to be a good fit for the underlying process, but that the evidence from the ACC alone is not totally compelling, it is interesting to ask whether any real benefits can be achieved by modelling the time variation in this way. To do this, consider a prediction of the received power at the next discrete time sample according to the proposed model, compared to a simple IID Rician predictor. As a starting point, (7.13) is expressed in a slightly different way:

$$|z_i'|^2 = B^2|z_{i-1}'|^2 + (1-B)^2|\mu|^2 + \epsilon_i', \tag{7.15}$$

where ϵ_i' incorporates all of the other terms. In general, ϵ_i' is a random term, however it is not Gaussian, and not independent of $B^2|z_{i-1}'|^2 + (1-B)^2|\mu|^2$. However, if ϵ_i' were to be treated as a series of IID Gaussian random variables, it can be seen that (7.15) is in the form of an AR1 process. Figs. 7.10 and 7.11 show that for Measurement Campaigns 3a and 3b respectively, the AR1 model does indeed lead to an improved (i.e., reduced variance) estimate of the channel compared to a simple Rician predictor.

In Fig. 7.11 it can be seen that after approximately 70 s there appears to have been a step shift in received power. This is an example of the fact that the process is actually quasi-Wide-sense Stationary Uncorrelated Scattering (WSSUS) [16] not WSSUS, and the channel estimation/ prediction can be improved by introducing a forgetting factor or finite window length (i.e., to use as a sample to estimate the parameters). Furthermore at approximately 70 s in Fig. 7.10 there is a large spike in received power, and neither the AR1 nor the Rician model can anticipate this. This is evidence that there is always the possibility that something can happen which cannot be forecast statistically, and in such cases it may be necessary to mitigate any adverse effects of such an eventuality at a higher level (for example by re-sending packets, if a sudden unexpected dip in received power occurs).

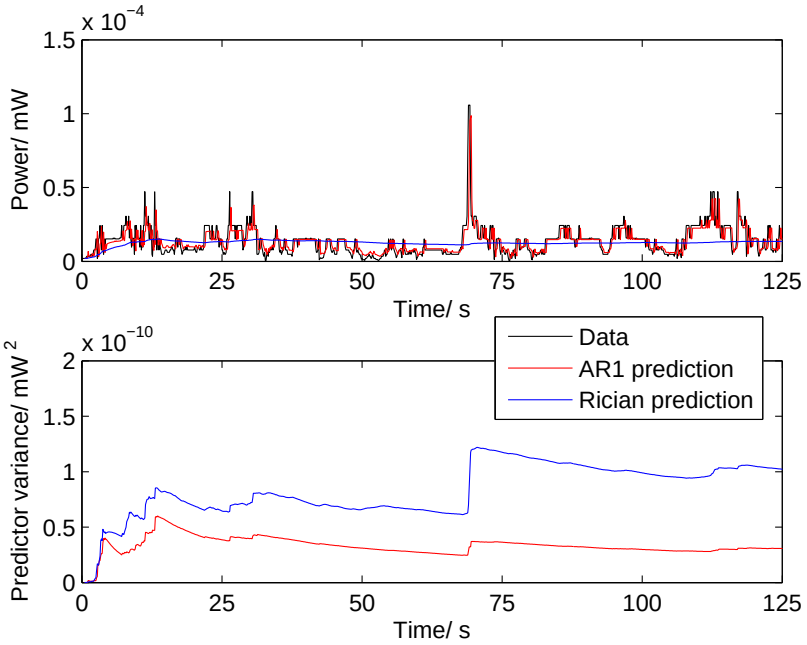

Figure 7.10: Prediction of received power for Measurement Campaign 3a

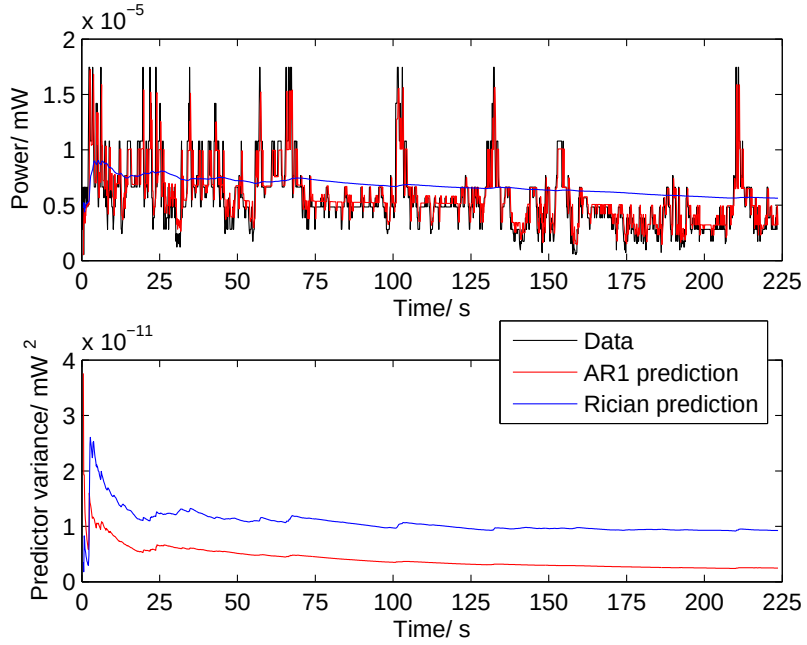

Figure 7.11: Prediction of received power for Measurement Campaign 3b

7.3 Chapter Summary

Having characterised the fundamental properties of the EM wave propagation environment in Chapters 4 – 6, it is important to investigate whether this can lead to actual improvements in the performance of in-vehicle wireless communication systems. The approach taken is to assess to what extent a typical in-vehicle wireless communication system can estimate the parameters of the wireless channel. If these can be estimated accurately, then it is reasoned that a wireless communication system can use this Channel State Information (CSI) to improve the information transfer.

It has been shown that, if the channel frequency response is available in complex form, then a typical in-vehicle WSN can accurately estimate the cavity time constant. If only the magnitude of the frequency response is available (i.e., corresponding to RSSI values) then there is some evidence that accurate cavity time constant estimation is possible under certain circumstances. Estimating the cavity time constant is important as it can be used to find the delay spread and coherence times of channels in the cavity, parameters which are very important for the deployment of effective in-vehicle wireless communication systems.

Furthermore, by making the assumption that the channel time varying frequency response evolves in time as a Markov process (i.e., for any given frequency), it has been shown that the time variation of the channel at discrete time intervals can be predicted with much greater accuracy compared to the simple case where each discrete time sample is treated as independent. This is important for the deployment of effective in-vehicle wireless communication systems, as it provides enhanced CSI at the receiver. Furthermore, this information could be fed back to provide transmitter CSI, or indeed in some network architectures fed to a central control unit to make improved decisions regarding resource allocation to a number of wireless links.

Chapter 8

Conclusions

This dissertation presents a fundamental characterisation of Electromagnetic (EM) wave propagation in vehicle cavities, a detailed investigation into the analogy between vehicle cavities and reverberation chambers, and an example of how this analysis can lead to improvements in the performance of wireless communication systems deployed in vehicles. Specifically, the fundamental characterisation consists of an impulse response model, an upper bound on the Doppler spread, and a lower bound on the information capacity of a wireless communication channel given the impulse response model and Doppler spread bound.

The impulse response model is expressed in terms of a ray arrival process (for an instantaneous realisation of the channel), and is derived from the assumption that all rays are independent. The resulting theoretical model is supported by measurements performed in a vehicle-like cavity. It is shown that, for all but impractically large bandwidths, the Power Delay Profile (PDP) of a wireless link in an EM cavity decays exponentially. This is consistent with a wealth of previous literature.

The Doppler spread characterisation is expressed in terms of an upper bound on the Power Spectral Density (PSD). It is derived from four assumptions, which essentially amount to assuming that the channel monotonically does not become more correlated with time. This theoretical model is supported by measurements taken for a range of channel variation types, in both the vehicle-like cavity used for the impulse response measurements and in an actual vehicle. Measurements were also undertaken for a range of transmission frequencies and a range of cavity loading scenarios. It was found that the Doppler spread increases with frequency, however there is only a minor variation in the Doppler spread as the cavity loading varies (which takes the form of a small decrease in Doppler spread with loading).

Measurements of PDP and PSD indicate that typically the in-vehicle channel is underspread (to a very good approximation), i.e., its delay spread is smaller than its coherence time. For such channels, in the infinite bandwidth limit, the information capacity approaches that of the same channel with perfect Channel State Information (CSI) at the receiver. The fact that channels in vehicle cavities are not just underspread, but are typically highly underspread has been exploited to derive a lower bound on the information capacity for finite values of bandwidth. The bounding method expresses the channel input as symbols in the frequency domain, and applies a *Kalman* filter to use the frequency correlation to learn the channel state. This results in a mathematically elegant and computationally simple bound. For the measured values of PDP and PSD it is shown that the lower bound on the information capacity is indeed very close to the capacity of the same channel with perfect CSI at the receiver.

That the EM environment in vehicle cavities is analogous to that in reverberation chambers is often assumed implicitly. To establish the extent to which this is valid, a detailed investigation into the analogy between vehicle cavities and reverberation chambers has been undertaken. Noting that the characterisation of the impulse response of the in-vehicle channel yields the result that the PDP decays exponentially, as is the case for channels in reverberation chambers, three specific reverberation chamber properties are investigated. Whether, in any given vehicle cavity, the time constant of the exponentially decaying PDP is the same for all possible links, whether the vehicle cavity is an isolated EM environment, and whether the Electric Field (EF) distribution is *uniform* (i.e., isotropic and homogeneous). The results of this investigation are that, for typical vehicle cavities, the time constant of the exponentially decaying PDP is approximately the same for all possible links, the EM environment can be modelled as isolated with an increased noise floor (to allow for the propagation into the cavity of EM waves from external sources) and that the EF distribution is sometimes approximately isotropic, but not homogeneous. These results lead to two properties which are potentially important for wireless communications systems, namely that, in any given cavity, the Root Mean Square (RMS) delay spread is approximately the same for all links (and hence the coherence bandwidth is also the same for all links) and that the angular spread is approximately uniform. Furthermore, whilst it has been shown that the EF distribution is not globally homogeneous, it does appear to vary continuously for vehicle cavities with isotropic EF distributions (and thus is approximately locally homogeneous), which means that over short distances the spatial correlation is well defined. This is potentially very useful for designers of Multiple Input Multiple Output antenna arrays to be deployed in wireless communication systems in vehicles. For cavities which don't have an isotropic EF distribution, it is anticipated that beamforming may work well.

The fact that, for typical vehicle cavities, the RMS delay spread is approximately the same for all links is potentially very beneficial for wireless communication systems (for example, even

before a link is turned on its coherence bandwidth is available if it has been estimated for other links, and thus frequency diversity can be used in an efficient way immediately). This property can only be exploited, however, if channel state estimation is possible from information typically available to wireless communication systems. To this end, it is shown that if the complex channel response is available on 16 frequency channels at intervals of 5 MHz (i.e., as is the case for the *802.15.4* physical layer [74]) then the time constant of the exponentially decaying PDP can be estimated accurately. Not only is time constant estimation possible, but by making the further assumption that successive channel realisations (in time) form a Markov process, it has been shown that estimation of the time variation of the channel is also possible by typical wireless communication systems.

These elements unite to form a thesis which addresses all of the main issues required to deploy effective wireless communication systems in vehicles. It is therefore envisaged that the major application of this work will be to aid the deployment of wireless communication systems in vehicles. The analysis presented in this dissertation is, however, somewhat general, and there is potential for impact further afield. Specifically, the theoretical modelling of the EM wave propagation has been derived such that it applies to all EM cavities, the lower bound on the information capacity can be applied to any highly underspread channel with known PDP and coherence time, and the results from the investigation into the analogy between vehicle cavities and reverberation chambers may also apply to heavily loaded reverberation chambers. To set this thesis in a more general context, a certain amount of further work is therefore required:

I. Perform measurements in a wider range of EM cavities, to investigate whether the theoretical characterisation presented here is valid.

II. For a much larger cavity, or a much wider frequency band, it may be the case that individual rays are resolvable and thus the τ^{-2} term in the impulse response (in (4.23)) becomes relevant. In such instances it would be useful to have experimental evidence to support the theoretical characterisation.

It is also possible, for given cavity types and applications, to make more specific assumptions regarding the channel variation which can be used to tighten the PSD bound, or indeed express the channel time variation itself as a function.

Appendix A

Antenna efficiencies

The efficiency has been measured for the three types of antennas used in the measurements. For the Schwarzbeck 9112 (SB9112) [68] and Schwarzbeck 9113 (SB9113) [69] antennas, the reflection efficiency is also given. For the low-profile printed patch-type antennas the efficiency has been measured for each individual unit. The total efficiency for the SB9113 antenna has previously been measured at the National Physical Laboratory (NPL) [103], and it is this measurement which is included here [1].

[1] It has since come to light that the value used as the total efficiency of the SB9113 antenna is actually the radiation efficiency, and thus the total efficiency should have been adjusted accordingly. All the analysis affected by this error in this dissertation has been repeated with the correct total efficiency and it was found that the difference compared to the analysis with the incorrect total efficiency used in this dissertation is negligible.

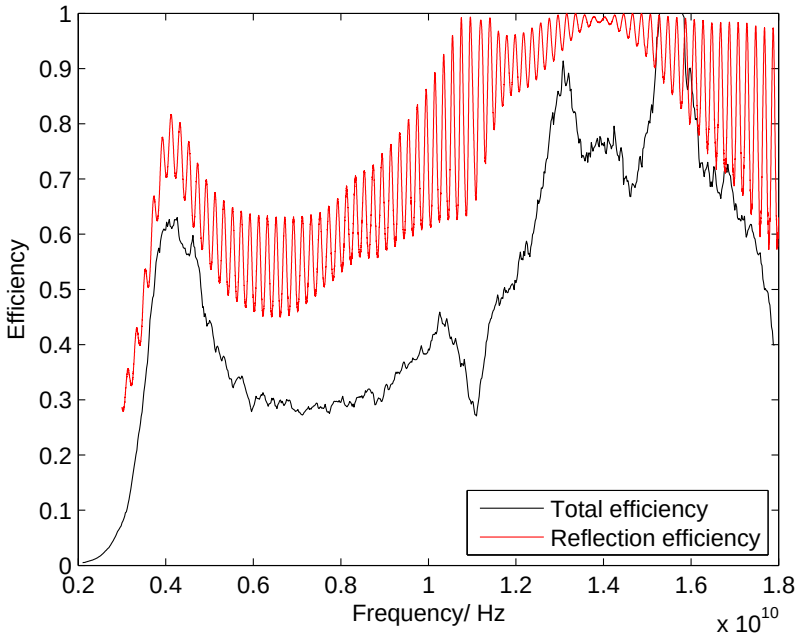

Figure A.1: Schwarzbeck 9112 efficiency

Note that due to a measurement error, at high efficiencies it is occasionally the case that the total efficiency value appears higher than the reflection efficiency value for the SB9112 antenna. This has no untoward effect on the results presented in this dissertation.

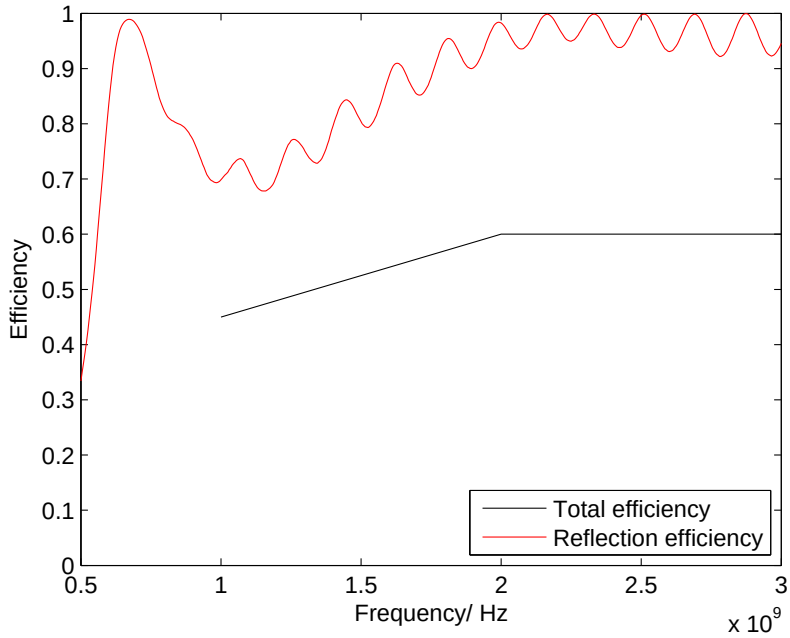

Figure A.2: Schwarzbeck 9113 efficiency

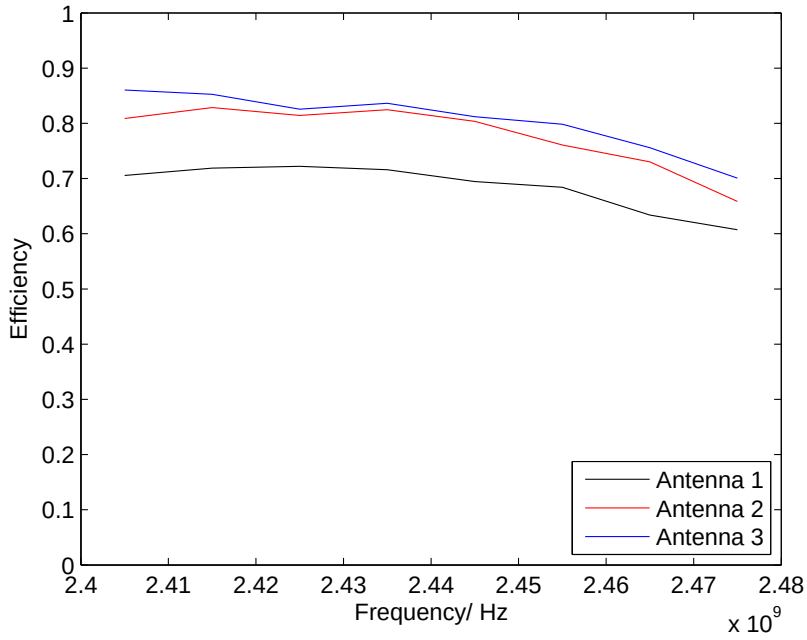

Figure A.3: Patch antenna efficiencies

Appendix B

MICAz calibration

For the units 1, 2, and 3 calibration has been undertaken for each unit permutation (i.e., Transmitter (Tx) 1, Receiver (Rx) 2; Tx1, Rx3; Tx2, Rx1; Tx2, Rx3; Tx3, Rx1; and Tx3, Rx2), and for each of the 16 frequency channels. Fig. B.1 shows the result at 2.45 GHz (the only frequency channel used by the measurements presented in this dissertation). This plot is the specific realisations of that shown in the manufacturers datasheet, [[104] Fig. 26].

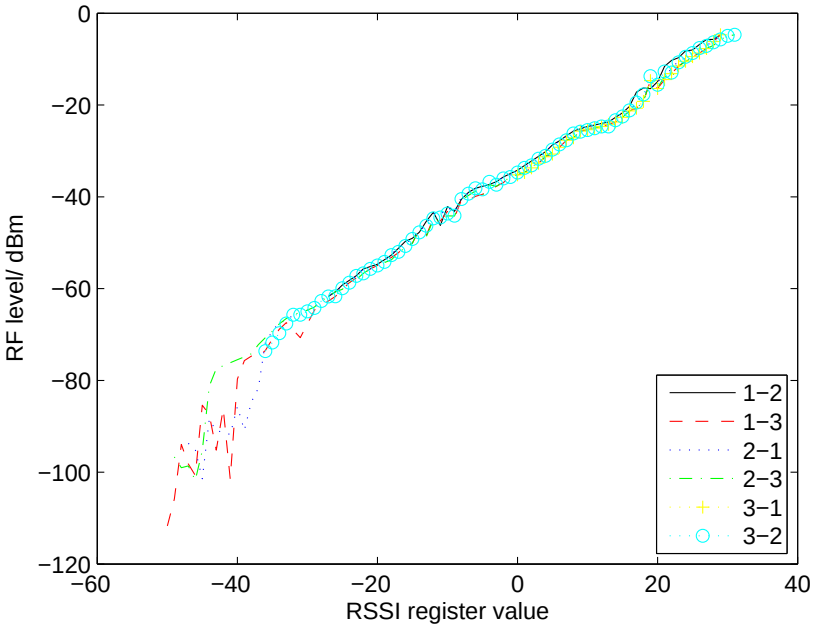

Figure B.1: RSSI calibration for frequency channel 10 (2.45 GHz)

Appendix C

Lemmas

The Lemma's included in this Appendix are for very simple algebraic results concerning matrices. They are used in the information theoretic analysis presented in Chapter 5.

Lemma 5.5

For identity matrix, I, and Positive Definite Symmetric (PDS) matrix D, there exists a PDS matrix D' such that:

$$(I - D)^{-1} = I + D'. \tag{C.1}$$

Proof:

From [[105] pp. 151]:

$$(I - D)^{-1} = I + (I - D)^{-1}D. \tag{C.2}$$

Given that $(I - D)$ is a PDS matrix, $(I - D)^{-1}$ is also a PDS matrix. Also, since D is a PDS matrix, then $(I - D)^{-1}D$ must be a PDS matrix, which is renamed D' to prove Lemma 5.5.

Lemma 5.6

For identity matrix, I, and PDS matrix D, there exists a PDS matrix D' such that:

$$(I + D)^{-1} = I - D'. \tag{C.3}$$

Proof:

From [[105] pp. 151]:

$$(I + D)^{-1} = I - (I + D)^{-1}D. \tag{C.4}$$

Given that $(I + D)$ is a PDS matrix, $(I + D)^{-1}$ is also a PDS matrix. Also, since D is a PDS matrix, then $(I + D)^{-1}D$ must be a PDS matrix, which is renamed D' to prove Lemma 5.6.

Lemma 5.7

For 2×2 identity matrix, I, and 2×2 PDS matrix, D, with $(I - D)$ also a 2×2 PDS matrix, it follows that:

$$|I - D| < 1. \tag{C.5}$$

Proof:

Let:

$$D = \begin{bmatrix} d_1 & d_2 \\ d_2 & d_4 \end{bmatrix}, \tag{C.6}$$

therefore:

$$\begin{aligned} |I - D| &= (1 - d_1)(1 - d_4) - d_2^2 \\ &= 1 - d_1 - d_4 + d_1 d_4 - d_2^2, \end{aligned} \tag{C.7}$$

consider $0 < d_1, d_4 < 1$, therefore:

$$d_1, d_4 > d_1 d_4 \tag{C.8}$$

$$\begin{aligned} \implies \quad 1 &> 1 - d_1 - d_4 + d_1 d_4 - d_2^2 \\ &= |I - D|, \end{aligned} \tag{C.9}$$

thus proving Lemma 5.7.

Bibliography

[1] S. A. (Reza) Zekavat, "A novel application for wireless communications in vehicle early warning," in *Consumer Communications and Networking Conference, 2004. CCNC 2004. First IEEE*, 2004, pp. 715–717.

[2] S. Mahmud and S. Shanker, "In-vehicle secure wireless personal area network (SW-PAN)," *Vehicular Technology, IEEE Transactions on*, vol. 55, no. 3, pp. 1051–1061, 2006.

[3] Q. Li, Y. Andreopoulos, and M. van der Schaar, "Streaming-viability analysis and packet scheduling for video over in-vehicle wireless networks," *Vehicular Technology, IEEE Transactions on*, vol. 56, no. 6, pp. 3533–3549, 2007.

[4] M. Rahmani, M. Pfannenstein, E. Steinbach, G. Giordano, and E. Biersack, "Wireless media streaming over IP-based in-vehicle networks," in *Communications Workshops, 2009. ICC Workshops 2009. IEEE International Conference on*, 2009, pp. 1–6.

[5] O. Siordia, I. de Diego, C. Conde, and E. Cabello, "Wireless in-vehicle compliant black box: For accident analysis," *Vehicular Technology Magazine, IEEE*, vol. 7, no. 3, pp. 80–89, 2012.

[6] H. Hu and Z.-K. Xie, "Framework of in-vehicle information management based on multi-agent in mobile wireless environments," in *Machine Learning and Cybernetics, 2009 International Conference on*, vol. 5, 2009, pp. 3083–3088.

[7] J. Poroor, S. Karunagaran, S. Sundararajan, and R. Pillai, "Fast dual-radio cross-layer handoffs in multi-hop infrastructure-mode 802.11 wireless networks for in-vehicle multimedia infotainment," in *Advanced Networks and Telecommunication Systems, 2008. ANTS '08. 2nd International Symposium on*, 2008, pp. 1–3.

[8] D. Hintea, J. Brusey, E. Gaura, N. Beloe, and D. Bridge, "Mutual information-based sensor positioning for car cabin comfort control," in *Knowledge-Based and Intelligent Information and Engineering Systems*, ser. Lecture Notes in Computer Science, A. Knig, A. Dengel, K. Hinkelmann, K. Kise, R. Howlett, and L. Jain, Eds.

Springer Berlin Heidelberg, 2011, vol. 6883, pp. 483–492. [Online]. Available: http://dx.doi.org/10.1007/978-3-642-23854-3_51

[9] J. Dawson, D. Hope, M. Panitz, and C. Christopoulos, "Wireless networks in vehicles," in *Electromagnetic Propagation in Structures and Buildings, 2008 IET Seminar on*, 2008, pp. 1–6.

[10] M. Heddebaut, V. Deniau, and K. Adouane, "In-vehicle WLAN radio-frequency communication characterization," *Intelligent Transportation Systems, IEEE Transactions on*, vol. 5, no. 2, pp. 114–121, 2004.

[11] G. Leen and D. Heffernan, "Vehicles without wires," *Computing Control Engineering Journal*, vol. 12, no. 5, pp. 205–211, 2001.

[12] J.-S. Byun, W.-S. Shim, and W.-K. Hong, "WSN-based intelligent telematics system," in *Engineering of Computer Based Systems, 2006. ECBS 2006. 13th Annual IEEE International Symposium and Workshop on*, 2006, p. 2.

[13] T. ElBatt, C. Saraydar, M. Ames, and T. Talty, "Potential for intra-vehicle wireless automotive sensor networks," in *Sarnoff Symposium, 2006 IEEE*, 2006, pp. 1–4.

[14] J. Tavares, F. Velez, and J. Ferro, "Application of wireless sensor networks to automobiles," vol. 8, no. 6, 2008.

[15] D. Balachander, T. R. Rao, and N. Tiwari, "In-vehicle RF propagation measurements for wireless sensor networks at 433/868/915/2400MHz," in *Communications and Signal Processing (ICCSP), 2013 International Conference on*, 2013, pp. 419–422.

[16] P. Bello, "Characterization of randomly time-variant linear channels," *Communications Systems, IEEE Transactions on*, vol. 11, no. 4, pp. 360–393, 1963.

[17] "IEC 61000-4-21 standard." [Online]. Available: http://webstore.iec.ch/webstore/webstore.nsf/ArtNum_PK/44777?OpenDocument

[18] D. Hill, *Electromagnetic Fields in Cavities (Deterministic and Statistical Theories)*, 2009.

[19] O. Delangre, S. Van Roy, P. De Doncker, M. Lienard, and P. Degauque, "Modeling in-vehicle wideband wireless channels using reverberation chamber theory," in *Vehicular Technology Conference, 2007. VTC-2007 Fall. 2007 IEEE 66th*, 2007, pp. 2149–2153.

[20] H. Weng, D. Beetmer, T. Hubing, X. Dong, R. Wiese, and J. McCallum, "Investigation of cavity resonances in an automobile," in *Electromagnetic Compatibility, 2004. EMC 2004. 2004 International Symposium on*, vol. 3, 2004, pp. 766–770 vol.3.

[21] A. Ruddle, "Validation of simple estimates for average field strengths in complex cavities against detailed results obtained from a 3d numerical model of a car," *Science, Measurement Technology, IET*, vol. 2, no. 6, pp. 455–466, 2008.

[22] "The SEFERE project." [Online]. Available: http://www.sefere.org/

[23] F. Bellens, F. Quitin, F. Horlin, and P. De Doncker, "Channel measurements and MB-OFDM performance inside a driving car," in *Electromagnetics in Advanced Applications, 2009. ICEAA '09. International Conference on*, 2009, pp. 392–395.

[24] J. Andersen, K. L. Chee, M. Jacob, G. Pedersen, and T. Kurner, "Reverberation and absorption in an aircraft cabin with the impact of passengers," *Antennas and Propagation, IEEE Transactions on*, vol. 60, no. 5, pp. 2472 –2480, May 2012.

[25] Y. Katayama, K. Terasaka, K. Higashikaturagi, I. Matunami, and A. Kajiwara, "Ultra-wideband impulse-radio propagation for in-vehicle wireless link," in *Vehicular Technology Conference, 2006. VTC-2006 Fall. 2006 IEEE 64th*, 2006, pp. 1–5.

[26] N. Zhang, X. Zhu, L. Liu, C. Yu, Y. Zhang, Y. Dong, H. Zhang, Z. Kuai, and W. Hong, "Measurement and characterization of wideband channel for in-vehicle environment," in *Radio and Wireless Symposium, 2009. RWS '09. IEEE*, jan. 2009, pp. 191 –194.

[27] W. Niu, J. Li, and T. Talty, "Ultra-wideband channel modeling for intravehicle environment," *EURASIP J. Wirel. Commun. Netw.*, vol. 2009, pp. 7:1–7:12, Jan. 2009. [Online]. Available: http://dx.doi.org/10.1155/2009/806209

[28] ——, "Intra-vehicle UWB channel measurements and statistical analysis," in *Global Telecommunications Conference, 2008. IEEE GLOBECOM 2008. IEEE*, 2008, pp. 1–5.

[29] W. Xiang, "A vehicular ultra-wideband channel model for future wireless intra-vehicle communications (IVC) systems," in *Vehicular Technology Conference, 2007. VTC-2007 Fall. 2007 IEEE 66th*, 2007, pp. 2159–2163.

[30] U. Demir, C. Bas, and S. Coleri Ergen, "Engine compartment UWB channel model for intra-vehicular wireless sensor networks," pp. 1–1, 2013.

[31] C. Bas and S. Ergen, "Ultra-wideband channel model for intra-vehicular wireless sensor networks beneath the chassis: From statistical model to simulations," *Vehicular Technology, IEEE Transactions on*, vol. 62, no. 1, pp. 14–25, 2013.

[32] ——, "Ultra-wideband channel model for intra-vehicular wireless sensor networks," in *Wireless Communications and Networking Conference (WCNC), 2012 IEEE*, 2012, pp. 42–47.

[33] L. Liu, Y. Wang, N. Zhang, and Y. Zhang, "UWB channel measurement and modeling for the intra-vehicle environments," in *Communication Technology (ICCT), 2010 12th IEEE International Conference on*, 2010, pp. 381–384.

[34] H. Sawada, T. Tomatsu, G. Ozaki, H. Nakase, S. Kato, K. Sato, and H. Harada, "A sixty GHz intra-car multi-media communications system," in *Vehicular Technology Conference, 2009. VTC Spring 2009. IEEE 69th*, 2009, pp. 1–5.

[35] A. Saleh and R. Valenzuela, "A statistical model for indoor multipath propagation," *Selected Areas in Communications, IEEE Journal on*, vol. 5, no. 2, pp. 128 –137, Feb 1987.

[36] H.-M. Tsai, W. Viriyasitavat, O. Tonguz, C. Saraydar, T. Talty, and A. Macdonald, "Feasibility of in-car wireless sensor networks: A statistical evaluation," in *Sensor, Mesh and Ad Hoc Communications and Networks, 2007. SECON '07. 4th Annual IEEE Communications Society Conference on*, 2007, pp. 101–111.

[37] A. Moghimi, H.-M. Tsai, C. Saraydar, and O. Tonguz, "Characterizing intra-car wireless channels," *Vehicular Technology, IEEE Transactions on*, vol. 58, no. 9, pp. 5299–5305, 2009.

[38] K. Karlsson, X. Chen, P.-S. Kildal, and J. Carlsson, "Doppler spread in reverberation chamber predicted from measurements during step-wise stationary stirring," *IEEE Antennas and Wireless Propagation Letters*, vol. 9, pp. 497–500, 2010.

[39] X. Chen, P.-S. Kildal, and J. Carlsson, "Determination of maximum Doppler shift in reverberation chamber using level crossing rate," in *Proceedings of the 5th European Conference on Antennas and Propagation (EUCAP)*, 2011, pp. 62–65.

[40] P. Hallbjorner and A. Rydberg, "Maximum Doppler frequency in reverberation chamber with continuously moving stirrer," in *Antennas and Propagation Conference, 2007. LAPC 2007. Loughborough*, 2007, pp. 229–232.

[41] S. M. H. A. Shah, "Wireless channel characterization of the reverberation chamber at NIST." [Online]. Available: http://publications.lib.chalmers.se/records/fulltext/137073.pdf

[42] X. Chen, "Evaluation and measurement of the Doppler spectrum in a reverberation chamber," *Progress In Electromagnetics Research M*, vol. 26, pp. 267–277, 2012.

[43] P. Corona, G. Ferrara, and M. Migliaccio, "A spectral approach for the determination of the reverberating chamber quality factor," *IEEE Transactions on Electromagnetic Compatibility*, vol. 40, no. 2, pp. 145–153, 1998.

[44] C. E. Shannon, "A mathematical theory of communication," *The Bell System Technical Journal*, vol. 27, pp. 379–423, 623–656, July, October 1948. [Online]. Available: http://cm.bell-labs.com/cm/ms/what/shannonday/shannon1948.pdf

[45] H. Nyquist, "Certain topics in telegraph transmission theory," *Proceedings of the IEEE*, vol. 90, no. 2, pp. 280 –305, Feb 2002.

[46] ——, "Certain factors affecting telegraph speed," *American Institute of Electrical Engineers, Transactions of the*, vol. XLIII, pp. 412–422, 1924.

[47] R. V. L. Hartley, "Transmission of information 1," *Bell System Technical Journal*, vol. 7, no. 3, pp. 535–563, 1928. [Online]. Available: http://dx.doi.org/10.1002/j.1538-7305.1928.tb01236.x

[48] R. G. Gallager, *Information Theory and Reliable Communication*. New York, NY, USA: John Wiley & Sons, Inc., 1968.

[49] D. Tse and P. Viswanath, *Fundamentals of wireless communication*. New York, NY, USA: Cambridge University Press, 2005.

[50] G. Durisi, U. Schuster, H. Bolcskei, and S. Shamai, "Noncoherent capacity of underspread fading channels," *Information Theory, IEEE Transactions on*, vol. 56, no. 1, pp. 367–395, 2010.

[51] G. Durisi, H. Bolcskei, and S. Shamai, "Capacity of underspread WSSUS fading channels in the wideband regime," in *Information Theory, 2006 IEEE International Symposium on*, 2006, pp. 1500–1504.

[52] G. Durisi, V. I. Morgenshtern, H. Bolcskei, U. G. Schuster, and S. Shamai (Shitz), *Information theory of underspread WSSUS channels*, 2011, pp. 65–116. [Online]. Available: http://www.nari.ee.ethz.ch/commth/pubs/p/dmbss_book10

[53] T. Koch and A. Lapidoth, "On multipath fading channels at high SNR," *Information Theory, IEEE Transactions on*, vol. 56, no. 12, pp. 5945–5957, 2010.

[54] U. Salim and D. Slock, "Asymptotic capacity of underspread and overspread stationary time- and frequency-selective channels," in *Information Theory and Applications Workshop, 2008*, 2008, pp. 562–570.

[55] ——, "Asymptotic capacity of underspread and overspread doubly selective MIMO channels," in *Personal, Indoor and Mobile Radio Communications, 2008. PIMRC 2008. IEEE 19th International Symposium on*, 2008, pp. 1–5.

[56] A. Lapidoth and S. Moser, "Capacity bounds via duality with applications to multiple-antenna systems on flat-fading channels," *Information Theory, IEEE Transactions on*, vol. 49, no. 10, pp. 2426 – 2467, oct. 2003.

[57] T. Koch and A. Lapidoth, "The fading number and degrees of freedom in non-coherent MIMO fading channels: a peace pipe," in *Information Theory, 2005. ISIT 2005. Proceedings. International Symposium on*, 2005, pp. 661–665.

[58] A. Lapidoth and S. Moser, "The fading number of single-input multiple-output fading channels with memory," *Information Theory, IEEE Transactions on*, vol. 52, no. 2, pp. 437–453, 2006.

[59] R. de Francisco, L. Huang, G. Dolmans, and H. de Groot, "Coexistence of ZigBee wireless sensor networks and Bluetooth inside a vehicle," in *Personal, Indoor and Mobile Radio Communications, 2009 IEEE 20th International Symposium on*, 2009, pp. 2700–2704.

[60] H.-M. Tsai, O. Tonguz, C. Saraydar, T. Talty, M. Ames, and A. Macdonald, "Zigbee-based intra-car wireless sensor networks: a case study," *Wireless Communications, IEEE*, vol. 14, no. 6, pp. 67–77, 2007.

[61] D. Z. Xiangming Kong and M. Ahmed, "A software-defined radio system for intravehicular wireless sensor networks," 2010.

[62] "Zigbee." [Online]. Available: http://www.zigbee.org/

[63] H. Zhang, L. Low, J. Rigelsford, and R. Langley, "Field distributions within a rectangular cavity with vehicle-like features," *Science, Measurement Technology, IET*, vol. 2, no. 6, pp. 474 –484, November 2008.

[64] T.-H. Loh, M. Alexander, P. Miller, and A. L. Betancort, "Interference minimisation of antenna-to-range interface for pattern testing of electrically small antennas," in *Antennas and Propagation (EuCAP), 2010 Proceedings of the Fourth European Conference on*, April 2010, pp. 1 –5.

[65] T. Loh, M. Alexander, F. Widmer, P. Miller, and D. Knight, "Validation of a new small-antenna radiated testing range," in *Antennas and Propagation, 2009. EuCAP 2009. 3rd European Conference on*, March 2009, pp. 699 –703.

[66] "Phantom." [Online]. Available: http://www.speag.com/products/em-phantom/

[67] T. Prakoso, R. Ngah, Z. Ghassemlooy, and T. A. Rahman, "Antenna representation in two-port network scattering parameter." *Microwave and Optical Technology*

Letters, vol. 53, no. 6, pp. 1404–1409, 2011. [Online]. Available: http://dx.doi.org/10.1002/mop.26005

[68] "Schwazbeck 9112 datasheet." [Online]. Available: http://www.schwarzbeck.de/Datenblatt/k9112.pdf

[69] "Schwazbeck 9113 datasheet." [Online]. Available: http://www.schwarzbeck.de/Datenblatt/k9113.pdf

[70] C. Delaveaud, P. Leveque, and B. Jecko, "New kind of microstrip antenna: the monopolar wire-patch antenna," *Electronics Letters*, vol. 30, no. 1, pp. 1 –2, Jan 1994.

[71] G. Conway, W. Scanlon, and D. Linton, "Low-profile microstrip patch antenna for over-body surface communication at 2.45 GHz," in *Vehicular Technology Conference, 2007. VTC2007-Spring. IEEE 65th*, April 2007, pp. 392 –396.

[72] G. Conway, W. Scanlon, C. Orlenius, and C. Walker, "In situ measurement of UHF wearable antenna radiation efficiency using a reverberation chamber," *Antennas and Wireless Propagation Letters, IEEE*, vol. 7, pp. 271 –274, 2008.

[73] A. Chandran, G. Conway, and W. Scanlon, "Compact slot-loaded patch antenna for 868 MHz wireless body area networks," in *Antennas and Propagation Conference, 2008. LAPC 2008. Loughborough*, March 2008, pp. 433 –436.

[74] "802.15.4 standard." [Online]. Available: http://standards.ieee.org/getieee802/download/802.15.4d-2009.pdf

[75] "MICAz." [Online]. Available: http://www.memsic.com/wireless-sensor-networks/

[76] "MATLAB." [Online]. Available: http://www.mathworks.co.uk/

[77] D. Pozar, *Microwave Engineering*. Wiley, 1997.

[78] A. Renyi, "Remarks on the Poisson process." [Online]. Available: http://www3.nd.edu/$\sim$mhaenggi/ee87021/Renyi-RemarksPPP.pdf

[79] J. Aitchison and J. Brown, *The Lognormal Distribution*. Cambridge University Press, 1957.

[80] J. Dawson and L. Arnaut, "Reverberation (mode-stirred) chambers for electromagnetic compatability." [Online]. Available: http://www.compliance-club.com/archive/old_archive/030530.htm

[81] L. Arnaut, "Effect of local stir and spatial averaging on measurement and testing in mode-tuned and mode-stirred reverberation chambers," *Electromagnetic Compatibility, IEEE Transactions on*, vol. 43, no. 3, pp. 305–325, Aug 2001.

[82] L. Cappetta, M. Feo, V. Fiumara, V. Pierro, and I. Pinto, "Electromagnetic chaos in mode-stirred reverberation enclosures," *Electromagnetic Compatibility, IEEE Transactions on*, vol. 40, no. 3, pp. 185–192, Aug 1998.

[83] L. Arnaut, "On the relationship between correlation length and rate of fluctuation of random fields," *Electromagnetic Compatibility, IEEE Transactions on*, vol. 49, no. 3, pp. 727–729, Aug 2007.

[84] J. D. Parsons, *The Mobile Radio Propagation Channel (Second Edition)*. Wiley, 2000.

[85] A. Goldsmith, *Wireless Communications*. Cambridge University Press, 2005.

[86] R. E. Kalman, "A new approach to linear filtering and prediction problems," 1960. [Online]. Available: http://www.cs.unc.edu/~welch/kalman/media/pdf/Kalman1960.pdf

[87] M. Hatfield, M. Slocum, E. Godfrey, and G. Freyer, "Investigations to extend the lower frequency limit of reverberation chambers," in *IEEE International Symposium on Electromagnetic Compatibility.*, vol. 1, August 1998, pp. 20–23 vol.1.

[88] O. Lunden and M. Backstrom, "Absorber loading study in FOI 36.7 m^3 mode stirred reverberation chamber for pulsed power measurements," in *IEEE International Symposium on Electromagnetic Compatibility.*, August 2008, pp. 1–5.

[89] L. Arnaut, "Compound exponential distributions for undermoded reverberation chambers," *Electromagnetic Compatibility, IEEE Transactions on*, vol. 44, no. 3, pp. 442–457, Aug 2002.

[90] R. Serra and F. Canavero, "Bivariate statistical approach for "good-but-imperfect" electromagnetic reverberation," *Electromagnetic Compatibility, IEEE Transactions on*, vol. 53, no. 3, pp. 554–561, Aug 2011.

[91] G. Orjubin, E. Richalot, S. Mengue, and O. Picon, "Statistical model of an undermoded reverberation chamber," *Electromagnetic Compatibility, IEEE Transactions on*, vol. 48, no. 1, pp. 248–251, Feb 2006.

[92] L. Arnaut and G. Gradoni, "Probability distribution of the quality factor of spacecraft structures modelled as undermoded reverberation chambers," in *Aerospace EMC, 2012 Proceedings ESA Workshop on*, May 2012, pp. 1–4.

[93] ——, "On distributions of fields and power in undermoded mode-stirred reverberation chambers," in *General Assembly and Scientific Symposium, 2011 XXXth URSI*, Aug 2011, pp. 1–4.

[94] C. Lemoine, P. Besnier, and M. Drissi, "Investigation of reverberation chamber measurements through high-power goodness-of-fit tests," *Electromagnetic Compatibility, IEEE Transactions on*, vol. 49, no. 4, pp. 745–755, Nov 2007.

[95] C. Holloway, H. Shah, R. Pirkl, K. Remley, D. Hill, and J. Ladbury, "Early time behavior in reverberation chambers and its effect on the relationships between coherence bandwidth, chamber decay time, RMS delay spread, and the chamber buildup time," *Electromagnetic Compatibility, IEEE Transactions on*, vol. 54, no. 4, pp. 714–725, Aug 2012.

[96] W. C. Y. Lee, *Mobile Cellular Telecommunications Systems*. McGraw Hill Publications, 1989.

[97] R. Liu, S. Herbert, T.-H. Loh, and I. Wassell, "A study on frequency diversity for intra-vehicular wireless sensor networks (WSNs)," in *Vehicular Technology Conference (VTC Fall), 2011 IEEE*, Sept 2011, pp. 1–5.

[98] A. Magleby and C. Furse, "Predicted MIMO performance in intra-vehicle channels," in *Antennas and Propagation Society International Symposium, 2008. AP-S 2008. IEEE*, July 2008, pp. 1–4.

[99] A. Magleby, C. Furse, and Z. Yun, "3d ray-tracing for intra-vehicle environments," in *Antennas and Propagation Society International Symposium, 2009. APSURSI '09. IEEE*, June 2009, pp. 1–4.

[100] F. Qu, J. Li, L. Yang, and T. Talty, "Measured channel capacity of SIMO-UWB for intra-vehicle communications," in *Antennas and Propagation (EUCAP), Proceedings of the 5th European Conference on*, April 2011, pp. 3056–3060.

[101] H. Deng, J. Li, L. Yang, and T. Talty, "Intra-vehicle UWB MIMO channel capacity," in *Wireless Communications and Networking Conference Workshops (WCNCW), 2012 IEEE*, April 2012, pp. 393–397.

[102] M. Srensen, *Ornstein–Uhlenbeck Process*. John Wiley & Sons, Ltd, 2006. [Online]. Available: http://dx.doi.org/10.1002/9780470012505.tao009m

[103] S. Bhatti, "Cross-correlation methods for antenna efficiency measurement in anechoic and reverberation chambers," Master's thesis, University of Surrey, 2010.

[104] "CC2420 datasheet." [Online]. Available: http://inst.eecs.berkeley.edu/~cs150/Documents/CC2420.pdf

[105] S. R. Searle, *Matrix Algebra Useful for Statistics*. New York, NY, USA: John Wiley & Sons, Inc., 1982.